Impact of TREM2 on MG/BMDMs during brain metastatic colonization

Dissertation
for the attainment of the doctoral degree
in Biomedical Sciences
(Dr. rer. physiol.)

of the
Faculty of Medicine
at the University Regensburg

submitted by
Jessica Alves de Lima (geb. Sonbol)
from
Alexandria (Egypt)

in the year
2025

Impact of TREM2 on MG/BMDMs during brain metastatic colonization

Dissertation
for the attainment of the doctoral degree
in Biomedical Sciences
(Dr. rer. physiol.)

of the
Faculty of Medicine
at the University Regensburg

submitted by
Jessica Alves de Lima (geb. Sonbol)
from
Alexandria (Egypt)

in the year
2025

Dean:	Prof. Dr. Dirk Hellwig
Supervisor:	Prof. Dr. med. Tobias Pukrop
Day of the oral examination:	09.07.2026

Table of contents

Zusammenfassung

Hirnmetastasen sind mit einer schlechten Prognose verbunden und treten häufig bei Lungen-, Brust-, Melanom- und kolorektalen Karzinomen auf. Während der Kolonisierung siedeln sich Tumorzellen im Gehirn an und entwickeln sich zu Makrometastasen. Unsere Studien zeigen, dass unterschiedliche histologische Wachstumsmuster (HGPs) am Makrometastase–Hirngewebe-Interface (MMPI) den Krankheitsverlauf und den neurologischen Tod entscheidend beeinflussen: Verdrängend wachsende Metastasen sind mit besserer, infiltrative mit schlechterer Prognose assoziiert. Das spezielle Immunmilieu des Gehirns erschwert die Immunabwehr, und tumorassoziierte Makrophagen (TAMs) bilden ein immunsuppressives Umfeld, das Tumorzellen schützt. In der mRNA-Analyse fiel die Überexpression des Rezeptors TREM2 auf, ein potenzieller Schlüsselregulator von Abschirmungsmechanismen. Zwar ist seine Rolle in Phagozytose und Lipidstoffwechsel bekannt, sein Einfluss auf die Metastasierung jedoch unklar. Wir postulieren, dass TREM2-positive TAMs zur lokalen Immunsuppression während der Kolonisierung beitragen. In kombinierten in vitro- und in vivo-Experimenten untersuchte ich diesen Zusammenhang in Mausmodellen mit unterschiedlichen HGPs, vergliche TREM2-Knockout-Mäuse mit Wildtyp-Tieren und analysierte HGPs, Immunlandschaft, Tumor-Makrophagen-Interaktionen, Migration und Lipidstoffwechsel. Unsere Ergebnisse zeigen, dass die verschiedenen Mausmodelle unterschiedliche HGP-Muster am MMPI aufweisen, die sowohl in frühen als auch in späten Stadien stabil bleiben und letztlich die Todesursache bestimmen. Die HGPs beeinflussen zudem die Immunlandschaft in den Hirnmetastasen-Modellen. Trotz der bekannten immunsuppressiven Funktion von TREM2 im Tumormikromilieu hatte ein TREM2-Defizit keinen signifikanten Einfluss auf die metastatische Hirnkolonisation, einschließlich Überleben, HGP oder Immunstatus. Allerdings war TREM2 mit Störungen des Lipidstoffwechsels und mitochondrialer Dysfunktion in Makrophagen assoziiert, was auf eine mögliche Rolle in metabolischen Prozessen innerhalb der metastatischen Nische hinweist.

Zusammengefasst deutet unsere Studie darauf hin, dass die Effekte von TREM2 kontextabhängig sind. Seine Beteiligung am Lipidstoffwechsel und an der mitochondrialen Funktion von Makrophagen legt jedoch nahe, dass seine Rolle bei der metastatischen Kolonisierung weiterhin eingehend untersucht werden sollte.

1. Introduction

1.1. Brain Metastasis: an unmet clinical need

Brain metastases (BM) represent a major clinical challenge and remain one of the most severe complications across several cancer entities. They occur far more frequently than primary brain tumors and are most commonly associated with lung cancer, breast cancer, melanoma, and increasingly colorectal cancer (Achrol et al. 2019; Quail and Joyce 2017). Despite continuous improvements in systemic cancer therapy, BM are still linked to high morbidity and mortality, reflecting the unique barriers and biological constraints of the central nervous system (CNS) microenvironment (Cacho-Díaz et al. 2020; Valiente et al. 2018).

Current standard-of-care approaches, including surgery, stereotactic radiosurgery, and whole-brain radiotherapy, can delay progression but rarely achieve long-term control, particularly in patients with multifocal or infiltrative lesions (Chamberlain et al. 2017). Although targeted therapies and immune checkpoint inhibitors (ICIs) have transformed the management of several metastatic cancers, their intracranial efficacy remains limited. In breast cancer, therapeutic responses are largely restricted to small subgroups such as human epidermal growth factor receptor 2 (HER2+) or triple-negative tumors, and even here CNS responses are often incomplete. In colorectal cancer, only the small fraction of microsatellite instability-high/deficient mismatch repair (MSI-H/dMMR) tumors respond to ICIs, while the vast majority of microsatellite-stable cases show minimal benefit (Cortes et al. 2020; Overman et al. 2018).

With the increasing prevalence of BM and the limited success of current therapies, there is an urgent need to better understand the mechanisms that govern metastatic colonization and immune evasion within the CNS. Dissecting the cellular and molecular crosstalk between tumor cells and the brain microenvironment, and understanding the several steps of metastatic colonization, is essential for improving survival outcomes for patients with brain metastases.

1.1.1. Steps of brain metastatic colonization

Metastatic colonization is a multistep process that presents several biological bottlenecks, including intravasation, survival in circulation, arrest in the brain vasculature, and transendothelial migration across the blood-brain barrier (BBB). It is important to distinguish cancer invasion from metastatic infiltration: invasion refers to tumor cells penetrating the basement membrane and moving through surrounding tissue, either individually or collectively, eventually entering the circulation (Novikov et al. 2021); infiltration, in contrast, involves the replacement of parenchymal cells within organ structures (Er et al. 2018).

Successful brain colonization requires adaptation to the specialized neuroimmune niche, which includes neurons, astrocytes, microglia, and other glial cells, as well as immune evasion, metabolic flexibility, and reactivation of proliferation programs (Massagué and Obenauf 2016). The BBB and the brain's unique cellular environment create a highly selective barrier, allowing fewer than 0.01% of circulating tumor cells to establish macrometastases (Gofrit et al. 2022). Most disseminated cells are eliminated by the host immune system, while a small subset may enter dormancy and form micrometastases (<2 mm), which can subsequently progress into macrometastases (≥2 mm) with an established metastatic microenvironment. Large lesions (≥10 mm) can result in irreversible organ damage and patient death (Blazquez et al. 2020a) (Figure 1).

Clinically, the interval between dissemination and macrometastatic outgrowth represents a diagnostic blind spot, as micrometastases are typically undetectable and treated empirically. While some micrometastases remain dormant for extended periods, others progress, ultimately compromising organ function and survival (Achrol et al. 2019). This underscores the urgent need to better understand the pathophysiology of metastatic colonization in the brain.

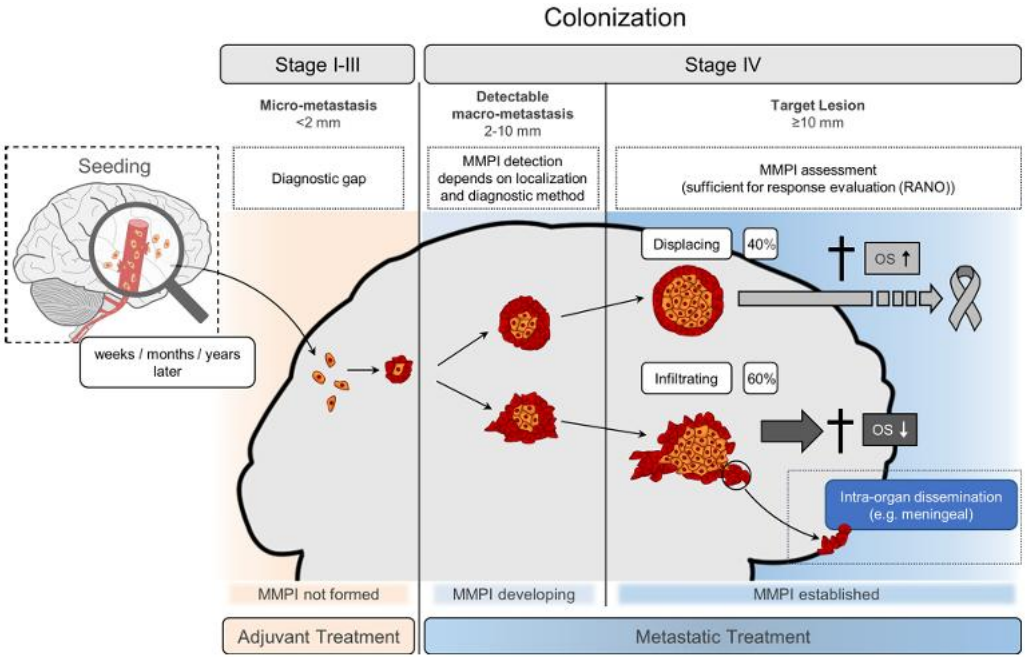

Figure 1. Cancer cell metastatic dissemination.

Metastatic colonization progresses through at least four different major phases: i) re-initiation of tumor cell proliferation, ii) formation of a micro-metastasis (<2 mm), iii) development of a macro-metastasis (≥2 mm) accompanied by the establishment of a supportive metastatic microenvironment and iv) organ destruction ultimately leading to organ failure and death. Taken from (Blazquez et al. 2020a).

1.1.2. The histological growth pattern (HGP) of BM at the macro-metastasis/organ parenchyma interface (MMPI)

We previously demonstrated that the HGP of BM at the interface with the surrounding brain tissue, defined as the region that sharply delineates the affected organ parenchyma from the macrometastatic lesion, termed the macro-metastasis/organ parenchyma interface (MMPI), is a key prognostic factor (Siam et al. 2015; Proescholdt et al. 2025), may influence disease progression and ultimately indicate the potential pathophysiological reason of the cause of death (Komljenovic et al. under revision).

BM exhibit distinct growth patterns: they may either displace adjacent brain tissue (non-infiltrative HGP) or infiltrate it (infiltrative HGP).

In detail these principal MMPI patterns have been characterized as following (Figure 2):

Displacing (non-infiltrative)– Tumor cells compress but do not infiltrate the parenchyma. These lesions exhibit distinct margins, sometimes surrounded by a reactive glial pseudo-capsule, and are associated with favorable outcomes (Blazquez et al. 2020a; Siam et al. 2015).

Epithelial infiltrative– Cohesive tumor cells penetrate the adjacent brain tissue, maintaining epithelial features and forming short-depth (<1 mm) infiltrative clusters. This pattern suggests limited yet coordinated infiltration (Blazquez et al. 2020a; Siam et al. 2015).

Diffuse infiltrative– Characterized by mesenchymal-like tumor cells with enhanced motility and infiltrative capacity, this pattern results in deep parenchymal infiltration (>2 mm), sometimes without a discernible tumor core. It is associated with poor prognosis and therapeutic resistance (Blazquez et al. 2020a; Siam et al. 2015).

These distinctions in HGP morphology not only reflect biological heterogeneity in metastatic behavior but also suggest the presence of divergent molecular mechanisms, highlighting opportunities for personalized therapeutic development.

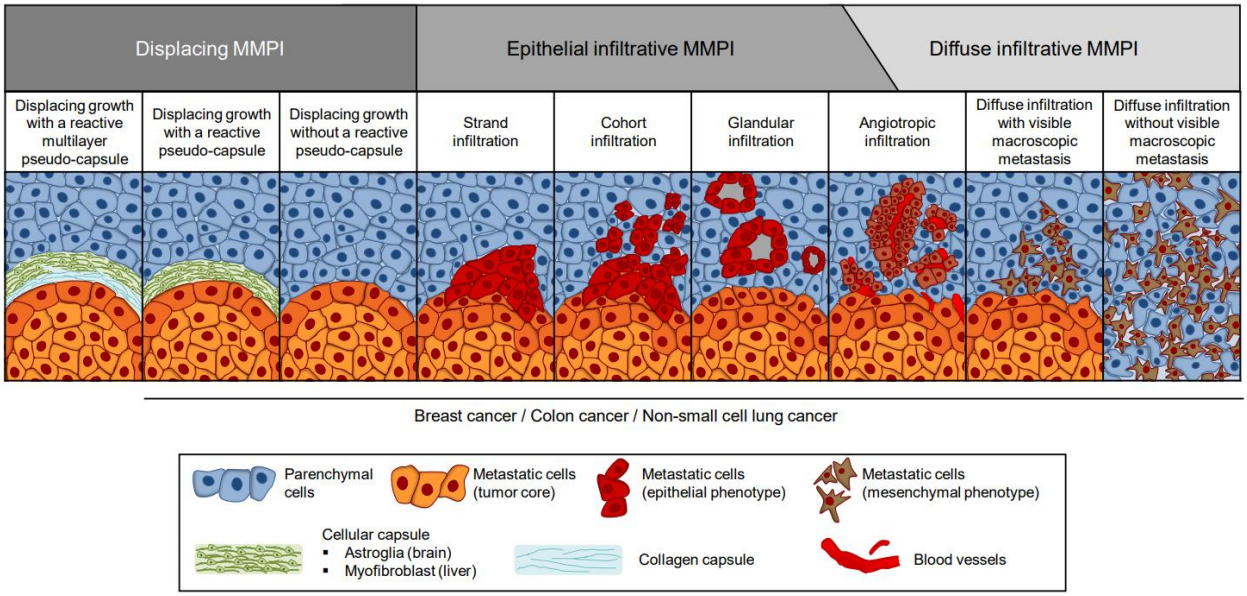

Figure 2. HGPs at the macro-metastasis/organ parenchyma interface (MMPI).

The HGP at the MMPI can be classified into three main categories: displacing, epithelial infiltrative, and diffuse infiltrative. Notably, angiotropic infiltration, characterized by tumor cell migration along host blood vessels, may exhibit features of both epithelial and diffuse patterns. Taken from (Blazquez et al. 2020a).

1.1.3. The immune microenvironment in BM

The tumor microenvironment (TME) critically influences tumor colonization and progression. In BM, the TME encompasses disseminated tumor cells, non-malignant stromal elements, and a complex immune context comprising tissue-resident microglia, peripheral myeloid cells, infiltrating lymphocytes (Schulz and Sevenich 2021). This specialized immune milieu not only responds to invading tumor cells but also actively shapes their growth dynamics, therapeutic resistance, and clinical behavior. As previously mentioned, recent studies further highlight the importance of the HGP at the MMPI as a determinant of patient outcome, suggesting that the immune composition and its functional state are tightly linked to the structural organization of metastases (Proescholdt et al. 2025; Komljenovic et al. under revision).

A conceptual framework for interpreting these immune landscapes comes from the classification proposed by (Galon and Bruni 2019) for colorectal cancer, who defined four major tumor immune phenotypes (**cold, excluded, suppressed, and hot)**, each associated with distinct T cell distribution patterns and functional immune activity. Importantly, (Galon and Bruni 2019) established these categories through a quantitative immune score, calculated by measuring the density of $CD3^+$ and $CD8^+$ T cells in both the tumor core and the margin. These phenotypes and their scoring system provide a valuable reference for understanding how immune infiltration patterns emerge within BMs and how they may correlate with specific HGPs at the MMPI.

As illustrated in Figure 3, cold tumors are characterized by low immune scores, with minimal T cell presence and poor infiltration into the tumor core. In contrast, the excluded phenotype shows an intermediate immune score in which $CD8^+$ T cells accumulate at the tumor margins but fail to penetrate the tumor parenchyma. The suppressed phenotype exhibits similar peripheral T cell accumulation but is functionally distinct: here, immunosuppressive mechanisms dominate, including increased TGF-β and IL-10, as well as the presence of regulatory T cells ($FOXP3^+$), which collectively restrain effective anti-tumor immunity (Li et al. 2025). Finally, hot tumors display high immune scores, with dense infiltration of activated $CD8^+$ T cells throughout the tumor bed, representing an inflammatory and potentially immunotherapy-responsive phenotype.

Together, these immune configurations provide a conceptual lens for interpreting the immune microenvironment in BM. When applied to the HGPs, these phenotypes suggest that the degree and pattern of immune infiltration may not only mirror but also mechanistically contribute to

the underlying growth pattern. Understanding how these immune phenotypes emerge in the context of BM will be essential for linking structural growth patterns to immune function and for identifying patients who may benefit from immune-targeted therapies.

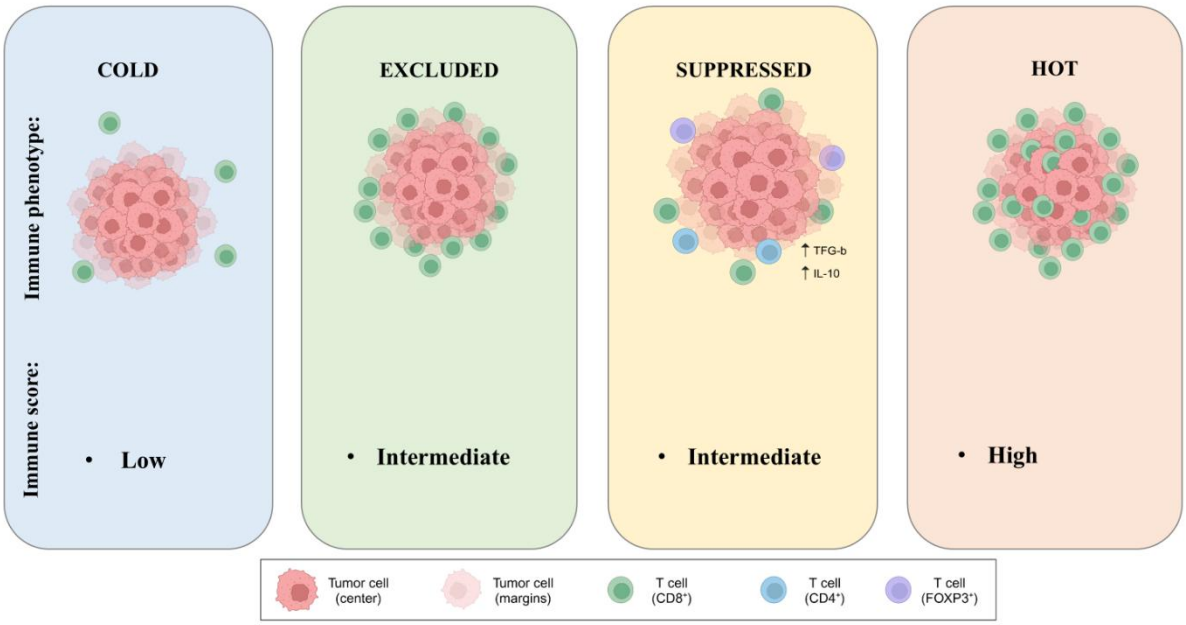

Figure 3. Classification of the tumor immune phenotypes according to the immunophenotype score.

Illustration of the four immune phenotypes, cold, excluded, suppressed, and hot. Each phenotype is defined by distinct patterns of T cell distribution and corresponding immune scores, ranging from low (cold) to high (hot). Adapted from (Galon und Bruni 2019).

1.1.4. Microglia (MG) and bone marrow-derived macrophages (BMDMs) in the brain-TME

Within BM, the TME is shaped in large part by myeloid cells, specifically, brain-resident MG and infiltrating BMDMs. Together, these populations can account for as much as 30–40% of the total tumor mass. MG, which originate from embryonic yolk-sac progenitors, are long-lived and self-renewing cells that maintain CNS homeostasis under steady-state conditions. In contrast, BMDMs are derived from circulating monocytes and are only recruited to the brain following disruption of the BBB, often triggered during metastatic progression (Schreurs et al. 2025).

Under physiological conditions, MG function as vigilant sentinels of the CNS, regulating immune surveillance and restricting peripheral leukocyte infiltration. However, the onset of

BM alters this balance dramatically. Metastatic colonization initiates a cascade of changes, including the release of damage-associated molecular patterns (DAMPs), cytokines, and extracellular matrix (ECM) remodeling cues, which collectively increase BBB permeability and facilitate monocyte infiltration. The result is a highly reactive myeloid compartment in which both MG and BMDMs adapt dynamically to cues from the evolving TME (Cotechini et al. 2021).

Both MG and BMDMs exhibit remarkable phenotypic plasticity, dynamically shifting along a spectrum from pro-inflammatory (M1-like) to anti-inflammatory/tumor-supportive (M2-like) states in response to the evolving TME (Solomou et al. 2024). M1-like macrophages drive inflammation to combat pathogens, while M2-like macrophages support tissue repair, immune modulation, and tumor growth. In the presence of oncogenic signals, macrophages increasingly shift toward M2-like, pro-metastatic, and immunosuppressive phenotypes, transitioning inflammation from acute to chronic (Doron et al. 2019). Within BM niches, tissue-resident MG often display an inflammatory signature, while recruited BMDMs adopt a pro-tumorigenic, immunosuppressive phenotype characterized by secretion of matrix metalloproteinases, angiogenic factors (e.g., VEGFA), and checkpoint molecules (e.g., PD-L1). These BMDMs facilitate tumor growth, dampen cytotoxic T cell activity, and contribute to resistance to immune checkpoint blockade. Yet, the molecular mechanisms that govern the activation states and functional specialization of these myeloid cells within BM remain only partially elucidated. Recently, attention has been focused on the distinct subpopulations of macrophages based on their specific surface markers and gene expression profiles. Among these, **Triggering Receptor Expressed on Myeloid Cells 2 (TREM2)** has emerged as a particularly notable molecule (Ulland et al. 2017). TREM2 plays a central role in shaping the immunosuppressive phenotype of TAMs, exerting broad influence over their behavior during tumor progression and metastatic colonization. Its expression has been linked to immune evasion, impaired antigen presentation, and promotion of a tumor-supportive microenvironment, marking it as a key regulator of myeloid cell function during tumor progression and metastasis (Zhong et al. 2024; Sun et al. 2023; Binnewies et al. 2021; Molgora et al. 2020).

1.2. TREM2 signaling

TREM2 plays a pivotal role in innate immune regulation, including phagocytosis, inflammation control, and cellular survival (Deczkowska et al. 2020; Yao et al. 2016). As a member of the immunoglobulin superfamily, TREM2 signals through an adaptor protein known as DNAX-activating protein of 12 kDa (DAP12) or, in some contexts, DAP10, both of which contain an immunoreceptor tyrosine-based activation motif (ITAM). Upon binding with its known ligands apolipoprotein E (ApoE) or lipopolysaccharide (LPS), TREM2 interacts with DAP12 via a conserved lysine residue in its transmembrane domain, initiating a signaling cascade through ITAM phosphorylation by Src family kinases (Figure 4). This phosphorylation recruits and activates spleen tyrosine kinase (Syk), which in turn drives downstream pathways such as phosphoinositide 3-kinase (PI3K)/Akt, extracellular signal-regulated kinase 1/2 (ERK1/2)/mitogen-activated protein kinase (MAPK), and phospholipase Cγ (PLCγ). Although TREM2 is expressed at the cell surface, it undergoes proteolytic cleavage by metalloproteases, releasing a soluble form known as (sTREM2) into the extracellular milieu (Ulland and Colonna 2018). This cleavage is believed to modulate the activation status of myeloid cells, and sTREM2 has been proposed to support the survival of neighboring cells (Zhong et al. 2017). These cascades collectively regulate key microglial functions such as proliferation, metabolic adaptation, phagocytic clearance, and cytokine secretion (Colonna and Wang 2016). Given its central role in regulating both the structural and functional landscape of the innate immune system, TREM2 has become a focus of intense research interest in both neuroinflammatory and oncological contexts.

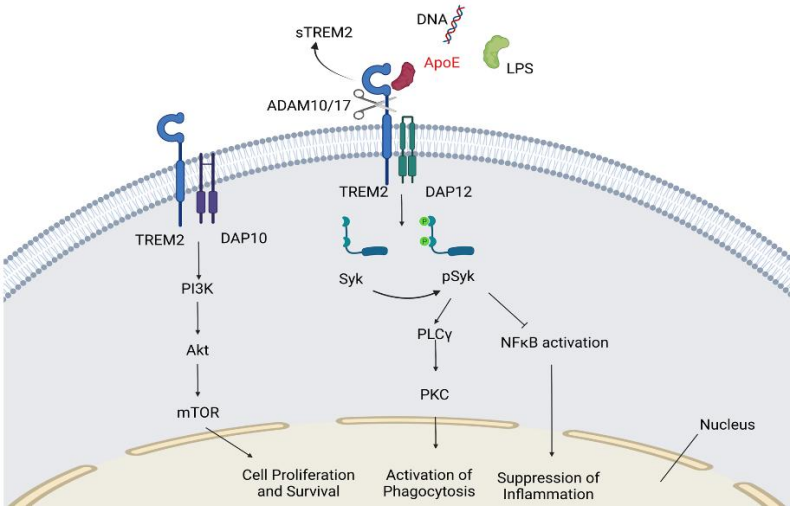

Figure 4. Schematic illustration of TREM2's signaling pathway.

Upon binding of TREM2 to its ligands, such as ApoE, LPS, or DNA debris, intracellular signaling is initiated via the adaptor proteins DAP10 and DAP12, leading to activation of PI3K

and Syk pathways, respectively. Proteolytic cleavage of TREM2 within its stalk region by ADAM10/17 generates sTREM2 and terminates downstream signaling. Image created with Biorender.com. Adapted from (Deczkowska et al. 2020; Yao et al. 2016).

1.2.1. Metabolic functions of TREM2 in Alzheimer's disease

TREM2 has emerged as a key player in neurodegeneration, particularly in Alzheimer's disease (AD). Genome-wide association studies have identified loss-of-function mutations in TREM2 as strong risk factors for late-onset AD (Guerreiro et al. 2013). Functionally, TREM2 is crucial for the activation of disease-associated microglia (DAM), a specialized microglial state responsible for recognizing and clearing amyloid-beta plaques, apoptotic cells, and lipid-rich debris. Loss of TREM2 disrupts this protective transition, leading to defective phagocytosis, impaired immune surveillance, and accelerated neurodegeneration. Mechanistic studies have shown that TREM2 deficiency impairs cholesterol efflux in microglia, where chronic myelin phagocytosis drives the accumulation of cholesteryl ester (CE) and oxidized CE (oxCE) in the brain. Notably, only CE accumulation could be rescued either by inhibiting acetyl-CoA acetyltransferase 1 (ACAT1), the enzyme converting free cholesterol to CE, or by activating liver X receptor (LXR) signaling, highlighting a direct link between TREM2 and lipid metabolism (Figure 5) (Nugent et al. 2020). Beyond lipid handling, TREM2 signaling supports metabolic reprogramming and microglial survival under pathological stress, emphasizing its central role in maintaining CNS immune homeostasis. Collectively, these findings position TREM2 as a neuroprotective factor in neurodegenerative disease contexts (Ulland et al. 2017; Ulrich et al. 2017; Wang et al. 2015).

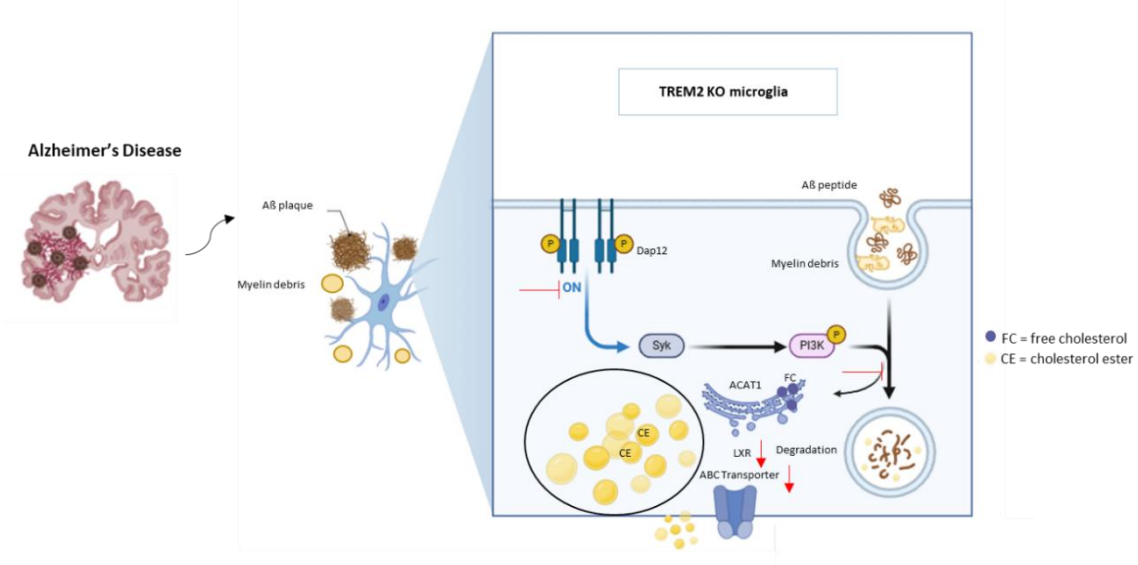

Figure 5. Schematic illustration of TREM2's metabolic role in Alzheimer's disease.

Loss of TREM2 disrupts Dap12–Syk–PI3K signaling, leading to defective myelin and Aβ debris degradation, impaired ABC transporter-mediated lipid efflux, and accumulation of cholesteryl esters (CE) in microglia. Image created with Biorender.com. Adapted from (Nugent et al. 2020).

1.2.2. Distinct roles of TREM2 in tumor progression

Beyond its role in neurodegeneration, TREM2 has emerged as a complex player in the TME, particularly in brain and peripheral tumors. It is highly expressed in TAMs, where it is associated with an immunosuppressive, M2-like phenotype that fosters tumor growth, immune evasion, and metastasis (Molgora et al. 2020) (Figure 6A). TREM2+ TAMs have been shown to inhibit cytotoxic T cell responses, support angiogenesis, and facilitate extracellular matrix remodeling, mechanisms that collectively enhance tumor progression (Wang et al. 2025).

However, recent findings have challenged this view by showing that TREM2's role in cancer may be more nuanced and highly dependent on tumor type and microenvironmental context (Sun et al. 2023). For example, (Zhong et al. 2024) reported that TREM2 deficiency in certain models leads to reduced tumor burden and prolonged survival, suggesting a potential tumor-suppressive effect (Figure 6B). In contrast, other studies such as those in glioblastoma models have reported no significant impact of TREM2 deletion on immune function or tumor progression (Figure 6C) (Peshoff et al. 2024; Zheng et al. 2023).

These apparently contradictory roles underscore the highly variable influence of TREM2 across different tumor types, model systems, and disease stages.

Therefore, TREM2 should not be viewed as a universal oncogenic or tumor-suppressive molecule. Rather, its function appears to be highly model-specific and dependent on microenvironmental and temporal cues, making it a compelling, yet challenging, target in cancer immunotherapy.

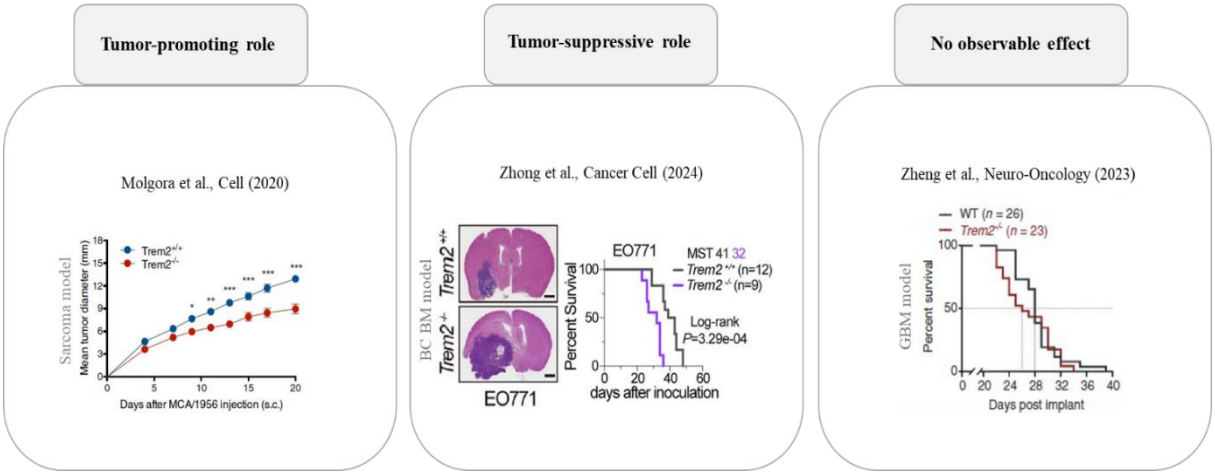

Figure 6. Schematic illustration of TREM2's divergent roles in tumor models.

Summary of studies showing context-dependent effects of TREM2 loss: (A) Tumor-promoting role in a sarcoma model (Molgora et al. 2020), (B) tumor-suppressive role in a breast cancer brain metastasis model (Zhong et al. 2024), and (C) no observable effect in a glioblastoma model (Peshoff et al. 2024; Zheng et al. 2023).

1.2.3. Potential role of TREM2 as driver of metastatic colonization

Our research group focuses on brain metastatic colonization, particularly the different HGPs at the MMPI. Using mouse models of breast and colon cancer metastasis to the brain and liver, we previously identified a set of 252 genes that act as shared drivers of metastatic colonization across organs and tumor entities (unpublished data). In parallel, our collaborators at the Charité Berlin, led by Gerhard Krönke, identified a specialized macrophage population in joint injury, termed shielding macrophages, which forms a protective barrier preventing cytotoxic immune cells from accessing damaged tissue (Collison 2019). This macrophage-mediated shielding appears critical for preserving tissue integrity and may represent a conserved immune-regulatory mechanism.

Krönke's group further characterized this response across multiple tissue-damage models, including joint and muscle injury, defining a 20-gene signature associated with macrophage-mediated shielding (Culemann et al. 2019). When comparing this dataset with our 252-gene colonization signature, we identified six overlapping genes, representing strong candidate mediators of shielding-like functions during metastatic colonization (Figure 7). Notably, TREM2 was consistently overexpressed at the mRNA level across all analyzed models.

Given this convergence, TREM2 emerged as a compelling regulator of macrophage function within the metastatic microenvironment. Its potential role in shaping the brain metastatic niche, and possibly contributing to shielding-like mechanisms that support tumor cell survival, formed the central rationale of this study.

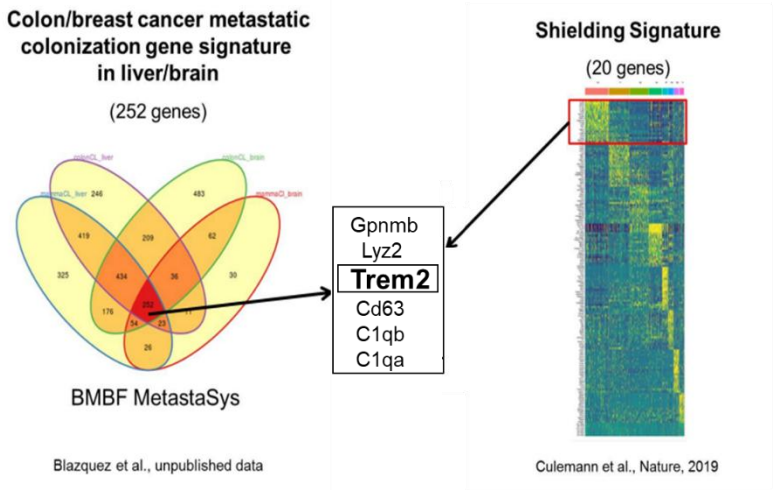

Figure 7. Overlapping genes among the colonization and shielding signature.

The shielding signature (20 genes) identified by Gerhard Krönke´s group in tissue damage models and the colonization signature (252 genes) from Tobias Pukrop´s group in metastatic colonization models of brain and liver metastases (unpublished) were compared. Six genes overlapped between both signatures, representing potential candidates involved in shielding during metastatic colonization.

1.3. Aims of the study

This dissertation proposes that the HGP at the MMPI critically shapes the immune landscape of BM by modulating immune cell infiltration and macrophage behavior. The central hypothesis is that TREM2-expressing TAMs promote local immune suppression during brain metastatic colonization.

The research is structured around two key objectives. The first is to establish and characterize syngeneic mouse models of BM that exhibit distinct HGPs at the MMPI. This includes assessing whether these HGPs remain consistent between early and late stages of colonization and investigating how these patterns correlate with immune cell composition, tumor colonization efficiency, and survival outcomes. The second objective focuses on the functional role of TREM2, a known immunoregulatory receptor expressed on myeloid cells. Using both *in vitro* and *in vivo* approaches, this work aims to determine how TREM2 influences macrophage lipid metabolism, tumor–macrophage interactions, and the broader immune response during metastatic outgrowth.

Through these investigations, the study aims to generate new insights into how HGPs and immune signaling pathways cooperate to regulate metastatic progression in the brain. The findings may also help shed some light on the distinct functions of TREM2 on macrophage lipid metabolism and during brain metastatic colonization.

In detail, the specific aims pursued in this study:

1. Develop and characterize syngeneic mouse models of breast and colorectal brain metastasis exhibiting distinct HGPs, both in early and late colonization.
2. Assess the immune cell composition within the brain metastatic microenvironment across different HGPs at the MMPI *in vivo*.
3. Evaluate the role of TREM2 in regulating macrophage lipid metabolism *in vitro*.
4. Analyze how TREM2 influences tumor–macrophage interactions *in vitro*.
5. Determine the impact of TREM2 on brain metastatic colonization and immune modulation *in vivo*.

2. Materials and Methods

2.1. Materials

2.1.1. Biological materials

2.1.1.1. Cell lines

The cell lines used in this study are listed in Table 1.

Table 1. Cell lines.

Name	Cell type/species	Background	Origin/source	Reference
E0771-LG	Murine breast cancer	C57BL/6	Prof. J. Pollard (Edinburgh, UK)	(Kitamura et al. 2019)
CMT93Var	Murine colorectal cancer (polypoid)	C57BL/6	Prof. Dr. C. Hackl (Regensburg, Germany)	(Franks and Hemmings 1978)
KPN	Murine small intestinal tumor organoid	C57BL/6	Prof. Dr. Elisabeth Naschberger (Erlangen, Germany)	(Jackstadt et al. 2019)
99LN	Murine breast cancer (luminal B)	C57BL/6	Prof. Dr. Lisa Sevenich (Frankfurt am Main, Germany)	(Wu et al. 2021)

2.1.1.2. Primary cells

Bone marrow-derived macrophages (BMDM) were isolated from the bone marrow of adult mice (10-12 weeks-old) following the protocol described in 2.2.1.2.1.

2.1.1.3. Mouse strains

Adult wild type mice (C57BL/6J) were bred in-house, while Trem2 KO mice (C57BL/6J-Trem2^{em2Adiuj}/J) were obtained from Jackson Laboratory (Bar Harbor, USA). All animals were housed under standard conditions and received a standard diet. Newborn mice were bred and obtained from the animal facility (ZTL) of the University Hospital Regensburg.

2.1.2. Cell culture media and additives

All media and additives used for the culture of the cell lines and primary cells are listed in Table 2.

Table 2. Cell culture and additives.

Product	Company
Accutase solution	Sigma-Aldrich (Steinheim)
Dulbecco's modified Eagle medium DMEM (without Glutamine, Glucose 1g/l)	Sigma-Aldrich (Steinheim)
DMEM (Glucose 1g/l, with stable Glutamine)	Bio & Sell (Nürnberg)
Dulbecco's Phosphate Buffered Saline (PBS) without Ca2+, Mg2+	Gibco/Thermo Fisher (Darmstadt)
Fetal calf serum (FCS)	Bio & Sell (Nürnberg)
GlutaMAX-I Supplement (stable Glutamine)	Gibco/Thermo Fisher (Darmstadt)
Hank's balanced salt solution (HBSS)	Gibco/Thermo Fisher (Darmstadt)
Lipopolysaccharide (LPS) from E. coli	Enzo Life Sciences (Lörrach)
Normal goat serum (NGS)	Sigma-Aldrich (Steinheim)
Normal horse serum (NHS)	Gibco/Thermo Fisher (Darmstadt)
Recombinant Mouse Apolipoprotein E (His-Tag)	Abcam (Cambridge)
Sodium Pyruvate	Sigma-Aldrich (Steinheim)
Trypsin-EDTA (1X)	Sigma-Aldrich (Steinheim)
2-Mercaptoethanol 50 mM	Gibco/Thermo Fisher (Darmstadt)

2.1.3. Chemicals, enzymes and ready-to-use reagents.

All used chemicals, enzymes as well as other reagents are listed in Table 3.

Table 3. Chemicals, enzymes and other reagents.

Product	Company
100 bp DNA ladder	Thermo Fisher Scientific (Waltham)
2-Propanol 70%	B. Braun (Melsungen)
Acetic acid	Carl Roth (Karlsruhe)
Agarose	Carl Roth (Karlsruhe)
Ammonium Persulfate (APS)	VWR (Ismaning)
Antibody Diluent	Dako (Jena)
Aqua bidest	B.Braun (Melsungen)
Bovine Serum Albumin (BSA) Standard Ampules	Gibco/ Thermo Fisher (Darmstadt)
Chloroform	Carl Roth (Karlsruhe)

Chromogen solution (Chromogens Red)	Dako (Jena)
Cytoblock Reagent	Epredia (Dreieich)
Cytopainter green/red	Abcam (Cambridge)
Chloroform	Carl Roth (Karlsruhe)
Dimethiyl Sulfoxide (DMSO)	Sigma-Aldrich (Steinheim)
DNase I (10u/µl)	Roche (Mannheim)
DNase I Incubation Buffer (10X)	Roche (Mannheim)
Domitor	Orion Pharma (Hamburg)
Ethanol, absolute for analysis	Merck Millipore (Darmstadt)
Ethylenediaminetetraacetic acid (EDTA)	Carl Roth (Karlsruhe)
Extracellular Matrix (ECM)	R&D Systems (Wiesbaden)
Fluorescent mounting medium	Agilent Dako (Glostrup, Denmark)
Fura-2/AM	Hölzel Biotec (Köln)
Gadolinium chelate agent	Bayer GmbH (Leverkusen)
GelRed Nucleic Acid Gel Stain	Biotium/Biozol (Fremont)
Gene ladder	Thermo Fisher Scientific (Waltham)
Glycine	Carl Roth (Karlsruhe) Merck Millipore (Darmstadt)
H_2O for molecular biology (RNase-free, DNase-free)	Sigma-Aldrich (Steinheim)
Isoflurane	Piramal Healthcare (Hallbergmoos)
Isopropanol	VWR Chemicals (Darmstadt)
iTaq Universal SYBR Green Supermix	Bio-Rad (Munich)
JC-1	Invitrogen by Life Technologies (Carlsbad, California)
KAPA 2G Fast Ready Mix with dye	Roche (Mannheim)
Ketamine	Serumwerk (Bernburg)
Lidocaine	Vetviva Richter (Wels)
Matrigel	Corning (Kaiserslautern)
MitoTracker Green	Invitrogen by Life Technologies (Carlsbad, California)
Methanol 100%	Merck Millipore (Darmstadt)
NaCl 0,9%	B. Braun (Melsungen)
NaOH	B. Braun (Melsungen)
OptiMEM	Gibco/Thermo Fisher (Darmstadt)
Paraformaldehyde (PFA)	Merck Millipore (Darmstadt)
Peroxidase solution	Merck Millipore (Darmstadt)
Phenol/chloroform/isoamyl alcohol	Carl Roth (Karlsruhe)
Phosphatase inhibitor PhosSTOP (10x)	Roche (Mannheim)

Poly-L-Lysine	Sigma-Aldrich (Steinheim)
Ponceau S Solution	AppliChem (Darmstadt)
Precision Plus Protein Dual Xtra	Bio-Rad (Munich)
Ringer solution	Sigma-Aldrich (Steinheim)
Rimadyl	Zoetis (Berlin)
RNase OUT (40 u/µl)	Invitrogen/ ThermoFisher (Karlsruhe)
Rhod-2/AM	Hölzel Biotech (Köln)
Rotiphorese Gel 30	Carl Roth (Karlsruhe)
Streptavidin alkaline phosphatase	Dako (Jena)
Tetramethylethylendiamin (TEMED)	AppliChem (Darmstadt)
Tris-Wash Buffer (pH6)	Merck Millipore (Darmstadt)
Triton X-100	Sigma-Aldrich (Steinheim)
TRIzol Reagent	Invitrogen/ ThermoFisher (Karlsruhe)
Tween 20	Sigma-Aldrich (Steinheim)
Xylol	Carl Roth (Karlsruhe)

2.1.4. Buffers and solutions

The antibodies and fluorescence dyes used in this study are listed in Table 4.

Table 4. Buffers and solutions.

Description	Concentration	Composition
6x DNA loading dye blue	10 mM	Tris-Base/Tris-HCl
	0.03%	bromophenol blue
Citrate buffer	2.1 g	solution A: tri-sodium citrate dihydrate in 100 ml H2O
	29.41 g	solution B: hydroxytricarballylic acid in 1 l
	2ml	H2O
	98ml	solution A
	ad 1 l	solution B
		H2O
		pH 6.0
10x Electrophoresis buffer	30g	Tris-Base
	144g	glycine
	10g	SDS
	ad 1L	Aqua
FACS washing buffer	98%	DPBS
	2%	FCS
PFA solution 4%	24 g	PFA
	540 ml	distilled water (dH_2O)

		solve at 60 °C
	6–9 drops	NaOH
	60 ml	10x PBS
		pH 7.3
	ad 1L	Aqua
	100x	protease inhibitor
Sodium acetate	123g	Na-acetate
	Ad 500 ml	Aqua
	Adjust pH	pH 4.8
Tris-acetate-EDTA (TAE) buffer	40 mM	Tris-Acetate
	1 mM	EDTA
	0.1%	glacial acetic acid
	ad	H_2O
10x Tris-buffered saline with Tween20 (TBST)	20 mM	Tris-Base/Tris-HCl
	150 mM	NaCl
	ad 1 L	
	Asjust pH with HCL	pH 7.6
	0.1%	(v/v) Tween20
Tris-EDTA (TE) buffer	5 ml	Tris-Base/Tris-HCl
	1 ml	EDTA
	494 ml	H_2O
Triton X	0.5%	0.5% (v/v) Triton X-100 in PBS

2.1.5. Antibodies and fluorescence dyes

The antibodies and fluorescence dyes used in this study are listed in Table 5.

Table 5. Antibodies and fluorescence dyes.

Name	Source	Label	Application/ Dilution	Company/ Cat. Nr.
Alexa Fluor 568 isolectin GS-IB4 conjugate	Griffonia simplicifolia	Alexa Fluor 568	IF (1:500)	Thermo Fisher (#21412)
Alexa Fluor 647 isolectin GS-IB4 conjugate	Griffonia simplicifolia	Alexa Fluor 647	IF (1:500)	Thermo Fisher (#132450)
E-Cadherin	Rabbit	-	IF (1:100)	Cell Signaling (#3195S)
Vimentin	Rabbit	-	IF (1:100)	Cell Signaling (#5741)
Phalloidin	Amanita phalloides	TRITC	IF (1:600)	Sigma-Aldrich (#P1951)

DAPI	Rabbit	-	IF (1:2.000)	Sigma-Aldrich (#D8417)
Isotype IgG2b	Rat	Alexa Fluor 488	FACS; 0,5 mg/ml	BioLegend; 400625
Isotype IgG2c	Rat	APC	FACS; 0,2 mg/ml	BioLegend; 400713
Isotype IgG2b	Rat	PE	FACS; 0,2 mg/ml	BioLegend; 400608
anti-mouse Ly-6C	Rat	APC	FACS; 0,2 mg/ml	BioLegend; 128016
anti-mouse Ly-6G	Rat	PE	FACS;0,2 mg/ml	BioLegend; 127607
anti-mouse CD11b	Rat	Alexa Fluor 488	FACS; 0,2 mg/ml	BioLegend; 101217
anti-mouse CD45	Rat	APC	FACS; 0,2 mg/ml	BioLegend; 103112
anti-mouse CD45	Rat	Alexa Fluor 488	FACS; 0,5 mg/ml	BioLegend; 103121
anti-mouse CD 45	Rat	Alexa Fluor 700	FACS; 0,5 mg/ml	BioLegend; 103121
anti-mouse CD45	Rat	PE	FACS; 0,2 mg/ml	BioLegend; 103105
anti-mouse CD9	Mouse	FITC	FACS; 0,2 mg/ml	BioLegend; 124808
anti-mouse CD36	Mouse	APC	FACS; 0,2 mg/ml	BioLegend; 102612
Ck8	Rabbit	-	IHC (1:1000)	Abcam (#ab59434)
Iba1	Rabbit	-	IHC (1:1000)	Wako (#019-19741)
Gfap	Rabbit	-	IHC (1:200)	Dake (#ZO334)
Cd3	Rabbit	-	IHC (1:150)	DCS Diagnostics (#CI597C01)
Cd8	Rabbit	-	IHC (1:2000)	Abcam (#ab 209775)
Anti Rabbit IgG, biotin (H+L) Biotin	Goat	-	IHC (1:250)	Dianova (#111-065-144)
Streptavidin HRP	-	-	IHC (1:1000)	Zytomed (#ZUC-012008)
DAB-kit	-	-	IHC (1:50)	Dako (#K3468)

2.1.6. Oligonucleotides

Table 6 summarizes all oligonucleotides used for this study.

Table 6. Oligonucleotides

Name	Description	Direction	Sequence (5`-3`)
mmGapdh	Glycerinaldehyde-3-phosphate dehydrogenase	Forward	CATCTTGGGCTACACTGAG
		Reverse	CTGTAGCCGTATTCATTGTC
mmPgk1	Phosphoglycerate Kinase 1	Forward	TGTCCAAACTAGGAGATGTC
		Reverse	CCTTGGCAAAGTAGTTCAG
mmTrem2	Triggering receptor expressed on myeloid cells 2	Forward	CATCACTCTGAAGAACCTCC
		Reverse	ATCTTGGTCATCTAGAGGGT
mmApoE	Apolipoprotein E	Forward	GGACTTGTTTCGGAAGGA
		Reverse	CAGCAATGTGACCAACAG
mmLpl	Lipoprotein Lipase	Forward	AGATTCATCAACTGGATGGA
		Reverse	CTTCTTATTGGTCAGACTTCC
mmGpnmb	Glycoprotein NMB	Forward	CAGAAGGAAGATGCTAATGG
		Reverse	GTCAGTCCCAAATCATTCCT
mmTyrobp	TYRO protein tyrosine Kinase binding protein	Forward	AAACAACACATTGCTGAGAC
		Reverse	CATCTGTAATATTGCCTCTGTG
mmIl-6	Interleukin 6	Forward	GATGGATGCTACCAAACTG
		Reverse	CCAGGTAGCTATGGTACTC
mmTnfa	Tumor Necrosis Factor alfa	Forward	TCCCCAAAGGGATGAGAAGT
		Reverse	CTCCTCCACTTGGTGGTTTG
mmIl-1b	Interleukin 1 beta	Forward	GTAATGAAAGACGGCACACC
		Reverse	ACTCTGCAGACTCAAACTCC
mmIl-10	Interleukin 10	Forward	GAAGACAATAACTGCACCCA
		Reverse	CATTAAGGAGTCGGTTAGCAG
mmArg1	Arginase 1	Forward	CAAAGACATCGTGTACATTGG
		Reverse	TTGTCTACTTCAGTCATGGA
mmHcst	Hematopoietic cell signal transducer	Forward	GTGGTGTTTGTATGTATGCG
		Reverse	AGGCATGTTGATGTAGACTC
mmMrc1	Mannose receptor 1	Forward	ATTATGGCAACAGACAAGAG
		Reverse	GAGTACATGGCTTCATATCCT
mmTgfβ	Transforming growth factor, beta 1	Forward	TGATACGCCTGAGTGGCTGTCT
		Reverse	CACAAGAGCAGTGAGCGCTGAA
mmIba1	allograft inflammatory factor 1	Forward	TTCAGCTACTCTGACTTTCTC
		Reverse	GAATCATTCTCAAGATGGCAG
mmCsf1	colony stimulating factor 1	Forward	GCGCTTTAAAGACAACACCC
		Reverse	ATGGAAAGTTCGGACACAGG
mmCsf1r	colony stimulating factor 1 receptor	Forward	CACCATCCACTTGTATGTC
		Reverse	CTCAACCACTGTCACCTC
mmGfap	glial fibrillary acidic protein	Forward	AACCTGGCTGCGTATAGAC
		Reverse	CCAGCGATTCAACCTTTCTC
mmCd3		Forward	TACTTGTACCTGAAAGCTCG

	Cluster of differentiation 3	Reverse	CTTGCTCCAGTAATAAATGACC
mmCd8	Cluster of differentiation 8	Forward	TAATAAGTACGTTCTCACCC
		Reverse	GTAGTAGAGTTCACTTTCTG
mmCd4	Cluster of differentiation 4	Forward	TTAAGATGGAAGACTCTCAGAC
		Reverse	CTGAAGGTCACTTTGAACAC
mmFoxp3	Forkhead box protein 3	Forward	CAACCTAGCCCCAAGATGAA
		Reverse	CCAGATGTTGTGGGTGAGTG
mmTrem2 (Genotyping)	glial fibrillary acidic protein	Forward	TCAGGGAGTCAGTCATTAACCA
		Reverse	CAATAAGACCTGGCACAAGGA

2.1.7. Commercial kits

All commercial kits are listed in Table 7.

Table 7. Commercial kits.

Product	Company
Clarity Western ECL Reagent A+B	Bio-Rad (Feldkirchen)
DNA polymerase enzyme	PAN Biotech (Aidenbach)
High Pure RNA Isolation Kit	Roche (Mannheim)
iScript cDNA synthesis Kit	Bio-Rad (Feldkirchen)
Monarch Genomic DNA Purification Kit	New England Biolabs (Frankfurt am Main)
Mycoplasma test Kit	Lonza (Basel)
QIAamp DNA Mini Kit	Qiagen (Hilden)
Signal Fire – Elite ECL Reagent A+B	Cell Signaling Technology (Leiden)

2.1.8. Consumables

All consumables used in this study are listed in Tabe 8.

Table 8. Consumables.

Product	Company
5ml Polystyrene Round Bottom Tube	Corning (Kaiserslautern)
5ml Polystyrene Round Bottom Tube with Cell-Strainer Cap 35µm	Corning (Kaiserslautern)
10 cm Petri dish (coated)	Nunc (Langenselbold)
10 cm Petri dish (un-coated)	Sarstedt (Nümbrecht)
Cell culture Petri dish 100mm (Nunclon Delta-treated)	Nunc/Thermo Fisher (Langenselbold)
6-well plates	Sarstedt (Nümbrecht)
12-well plates	Sarstedt (Nümbrecht)
24-well plates	Sarstedt (Nümbrecht)
384-well plates	4titude (Berlin)
6-well plates	Nunc (Langenselbold)

96-well plates	Nunc (Langenselbold)
2-well cell culture inserts	Ibidi (Gräfelfing)
BD Microlance 3	Becton Dickinson (Heidelberg)
Brain surface coil	Bruker (Ettlingen)
Breath sensors	Thermo Fisher Scientific (Waltham)
Cell culture flasks (25, 75, 175 cm^2)	Sarstedt (Nümbrecht)
Cell scrapper 25 cm	Sarstedt (Nümbrecht)
Centrifuge tubes (15, 50 ml)	Sarstedt (Nümbrecht)
Chamber slides (8 wells)	Thermo Fisher Scientific (Waltham)
Circulator bath	Thermo Fisher Scientific (Waltham)
Comb columns	Bio-Rad (Feldkirchen)
Combitips advanced (0.1 ml)	Eppendorf (Hamburg)
Cover glasses (18x18 mm)	Carl Roth (Karlsruhe)
Cuvettes	Sarstedt (Nümbrecht)
Dubois decapitation scissors	Hermle (Tuttlingen)
ES-Compresses	Hartmann (Heidenheim)
FilterTips (10 / 100 / 1000 µl)	Starlab (Hamburg)
Glass Pasteur Pipetter (150, 230 mm)	Carl Roth (Karlsruhe)
Hamilton microliter syringe 701 N (10 µl)	Hamilton (Reno, USA)
Metallic spacer (3.8 mm diameter)	Kig GmbG (Kirkel)
Microscope slides (25 x 75 x 1 mm)	Carl Roth (Karlsruhe)
Noyes eye scissors	Hermle (Tuttlingen)
OD24 OxoDish®	PreSens (Regensburg)
Pipette tips (10 / 100 / 1000 µl)	Eppendorf (Hamburg)
Polycarbonate membrane inserts (6-Well, 0.4µm pore size)	BD Falcon (Heidelberg)
Reaction tubes (0.2, 0.5, 1.5, 2 ml)	Sarstedt (Nümbrecht)
Rotilabo Blotting papers (1.5 mm)	Bio-Rad (Feldkirchen)
PCR soft tubes (0,2 ml)	Biozym (Wien)
qPCR adhesive sealing foil	4titude (Berlin)
SafeSeal tube (1,5, 2ml)	Sarstedt (Nümbrecht)
Semkin standard forceps	Hermle (Tuttlingen)
Seralon polyamide suture (DR-009, USP 7/0, EP 0.5)	Serag-Wiessner GmbH (Naila)
Serological pipettes (2, 25ml)	Sarstedt (Nümbrecht)
Serological pipettes (5ml)	Corning (Kaiserslautern)
Serological pipettes (10, 50ml)	Greiner Bio-One (Kremsmünster)
Sterican needle Gr. 17, 18, 20	B. Braun (Melsungen)
Steritop-Filter (0.22 µm pore size)	Sarstedt (Nümbrecht)
Syringe (5, 10 ml)	Becton Dickinson (Heidelberg)
Tail vein catheter	Sigma-Aldrich (Darmstadt)
Tissue forceps	Hermle (Tuttlingen)

Wecker spatula	Hermle (Tuttlingen)
Whatman qualitative round filter paper (90 mm diameter)	GE Healthcare (Buckinghamshire, UK)

2.1.9. Equipment

All laboratory equipment used during this study is listed in Table 9.

Table 9. Equipment.

Product	**Label**	**Company**
-80°C Ultra-Low temperature Freezer	New Brunswick U725-G Innova	Eppendorf (Hamburg)
4°C Fridge	KUw 1740	Liebherr (Ochsenhausen)
4°C Fridge	RP 1218	Electrolux (Nürnberg)
4°C Fridge	LKPv 6520 MedLine	Liebherr (Ochsenhausen)
4°C/-20°C Freezer combination	KGK 3212	Liebherr (Ochsenhausen)
-20°C Freezer	GUw 1213	Liebherr (Ochsenhausen)
-20°C Freezer	GS 2483	Liebherr (Ochsenhausen)
-20°C Freezer	Privileg 4059	Whirlpool Corporation (Michigan, USA)
Analytical balance	CP124S	Sartorius(Göttingen)
Autoclave	Fedegravi FV A3/A1	IBS (Fernwald)
Automatic flake ice machine	ZBE 70-35	Ziegra (Isernhagen)
Biological safety cabinet	HeraSafe HS12	Heraeus Instruments (Hanau)
Biological safety cabinet	CA/RE5	Clean Air (Utrecht, NL)
Block thermostat	HLC BT1303	SEL Laboratory Products (England)
Cell counting chamber	Neubauer Improved	LO Laboroptik (Marienfeld)
Centrifuge	Biofuge Fresco 17	Thermo Fisher Scientific (Waltham)
Centrifuge	Megafuge 3.0R	Heraeus Instruments (Hanau)
Centrifuge	Megafuge 1.0	Heraeus Instruments (Hanau)
Chemical balance	EHA 500-2	Kern (Lörrach)
Chemiluminescence system	ImageQuant LAS-500	GE-Healthcare (Chicago)
CO2 incubator	BB 6220	Heraeus Instruments (Hanau)
Cooling plate	CP 60	Microm (Neuss)
Drying cabinet	UM 200	Memmert (Schwabach)
Ductless recirculating fume hood	CaptairBio I-130	Erlab (Val de Reuil)
Confocal laser scanning microscope	FV3000	Olympus (Hamburg)
Flow Cytometer	LSR II	Becton Dickinson (Heidelberg)
Flow Cytometer	Calibur	Becton Dickinson (Heidelberg)
Live fluorescence microscope	Zeiss Axio Observer Z.1	Zeiss (Oberkochen)

Gel imaging system	Gel Doc XR+	Bio-Rad (Feldkirchen)
Horizontal gel electrophoresis system	Wide Mini-Sub® Cell GT	Bio-Rad (Feldkirchen)
Laminar flow hood	Herasafe HS18	Heraeus Instruments (Hanau)
LightCycler	QuantStudio 5, 384-well	Thermo Fisher Scientific (Waltham)
Light/fluorescence microscope	EVOS FL	Thermo Fisher Scientific (Waltham)
Magnetic stirring bar retriever	MR3001	Heidolph Instruments (Schwabach)
Microliter pipettes	100–1000µl, 20–200µl, 2–20µl, 0.2–2µl	Gilson/Eppendorf (Hamburg)
Microscopy tissue processor	LYNX	Reichert-Jung (Wetzlar)
Microtome	Reichert Ultracut S	Leica-Reichert (Wetzlar)
Microwave	M504	Whirlpool (Stuttgart)
Mini shaker	IKA MS2	IKA Lab equipment (Staufen)
Mr. Frosty	Mr.Frosty	Nalgene (Rochester, USA)
MRI scanner	7T	Bruker BioSpin (Ettlingen)
Multiscan FC		Thermo Fisher Scientific (Waltham)
N2 Tank	LC-189L	Taylor-Wharton (Shah Alam, Malaysia)
pH meter	538 MultiCal	WTW (Dublin)
Oxygraph-2k	O2k-Series	Oroboros Instruments (Innsbruck)
Horizontal shaker	KS 260 Basic	IKA (Staufen)
Power supply	Standard Power Pack P25	Biometra (Göttingen)
Roller shaker	RS-TR05	Phoenix Instrument (Garbsen)
SensorDish® Reader (SDR)	SDR v3	PreSens (Regensburg)
Single-lens reflex camera	Canon EOS 600D	Canon (Tokio)
Slides scanner system	Pannoramic 250	Sysmex (Hamburg)
Sliding microtome	HM 400 R	Microm (Neuss)
Spectrophotometer	NanoDrop 1000	Thermo Fisher Scientific (Waltham)
Stereotaxic drill	Jacobs Chuck (18,000 rpm)	Kopf Instruments (Bergisch Gladbach)
Suction pump	Vacusafe	Integra Biosciences (Biebertal)
Thermal cycler	PTC-200	MJ Research (Waltham)
Tissue float bath	GFL 1052	GFL (Burgwedel)
Transmission electron microscope	LEO 912AB	Zeiss (Oberkochen)
Ultra-precise small animal stereotaxic instrument	Model 963	Kopf Instruments (Bergisch Gladbach)
Vortex shaker	RS-VA 10	Phoenix Instruments (Garbsen)
Vortex shaker	IKA MS2 Minishaker	IKA-Werke (Staufen)
Vortex shaker	IKA MS3 Digital Shaker	IKA-Werke (Staufen)

Vortex shaker	Vortex Genie 2	Scientific Industries (USA)
Water bath	WNB 7	Memmert (Schwabach)

2.1.10. Software and databases

All software and databases used during this study are listed in Table 10.

Table 10. Software and databases.

Product	**Purpose**	**Company**
BioGPS (database)	Database for gene and protein function	BioGPS
BioRender	Scientific Figure Making	BioRender
CaseViewer (version 2.3)	Imaging editor for slide images	3DHISTECH Ltd.
EndNote (version X8.2)	Citation program	Clarivate Analytics
FACS software	FACSDiva™	Becton Dickinson
FACS software	CellQuest Pro	Becton Dickinson
FACS analysis software	FlowJo	Becton Dickinson
FV31S-SW software.	Imaging processing editor for confocal images	Olympus
Gen Card (version 5.3)	Database for gene and protein function	Life Map Sciences
GraphPad Prism (version 10)	Graphs and statistics	GraphPad Software
Heatmapper (online tool)	Creating heatmaps	omicX
Image Lab (on device)	Image analysis of agarose gels	Bio-Rad
ImageJ (win64) (version 1.51s)	Analyzing data, editing pictures	Wayne Rasband
ImageQuant LAS 4000 (on device)	Chemiluminescence imaging	Fujifilm
Microsoft Office 2019	Managing data, writing text, editing pictures	Microsoft
NanoDrop (on device)	DNA/RNA measurement	Thermo Fisher Scientific
NCBI (database)	Database for genomic information, BLAST tool	NCBI
PerlPrimer (version 1.1.21)	Designing primers	Marshall, 2004

2.2. Methods

2.2.1. Cell culture methods

2.2.1.1. Maintenance of tumor cells

The E0771-LG cell line, a highly metastatic subclone derived from experimental lung metastases of the parental E0771 breast cancer line [RRID:CVCL_GR23], was kindly provided by Prof. J. Pollard (University of Edinburgh, UK). The CMT93Var cell line, a metastatic subclone of the murine colorectal carcinoma CMT93 [RRID:CVCL_1986], was obtained from Prof. Dr. C. Hackl (University Hospital Regensburg, Germany). The KPN cell line, a murine colorectal cancer line derived from C57BL/6 mice, was provided by Prof. E. Naschberger (University of Erlangen, Germany). The 99LN-BrM breast cancer cell line, selected for brain tropism via one round of *in vivo* selection, was generously provided by Prof. L. Sevenich (Goethe University Frankfurt, Germany).

All cell lines were cultured in DMEM (Merck Millipore, Berlin, Germany) supplemented with 10% fetal calf serum (FBS, Bio&Sell, Nürnberg, Germany) at 37 °C in a humidified atmosphere containing 5% CO_2.

In order to passage the cells, they were washed once with PBS (Gibco/Thermo Fisher Scientific), detached by incubation with 1mL Trypsin-EDTA (1x) (Sigma-Aldrich) for 5-10 min. The detached cells were resuspended in 9ml of DMEM + 10% FCS and counted. The appropriate volume of cells was then diluted with DMEM + 10% FCS to a final volume of 10ml.

To maintain cells over a longer period of time, they were frozen in DMSO (Sigma-Aldrich) with 90% FCS (Bio&Sell) and stored in liquid nitrogen. Mycoplasma contamination was routinely tested and excluded for all experiments.

2.2.1.2. Primary cell isolation and culture

2.2.1.2.1. Primary cultures of BMDMs

BMDMs were isolated from 10- to 12-week-old C57BL/6 wildtype (WT) and TREM2 knockout (KO) mice, following a slightly modified protocol based on (Reiling et al. 2001). Mice were euthanized via CO_2 asphyxiation, and the skin on the hind limbs was disinfected with 70% ethanol. Incisions were made on both hind legs, and the skin and muscle tissue were removed using sterile scissors and forceps (Hermle). The femurs were harvested by distal

dissection at the knee joint, followed by careful dislocation of the femoral head from the hip socket. Extracted femurs were immersed in 70% ethanol and cleaned using sterile compresses (Hartmann) to remove residual tissue.

Under sterile conditions, the bone marrow cavity was exposed by trimming the ends of the femur and flushed using Pluznik medium in a coated petri dish (Nunc) with a fine 17G needle (B. Braun). Coated dishes allowed adherent cells such as fibroblasts and osteoclasts to attach to the surface, whereas macrophage progenitors remained in suspension. After 24 hours of incubation at 37°C and 5% CO_2, the supernatant containing non-adherent progenitor cells was collected and centrifuged at 1200 rpm for 10 minutes at room temperature. The resulting cell pellet was resuspended in 40 mL of Pluznik medium (see Table below) and seeded into four uncoated petri dishes (Sarstedt). Cells were cultured for six days to allow differentiation into mature BMDMs. Medium was refreshed after 72 hours. On day seven, BMDMs were harvested by incubation with 1 mL Accutase (Sigma-Aldrich) and reseeded in BMDM-culture medium (see Table below). Both culture media were supplemented with L929-conditioned medium, which provides macrophage colony-stimulating factor (M-CSF), an essential cytokine that promotes the differentiation of bone marrow progenitors (monocytes) into macrophages. The fully differentiated macrophages were detached with Accutase and could be checked for via FACS for quality control and used in further experiments.

The L929 conditioned medium which was used in Pluznik and culture media was obtained by incubating murine fibroblasts of the L929 cell line for 7 days under standard settings and collecting the supernatant, which was then centrifuged and filtered before being stored at -20°C.

Table 11. Composition of cell culture mediums for BMDM isolation.

Pluznik Medium	BMDM- culture medium
DMEM (Glucose 1g/l, with stable Glutamine)	DMEM (Glucose 1g/l, with stable Glutamine)
30% L929 conditioned medium	15% L929 conditioned medium
10% Fetal bovine serum	10% Fetal bovine serum
5% Normal horse serum	
0,2% 2-Mercaptoethanol	
1% Sodium pyruvate	

2.2.2. Functional in vitro assays

2.2.2.1. Hanging Drop assay

The ability of cancer cells to form a spheroid in anchorage-independent conditions and its subsequent outgrowth were analyzed by spheroid formation assays using the hanging drop method and prior immunofluorescence staining. First, a single cell suspension (5 x 10^4 / 1 ml) was prepared. The tumor single cell suspension was stained with Cytopainter green/red 1:50 (Abcam) for 40 min. Subsequently the tumor cells and BMDMs were stained with DAPI 1:500 5 min. The bottom of a 100 mm cell culture dish was filled with 10 ml PBS to act as a hydration chamber. The lid was inverted and 25 µl drops of the cell suspension were placed onto it with sufficient distance between them. The lid was carefully inverted, placed onto the PBS-filled bottom chamber and incubated for 72h (Day-3,-2,-1 and 0) leading to the formation of spheroids in those hanging drops. Spheroids formation was visualized every 24h and photographs were taken from (Day −3 to Day 0) using an EVOS FL microscope.

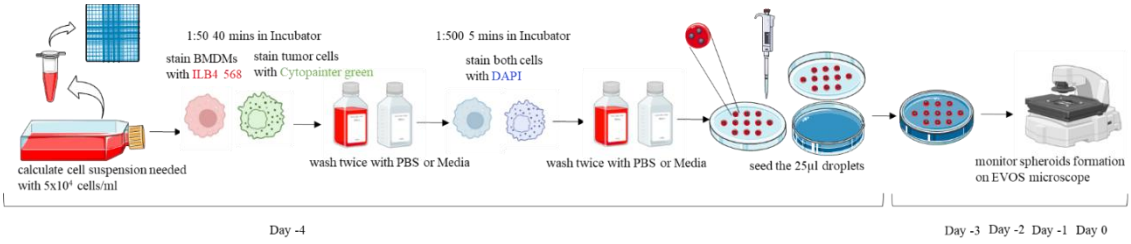

Figure 8. Schematic illustartion of the Hanging drop assay. Image created with Biorender.com.

2.2.2.2. Migration assay

The migratory capacity of tumor cells and BMDMs was assessed using migration assays with 2-well cell culture inserts. Inserts were placed into 24-well plates, and 5 x 10^4 BMDMs and tumor cells were seeded into the right and left compartments, respectively, and incubated for 24 h until confluence was reached. The following day, the inserts were removed, and cells were allowed to migrate for up to 72 h. Images of migrated cells were acquired at 24 h (startpoint) and 72 h (endpoint) using an EVOS FL microscope.

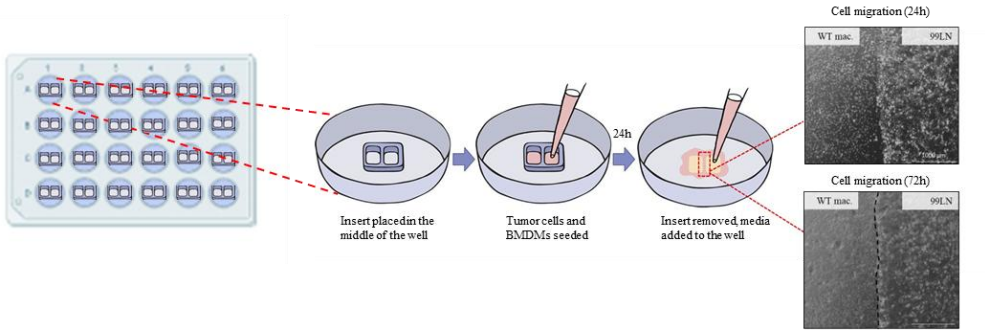

Figure 9. Schematic illustration of the migration assay. Image adpoted from (Sultan et al. 2019) and edited with Biorender.com.

2.2.3. *In vivo* experiments

2.2.3.1. Stereotactical intracerebral injection

BM experiments were conducted using 10- to 12-week-old C57BL/6 WT and TREM2 KO mice, as described (Alves de Lima et al. accepted). Tumor cells were stereotactically implanted into the brain following intraperitoneal anesthesia using a ketamine-domitor-based cocktail (administered at 10 µL per gram of body weight; see Table 12). To ensure local analgesia, lidocaine was administered subcutaneously at the surgical site prior to the procedure. The scalp was then disinfected using 70% ethanol and a small midline incision was made using a sterile scalpel to expose the skull. The periosteum over the right parietal bone was gently removed, and the animal was secured in a stereotactic frame (David Kopf Instruments) using ear bars to ensure proper alignment. A craniotomy was performed using a precision drill (David Kopf Instruments), targeting coordinates 1 mm lateral and 2 mm rostral to the bregma. A small burr hole (~1 mm diameter) was drilled carefully, avoiding damage to the underlying dura. Tumor cells were prepared immediately prior to injection. Cells were trypsinized, counted using a Neubauer chamber, centrifuged, and resuspended in 3 µL of a 2:1 ECM-to-medium gel matrix (2 µL ECM gel, 1 µL culture medium). The suspension was loaded into a 10 µL Hamilton syringe fitted with a beveled needle. The syringe was mounted vertically into the stereotactic holder, with the bevel facing left. The needle was lowered 3.5 mm into the brain parenchyma and then retracted 0.5 mm to create a deposition space. The 3 µL of tumor cell suspension was injected slowly over the course of one minute, and the needle was left in place for an additional two minutes to allow for stabilization of the injected material. Following injection, the skull was rinsed with sterile NaCl. The skin incision was closed using polyamide sutures (Seralon, Serag-Wiessner GmbH). Postoperative analgesia was provided by subcutaneous administration

of a diluted painkiller solution (5 µg/g body weight), and the animals were placed on a heated recovery pad (Medax) until full awakening from anesthesia.

Table 12. Composition of anesthetic solution and painkiller for stereotactical intracerebral injection of tumor cells.

Anesthetic solution	Painkiller
Ketamin 100 mg/ml	Lidocaine 5mg/ml
Domitor 0,25 mg/ml	Rimadyl 5mg/ml
NaCl ad 10ml	

2.2.3.2. Post-Injection monitoring and Neurological Assessment

Following intracerebral tumor cell delivery via stereotactic injection, mice were closely monitored for signs of neurological or physical decline. Clinical observation focused on changes in behavior, overall condition, body weight, and motor performance. Body weight was recorded biweekly to detect progressive deterioration. If mice exhibited indications of neurological impairment or motor dysfunction, a Hanging Wire test was performed to assess neuromuscular strength, coordination, and spatial orientation, functions often compromised in the context of metastatic progression within the brain (Alves de Lima et al. accepted).

2.2.3.2.1. Tissue Collection and Perfusion Procedure

Symptomatic and surviving mice were sacrificed for organ-specific downstream analyses through transcardial perfusion with PBS. Prior to perfusion, mice were deeply anesthetized using a combination of 10% Ketamine and 2,5% Domitor. Once full anesthesia was confirmed, a midline incision was made in the abdomen, and the thoracic cavity was opened. The peritoneal tissue was carefully removed to expose the heart. The rib cage was then gently fractured to improve access and visibility.

The heart was stabilized with forceps, and a perfusion needle was inserted into the left ventricle. Simultaneously, a small incision was made in the right atrium to allow blood to exit. PBS was then slowly infused to flush the circulatory system, effectively removing blood from both peripheral organs and cerebral vessels, thereby facilitating brain preservation.

Immediately following perfusion, the animal was decapitated. The brain was carefully extracted from the skull; olfactory bulbs were removed, and the anterior brain region was dissected for molecular studies. These anterior brain samples were snap-frozen in liquid nitrogen and stored at –80 °C for later RNA extraction and gene expression profiling via quantitative real-time PCR (qRT-PCR) (see Section 2.2.6.1.4).

The remaining brain tissue was fixed in 4% paraformaldehyde (PFA) for 48 hours, washed in PBS, and stored until paraffin embedding for subsequent immunohistochemistry (IHC) allowing the further characterization of the HGPs. Additionally, peripheral organs including the liver, lungs, and spleen were collected and preserved under similar conditions to support potential future analyses beyond the current project scope.

2.2.4. Flow cytometry methods

Flow cytometry utilizes a process called hydrodynamic focusing to create a single file line of cells. The cells are then differentiated according to size (forward scatter), granularity (side scatter) and specific markers (using fluorescent antibodies). In this study, BMDMs were detached from the plate according to 2.2.1.2.1 and resuspdended in DMEM + 10% FCS beforebeing centrifuged. All centrifugation steps were carried out at 1200 rpm, 5 min, 4 °C. The samples were first gated by forward (FSC) against side scatter (SSC) as a way to exclude cellular debris, then by FSC-A against FSC-H to ensure that only single cells are measured, before gating the cells by different antigens of interest. An unstained sample was measured to account for the autofluorescence of the cells and isotype antibodies were used to control to determine the non-specific binding of an antibody to Fc receptors. The acquisition of stained cells was performed with the BD FACS Calibur or Flow Cytometer LSR II instrument.

2.2.4.1. Flow-cytometric determination of the BMDM purity

In order to evaluate the efficacy of the BMDM differentiation protocol, flow cytometry was performed on day 1 and day 7 of the protocol (see Methods 2.2.1.2.1.). BMDMs were detached and resuspended in DMEM + 10% FCS before being centrifuged. The pellet was resuspended in PBS + 2% FCS and counted. $2x10^5$ cells were then put in each FACS-tube. Antibodies were added in excess (< 0,25 µg per-10^6 cells) and the cells were incubated for 30 minutes at 4°C. 1ml of PBS per FACS tube was added and the tubes were centrifuged at 1.200 rpm (room temperature or 4°C). After this, the supernatant with the antibodies that had not bound to their respective antigens was discarded and the cells were resuspended in PBS + 2% FCS to a final concentration of $1x10^6$ cells per ml for an optimal flow rate, with a minimal volume of 200-300µl. The cell suspension was filtered through 35µm filter before starting the actual flow cytometry. In order to correct for overlapping emission spectra, compensation was applied, meaning that some tubes were each stained with only one of the different fluorophores bound to antibodies specific for a ubiquitous antigen (in this case CD45). An unstained sample was

measured to account for the autofluorescence of the cells and isotype antibodies were used to control to determine the non-specific binding of an antibody to Fc receptors.

2.2.4.2. Flow-cytometric determination of the surface lipid proteins

The surface lipid proteins on BMDMs were assessed using the cluster of differentiation 36 also known for platelet glycoprotein 4 (CD36, Biolegend) and cluster of differentiation 9 known as tetraspanin (CD9, Biolegend). For this, $1x10^5$ cells/staining were washed with DPBS and resuspended in 1 ml DMEM + 10% FCS before being centrifuged. The pellet was resuspended in PBS + 2% FCS and counted. $1x10^5$ cells were then put in each FACS tube. Antibodies were added in excess (< 0,25 µg per 10^6 cells) and the cells were incubated for 30 minutes at 4°C. Cells were washed with PBS + 2% FCS to a final concentration of $1x10^5$ cells in 200/300µl. An unstained sample was measured to account for the autofluorescence of the cells and isotype antibodies were used to control to determine the non-specific binding of an antibody to Fc receptors.

2.2.4.3. Flow-cytometric determination of the cellular mitochondrial mass

Determination of mitochondrial mass was conducted in collaboration with the Christian Wetzel group employing MitoTracker Green FM for fluorescence-based quantification. For this, $0.5x10^6$ cells/staining were washed with DPBS and resuspended in 1 ml cell culture medium without serum. Cells were treated with 1.5 µM Cyclosporine A and 10 nM Mitotracker Green FM and incubated for 1–2 h under cell culture conditions. Afterwards, cells were washed in FACS washing buffer, resuspended in 300 µl FACS washing buffer and measured. An unstained sample was measured to account for the autofluorescence of the cells and isotype antibodies were used to control to determine the non-specific binding of an antibody to Fc receptors.

2.2.5. Cell-culture based techniques for metabolic analysis

2.2.5.1. Measurment of cellular oxygen consumption

Oxygen consumption was evaluated using PreSens optical oxygen sensing technology in collaboration with the Kathrin Renner-Sattler research group. $0{,}5x10^6$ cells were seeded into OD24 OxoDish® plates (PreSens Precision Sensing GmbH, Regensburg, Germany) and maintained under standard cell culture conditions, including basal, ApoE-stimulated 1µg/ml, and LPS-stimulated 10 ng/ml conditions for 24h. Oxygen levels in the culture medium were monitored non-invasively using the SensorDish® Reader (SDR) system, enabling real-time measurement of oxygen consumption in live cells.

2.2.5.2. Lipidomic analysis of isolated BMDM

BMDMs were isolated following the protocol previously described (see Methods 2.2.1.2.1). On day 7 after isolation, 1 x 10^6 cells were seeded into 6-well plates. Once the cultures reached 90–100% confluency the following day, cells were stimulated with ApoE (1 µg/ml) and LPS (10 ng/ml) and incubated for 24 hours. After stimulation, cell lysates were prepared for lipidomic analysis. The culture medium was removed, cells were washed 2–3 times with PBS, and 200 µl of 0.2% SDS in water plus 200 µl water were added. The lysates were then transferred to 1.5-ml Eppendorf tubes and immediately frozen at –20°C. Quantitative lipidomics was carried out in collaboration with the group of Gerhard Liebisch. Internal standards were added prior to lipid extraction, and 100 µg of total protein was processed using the extraction method described by (BLIGH and DYER 1959, 1959). Lipid analyses were carried out by direct flow injection analysis (FIA) using both a triple quadrupole mass spectrometer (FIA-MS/MS) and a high-resolution hybrid quadrupole-Orbitrap mass spectrometer (FIA-FTMS). FIA-MS/MS measurements were performed in positive ion mode according to the analytical setup and procedures described by (Liebisch et al. 2004).

2.2.6. Gene expression analysis

2.2.6.1. RNA methods

2.2.6.1.1. Isolation of total RNA from murine tissue samples

Total RNA was extracted from murine brain metastasis tissue using TRIzol reagent (Invitrogen) following a modified phenol-chloroform-based protocol. Small frozen tissue pieces were homogenized in 1 mL of TRIzol, after which 200 µL of chloroform (Carl Roth) was added. The samples were mixed thoroughly and incubated at room temperature for 5 minutes to allow phase separation. After centrifugation at 17,000 x g for 15 minutes at 4 °C, the upper aqueous phase, containing the RNA, was carefully collected and transferred to a fresh tube. To this, 500 µL of isopropanol was added, followed by incubation for 10 minutes at room temperature to facilitate RNA precipitation. The samples were then centrifuged again at 13,000 x g and 4 °C for 30 minutes. The resulting RNA pellet was washed with 1 mL of 70% ethanol by spinning at 20,000 x g for 5 minutes at 4 °C, air-dried for 5–10 minutes, and subsequently resuspended in 50 µL of DNA digestion solution to remove any residual genomic DNA. Digestion was performed at 37 °C for 20 minutes. To purify the RNA further, 150 µL of nuclease-free water and 200 µL of phenol/chloroform/isoamyl alcohol (Carl Roth) were added. After vortexing for 30 seconds and centrifugation at 17,000 x g for 2 minutes at 4 °C, the aqueous phase was again carefully collected. Sodium acetate (20 µL, 3 M, pH 4.8) and 200 µL of isopropanol were added to precipitate the RNA, followed by a 30-minute incubation at 4 °C and centrifugation for another 30 minutes at 17,000 x g. The RNA pellet was washed twice with 1 mL of 70% ethanol (5 minutes each at 17,000 x g, 4 °C), then air-dried and dissolved in 20 µL of nuclease-free water. Finally, RNA purity and concentration were determined using a NanoDrop ND-1000 spectrophotometer (Thermo Fisher Scientific), and samples were stored appropriately for downstream qPCR analysis.

<u>DNA digestion mix:</u>

- DNase I (10 U/µl, Roche) 1 µl
- RNase OUT (40 U/µl, Invitrogen) 0.5 µl
- DNase I incubation buffer (10x, Roche) 5 µl
- Nuclease-free water ad 50 µl

2.2.6.1.2. Isolation of mRNA from cultured cells

Messenger RNA (mRNA) was isolated from cultured cells using the High Pure RNA Isolation Kit (Roche), following the manufacturer's protocol. For each extraction, 0.5 x 10^6 cells were plated in 6-well culture dishes and incubated overnight under standard conditions (37 °C, 5% CO_2) to allow adherence. After a single PBS wash to remove non-adherent cells and debris, the adherent cells were lysed directly in the well using 400 µL of lysis/binding buffer supplemented with 200 µL of PBS. This buffer, containing guanidine hydrochloride, RNase inhibitors, and the detergent Triton X-100, facilitated rapid membrane disruption and protein denaturation. Following lysis, the mixture was vortexed for 15 seconds to ensure homogeneity, then transferred to a spin column containing a glass fiber matrix. The column was centrifuged at 8000 x g for 15 seconds, during which cellular debris and proteins passed through, while nucleic acids remained bound to the matrix. Genomic DNA contamination was subsequently eliminated via on-column digestion using DNase I, applied for 15 minutes at room temperature. After enzymatic digestion, the column was washed three times to remove residual contaminants. Finally, the purified RNA was eluted in 50 µL of nuclease-free water. RNA concentration and purity were assessed spectrophotometrically using the NanoDrop ND-1000 (Thermo Fisher Scientific) prior to downstream applications.

2.2.6.1.3. Reverse transcription

qRT-PCR was employed to assess gene expression alterations. To generate complementary DNA (cDNA), total RNA isolated from the samples was reverse transcribed using the iScript cDNA synthesis kit (Bio-Rad). The reverse transcription reaction relies on a reverse transcriptase enzyme that initiates synthesis by annealing to both random hexamer primers and oligo(dT) primers included in the kit. These primers facilitate the conversion of eukaryotic mRNA, characterized by a poly-A tail, into cDNA. For each sample, 1 µg of RNA was combined with 4 µL of 5x iScript reaction mix and 1 µL of reverse transcriptase, and the volume was adjusted to 20 µL using nuclease-free water. The reaction mixture was incubated in a thermal cycler (PTC-200, MJ Research) under the following conditions: 5 minutes at 25 °C for primer annealing, followed by a 30-minute incubation at 42 °C to allow cDNA synthesis. The final step involved heating to 85 °C for 5 minutes to inactivate the enzyme and terminate the reaction. After cooling, the resulting cDNA was diluted 1:5 in nuclease-free water and stored at −20 °C until further use in downstream gene expression analyses.

2.2.6.1.4. Quantitative real-time PCR (qRT-PCR)

qRT-PCR was employed to assess differential gene expression levels. This technique builds on the core principles of conventional PCR, with the added advantage of real-time monitoring through the use of SYBR Green, a DNA-binding dye that fluoresces upon intercalation with double-stranded DNA. The dye absorbs light at 497 nm and emits fluorescence at 520 nm, enabling real-time tracking of DNA amplification during the PCR cycles. To initiate the reaction, hot-start iTaq DNA polymerase was activated at 95 °C for 12 minutes. Amplification was then conducted over 40 cycles, each consisting of denaturation at 95 °C for 15 seconds, followed by annealing and extension at 60 °C for 1 minute. The accumulation of PCR product during each cycle directly correlated with the increase in SYBR Green fluorescence. The cycle threshold (Ct), defined as the cycle number at which fluorescence surpasses a predefined threshold, was calculated for each target gene and normalized to the expression levels of the housekeeping genes *Gapdh* and *Pgk1* (ΔCt). To confirm the specificity of amplification, a melting curve analysis was performed at the end of the qRT-PCR run by gradually increasing the temperature and continuously recording the fluorescence, allowing detection of potential nonspecific products or primer dimers. Primers used in this study were designed based on the strategy described in Section 2.2.6.1.4.1 and are listed in Table 6. The PCR reaction mix consisted of 5.6 µL iTaq Universal SYBR Green Supermix, 0.6 µL of a forward/reverse primer mix (10 µM each), and 1.8 µL nuclease-free water per well. For each sample, 8 µL of this mix was dispensed in triplicate into a FrameStar 384-well plate (4titude), followed by the addition of 2 µL of cDNA template (10 ng; 1:1 diluted in nuclease-free water).

After sealing, the plate was briefly centrifuged at 400 g for 5 minutes at 4 °C and subjected to amplification using the QuantStudio 5 Real-Time PCR System. Data were analyzed with the QuantStudio Design & Analysis software (Thermo Fisher). Each run included negative controls, both no-template and no-primer controls, to ensure the reliability and specificity of the assay.

Table 13. Protocol of qRT-PCR program.

Step	Temperature	Time	Cycles
Activation of Taq DNA polymerase:	95°C	12 min	
Denaturation:	95°C	15 s	40
Annealing and elongation:	60°C	1 min	40
Melting curve analysis:	95°C	15 s	
	60-95°C	2°C/min	

2.2.6.1.4.1. Establishment of primers for qRT-PCR reactions

Primer pairs for qRT-PCR were designed using PerlPrimer software (version 1.1.2.1, SourceForge.net). Since the ΔCt method assumes 100% amplification efficiency, it is essential to evaluate primer efficiency before conducting relative gene expression analyses. To achieve this, multiple primer pairs for each gene of interest (GOI) were designed and experimentally tested to identify those that demonstrate near-perfect amplification efficiency.

Primer efficiency testing was performed using positive control samples identified from the BioGPS database, which lists cell lines and tissues with high expression of the respective GOI. Serial dilutions of cDNA from these controls, with known concentrations, were prepared and subjected to qRT-PCR as outlined previously (see section 2.2.6.1.4). The resulting Ct values were plotted against the logarithm of the input cDNA quantity. The slope of this standard curve was calculated by the QuantStudio Design & Analysis software, where a slope of –3.33 corresponds to 100% primer efficiency, indicating a doubling of product with each PCR cycle. Only primer pairs with efficiencies between 90% and 110% were selected for subsequent gene expression experiments.

2.2.6.2. DNA methods

2.2.6.2.1. Isolation of total DNA from eucaryotic cells

Genomic DNA was extracted from eukaryotic cells using a microcentrifuge-based protocol following the QIAamp DNA Mini Blood Kit instructions (QIAGEN). Cells grown as monolayers in 6-well plates were detached using a cell scraper. Up to 5 x 10^6 cells were collected into 1.5 ml microcentrifuge tubes and centrifuged at 300 x g for 5 minutes. After carefully discarding the supernatant without disturbing the pellet, the cells were resuspended in PBS to a final volume of 200 µl. For protein digestion, 20 µl of Proteinase K was added, followed by 200 µl of AL buffer to lyse the cells efficiently. The mixture was vortexed briefly for 15 seconds and incubated at 56°C for 10 minutes. The tube was then centrifuged briefly before adding 200 µl of 96–100% ethanol. After mixing for 15 seconds and a short centrifugation, the sample was applied to a spin column placed in a 2 ml collection tube and centrifuged at 6000 x g for 1 minute. The spin column was transferred to a fresh collection tube and washed with 500 µl of AW1 buffer, ensuring the buffer did not wet the column's rim. This was followed by centrifugation at 6000 x g for 1 minute to remove contaminants. Next, the column was moved to a new collection tube, and 500 µl of AW2 buffer, an ethanol-based wash solution, was added to remove residual salts. This step was centrifuged at maximum speed

(~17,000 x g) for 2 minutes. To minimize carryover of AW2 buffer, the spin column was placed in another fresh tube and centrifuged again at maximum speed for 1 minute. For elution, the spin column was placed into a clean 1.5 ml microcentrifuge tube, and DNA was eluted three times with 50 µl AE buffer each time. Each elution step included a 5-minute incubation at room temperature (15–25°C) prior to centrifugation at 6000 x g for 1 minute to maximize DNA recovery.

DNA concentration and purity were assessed using a NanoDrop ND-1000 spectrophotometer (Thermo Fisher Scientific), yielding approximately 150 ng/µl from 10^6 cells. Finally, the purified DNA was stored long-term at –30 to –15°C in AE buffer.

2.2.6.2.2. Isolation of total DNA from tissue samples

The Monarch Genomic DNA purification Kit (New England Biolabs) was used to purify DNA from murine ear and brain metastasis tissue samples. First, murine ear tissue was weighed and limited to a maximum of 10 mg. The tissue was cut into small fragments, placed in a 1.5 ml microcentrifuge tube, and digested with 3 µl of Proteinase K and 200 µl of tissue lysis buffer. To improve homogenization, the samples were mechanically disrupted using tissue grinding pestles. Then, tissues were incubated at 56°C for 30-60 min a thermal mixer with agitation at full speed (1400 rpm) until tissue pieces have completely dissolved. After incubation, the tubes were briefly centrifuged to collect any condensation from the lid. Subsequently, 400 µl of binding Buffer containing guanidine salts was added to enhance binding to the spin column and detergent action. The mixture was pulse-vortexed for 5-10 seconds. The lysate was transferred to a purification column pre-inserted into a collection tube then subjected to a series of washes: first, 500 µl of gDNA Wash Buffer was added, and the sample was centrifuged at maximum speed for 1 minute; second, the sample was washed again with 500 µl gDNA wash buffer at maximum speed for 1 minute. The tube containing the filtrate was discarded after each centrifugation, while the spin column was retained. To complete the washing phase, the spin column was transferred to a fresh 1.5 ml collection tube and centrifuged at maximum speed for 1 minute to remove residual wash buffer. DNA was eluted by adding 50 µl of preheated (60°C) gDNA elution buffer to the spin column, incubated 1 min at room temperature and then centrifuged at maximum speed for 1 minute. To maximize DNA yield, this elution step was repeated three times, with a 5-minute incubation at room temperature before each centrifugation.

2.2.6.2.3. Conventional PCR

Validation of genetic modification in mice was performed using Polymerase Chain Reaction (PCR). This biochemical technique detects the presence or absence of specific genomic DNA sequences by amplifying target DNA regions. All procedures were conducted on ice to preserve sample integrity. Following DNA isolation (see sections 2.2.6.2.1 and 2.2.6.2.2), the essential components for PCR were combined in a standard master mix (MM) (see Table 14). The reaction mixture was initially heated to 94°C to denature the double-stranded DNA, separating it into single strands (initial denaturation). Then, a thermostable DNA polymerase enzyme (PAN-Taq) synthesized complementary DNA strands by incorporating deoxynucleotide triphosphates (dNTPs) during the annealing step. The process was repeated in a thermocycler, which rapidly cycles through denaturation, annealing, and elongation phases 30 to 40 times over approximately 2 hours. This amplification results in more than a billion copies of the original target DNA sequence.

Table 14. List of essential components included in the master mix (MM) for the PCR. Final volume of 20 µl per sample.

Reagent	Concentration	Volume [µl] per sample
Buffer-PCR	10x	2
$MgCl_2$	25mM	1,6
dNTPs	10mM	0,5
BSA	20mg/ml	0,25
PAN-Taq	5 U/ml	0,1
H_2O-PCR	-	9,55
3´Primer (8µM)	8µM	1
5´Primer (8µM)	8µM	1
DNA sample/ template	-	4

The standard master mix (MM) for each sample was multiplied by the number of primer pairs and the number of samples. Then, the MM was aliquoted into separate tubes corresponding to each primer pair, with the appropriate primers added to each tube. In this study, two different primer pairs were used to analyze gene expression changes in TREM2 KO mice. Depending on the primer pair, the thermal cycler adjusted the temperature and duration of each step within the PCR cycles (see Table 15).

Table 15. Protocol of PCR program.

Step	Temp °C	Time	Cycles
1	94°C	3 min	
2	94°C	15s	
3	65°C	15s	-0,5°C per cycle decrease
4	68°C	30 s	58°C /30 s
5			Repeat steps 2-4 for 10 cycles
6	94°C	15s	
7	60°C	15s	
8	72°C	30s	
9			Repeat steps 6-8 for 28 cycles
10	72°C	2 min	
11	4°C	hold	

2.2.6.2.4. Gel electrophoresis

For gel electrophoresis, a 2% agarose gel was prepared by dissolving 2 g of agarose in 100 ml of TAE buffer, heating the mixture in a microwave until fully dissolved. Then, 9 µl of GelRed was added to the solution to enable visualization of DNA bands. The gel solution was poured into a casting tray and left to solidify for approximately 20–30 minutes. Next, 15 µl of each sample, along with negative and positive controls and a gene ladder for size reference, were loaded into the wells. The gel was run at 130 V for about 60 minutes, allowing DNA fragments to migrate at speeds inversely proportional to their size. After electrophoresis, the DNA bands were visualized using the ChemiDoc XRS+ Gel Imaging System (Bio-Rad). Knockout efficiency was then assessed by analyzing the size of the amplified DNA fragments.

2.2.7. Staining

2.2.7.1. Immunofluorescence staining

Immunofluorescence (IF) staining was used to examine the cellular distribution of E-cadherin (a membrane protein involved in cell adhesion), Vimentin (a mesenchymal intermediate filament), and Phalloidin (a toxin that specifically binds to actin filaments). The process started with washing the slides or coverslips with PBS, followed by permeabilization of the cell membranes using a 0.5% Triton X-100 solution. To reduce non-specific antibody binding, samples were blocked with 1% BSA. Afterwards, cells were incubated with primary antibodies targeting E-cadherin, Vimentin, or Phalloidin for 1 to 2 hours. For primary antibodies without fluorescent tags, a FITC-labeled secondary antibody was applied for an additional hour to detect them. Nuclear staining was done using DAPI. Negative controls, where only secondary antibodies were applied, helped verify the specificity of staining. Imaging was performed with an Olympus FV3000 confocal laser scanning microscope.

2.2.7.1.1. Staining of tumor cell spheroids

Spheroids formed from 250 tumor cells were initially observed under the EVOS FL microscope at 4x and 10x magnifications and selected based on quality before staining. The best spheroids were then carefully transferred into chamber slide systems (Thermo Fisher) and incubated in DMEM supplemented with 10% FCS for 16 hours at 37°C to promote adhesion. After incubation, the medium was gently removed to avoid disturbing the spheroids, followed by a single wash with 500 µl PBS. Fixation was performed by adding 500 µl of cold (–20°C) 100% methanol for 10 minutes on ice. The methanol was then mostly removed, leaving about 200 µl to evaporate at room temperature. Once dry, the spheroids were washed twice with PBS and stained using anti-E-cadherin and anti-vimentin antibodies as specified. After staining, the chamber slides were dismantled according to the manufacturer's protocol. The spheroids were covered with coverslips mounted in fluorescent mounting medium (DAKO) and allowed to set in the dark at 4°C for 12 to 24 hours. Finally, images were captured using an Olympus FV3000 confocal microscope (FV31S-SW model).

Table 16. Tumor cell spheroids staining protocol.

Reagent	Dilution	Volume	Incubation
PBS wash		500µl	3 x 5 min
0,5% Triton-X in PBS		500µl	10 min
PBS wash		500µl	3 x 5 min
1% BSA (blocking buffer)		500µl	30 min
PBS wash		500µl	3 x 5 min

1°Antibody in blocking buffer	1:100	400µl	2 h
PBS wash		500µl	3 x 5 min
2°Antibody in blocking buffer	1:300	400µl	1h
PBS wash		500µl	3 x 5 min
DAPI -staining	1:2000	400µl	5 min
PBS wash		500µl	3 x 5 min

2.2.7.2. Staining of BMDM

Cell morphology analysis often involves visualizing the cytoskeleton under a microscope. In this context, phalloidin, a bicyclic peptide toxin derived from the death cap mushroom (Amanita phalloides), binds selectively to actin filaments (F-actin) found in most eukaryotic cells. When conjugated with fluorescent dyes like TRITC, phalloidin enables the visualization of these cellular structures using fluorescence microscopy. For the experiment, 2 x 10^5 cells suspended in DMEM supplemented with 10% FBS and 15% L929-conditioned medium were seeded onto glass coverslips pre-coated with extracellular matrix (diluted 1:4 in DMEM) and incubated overnight at 37°C in 24-well plates. After fixation with 500 µl of 4% paraformaldehyde (PFA) for 10 minutes at room temperature, the coverslips were washed three times with 500 µl PBS for 5 minutes each. Staining was then performed according to the protocol described in table 17. Finally, the coverslips were inverted and mounted onto slides using DAKO fluorescent mounting medium and allowed to dry at room temperature for at least 2 hours before being stored at 4°C.

Table 17. Phalloidin staining protocol.

Reagent	Dilution	Volume	Incubation
PBS wash		500µl	3 x 5 min
0,5% Triton-X in PBS		500µl	10 min
PBS wash		500µl	3 x 5 min
1% BSA (blocking buffer)		500µl	30 min
PBS wash		500µl	3 x 5 min
Phalloidin-TRITC in blocking buffer	1:600	400µl	2 h
PBS wash		500µl	3 x 5 min
DAPI -staining	1:2000	400µl	5 min
PBS wash		500µl	3 x 5 min

2.2.7.2.1. Quantification of BMDMs morphologies

Pictures of the BMDMs were taken using the Olympus FV3000 confocal microscope with the help of the ImageJ software the different morphologies in each condition were counted and th

2.2.7.2.2. Staining of MitoTracker Green

Mitochondrial content was assessed in collaboration with the Christian Wetzel group by staining cells with 200 nM MitoTracker® Green in OptiMEM for 30 min at 37°C, humidified air, and 5% CO_2. For imaging, the coverslips were washed three times with Ringer's solution containing glucose (300 osmole/kg) and placed in a measuring chamber on the microscope. The wavelength switcher allowed the excitation of MitoTracker® Green at 470/40 nm. The emitted light was filtered at 525/50 nm for MTG fluorescence, respectively.

2.2.7.2.3. Staining of Mitochondrial Membrane Potential MMP (JC-1) Cytosolic Ca2+ (Fura-2/AM) and Mitochondrial Ca2+ (Rhod-2/AM)

Mitochondrial membrane potential (MMP) and intracellular calcium (Ca^{2+}) homeostasis in WT and TREM2 KO BMDMs were evaluated using the ratiometric dye JC-1 and the calcium indicators Fura-2/AM and Rhod-2/AM, in collaboration with Christian Wetzel´s group. Two days prior to experimentation, BMDMs were seeded on glass coverslips coated with either Matrigel, Geltrex, or left uncoated. Cells were subsequently stimulated with ApoE 1µg/ml or LPS 10 ng/ml the following day for 24h. For MMP assessment, cells were incubated with JC-1 (300 nM) at 37 °C for 30 minutes. Fluorescence was recorded at 537/42 nm (green) and 620/60 nm (red) following excitation at 480/36 nm. For calcium imaging, cells were loaded with 2 µM Fura-2/AM and 2 µM Rhod-2/AM in OptiMEM, and incubated under the same conditions. Fura-2 fluorescence was recorded at 510 nm after excitation at 340 and 380 nm, while Rhod-2 fluorescence was measured at 576 nm upon 556 nm excitation.

2.2.7.3. Staining of brain tissues

In cooperation with the Institute of Pathology at the University Hospital Regensburg, collected brain tissues were processed routinely by placing them into cassettes, dehydrating, and embedding them in paraffin. Using a sliding microtome, brain sections were cut into 3 µm thick slices, which were then floated on a warm water bath and mounted onto glass slides by a technician. The slices were dried overnight at room temperature and then warmed for 30 minutes at 60°C the following day. To fix the tissue, slices were treated with a series of decreasing alcohol concentrations involving short changes between xylene, alcohol, and water

(detailed in the table below), before undergoing various staining protocols tailored to the targets of interest. After staining, samples were dehydrated again through an increasing alcohol concentration series with brief changes between water, alcohol, and xylene. Finally, the slides were coverslipped and scanned at the Institute of Pathology using the Pannoramic 250 slide scanner. Stained samples were visualized with the CaseViewer software.

2.2.7.3.1. Immunohistocheminal stainings

Morphological characteristics of BM were assessed using various immunohistochemical staining techniques. To visualize the MMPI patterns, brain sections were stained for the mesenchymal marker vimentin (Vim) and the epithelial marker cytokeratin-8 (Ck8). For analysis of the metastatic microenvironment (MME), brain slices were stained with allograft inflammatory factor 1 (Iba1) to identify microglia and macrophages; with glial fibrillary acidic protein (Gfap) to detect astrocytes; and with cluster of differentiation 3 (Cd3) or cluster of differentiation 8 (Cd8) to mark T cells. These staining procedures were carried out with technical support, following the protocols detailed in the subsequent tables:

Table 18. IHC staining protocols for Ck8, Iba1, Cd3 and Cd8.

Reagent	Incubation
1x Target Retrieval solution, citrate pH 6.1	30 min 330W, allow cooling
Deionized water	3x, short (10 sec)
Tris wash buffer (pH6)	10 min
100µl 3% peroxidase solution	10 min
Tris wash buffer (pH6)	10 min
100µl antibody diluent	20 min
100µl antibody in antibody diluent	overnight at RT
Tris wash buffer (pH6)	10 min
100 µl Rabbit IgG (H+L)-Biotin (1:250) in antibody diluent	1h RT
Tris wash buffer (pH6)	10 min
100 µl ExtrAvidin-Peroxidase (1:1000) in antibody diluent	1h RT
Tris wash buffer (pH6)	10 min
100 µl DAB solution (1:50)	10 min RT
Tris wash buffer (pH6)	10 min
Hematoxylin	20 sec
Water bath (37°C)	1 min
Deionized water	Short wash

Table 19. IHC staining protocols for Gfap.

Reagent	Incubation
1x Target Retrieval solution, citrate pH 6.1	30 min 330W, allow cooling
Deionized water	3x, incubate overnight at 4°C
Tris wash buffer (pH6)	10 min
100µl 3% peroxidase solution	10 min
Tris wash buffer (pH6)	10 min
100µl antibody diluent	20 min
100µl antibody in antibody diluent	1h at RT
Tris wash buffer (pH6)	10 min
100 µl biotinylated secondary antibody (Reagent AB2)	15 min RT
Tris wash buffer (pH6)	10 min
100 µl streptavidin alkaline phosphatase (Reagent AP)	15 min RT
Tris wash buffer (pH6)	10 min
100 µl chromogen solution (Chromogens Red)1+2+3 (1:25) in AP substrate buffer)	1.5 min RT
Tris wash buffer (pH6)	10 min
Hematoxylin	20 sec
Water bath (37°C)	1 min
Deionized water	Short wash

2.2.8. Microscopy

2.2.8.1. Bright field microscopy

Cell morphology of tumor cells and tumor spheroids was examined using bright-field microscopy. Imaging was performed with an Olympus FV3000 confocal laser scanning microscope and analyzed using FV31S-SW software. Images were captured using 20x (without oil), 40x, and 60x (oil immersion) objectives. Additionally, the EVOS FL microscope was employed to observe spheroid formation and assess cell confluence at 4x and 10x magnifications.

2.2.8.2. Confocal microscopy

Immunofluorescence staining of tumor cells and spheroids was visualized using an Olympus FV3000 confocal laser scanning microscope and analyzed with FV31S-SW image processing software. Images were captured with DAPI (405 nm), FITC (488 nm), and TRITC (532 nm) lasers, using 20x (oil-free), 40x, and 60x (oil immersion) objectives. To prevent fluorescence, overlap between channels, sequential image acquisition was applied.

2.2.8.3. Fluorescent live cell imaging microscopy

Live cell imaging experiments were conducted in collaboration with the Christian Wetzel group using an inverted Zeiss Axio Observer Z.1 microscope equipped with a Fluor 40/1.3 objective lens (Zeiss, Oberkochen, Germany). All recordings were taken at a magnification of 40x with oil and detected using an AxioCam MRm CCD camera (Zeiss, Oberkochen, Germany). Illumination control and image acquisition were performed using a Lambda DG-4 high-speed wavelength switcher (Sutter Instruments, Novato, USA) and the ZEN 2012 imaging software. Analysis of the measurements in the regions of interest, manually drawn over selected cells in the visual field, was performed using ImageJ. Macros were used for background subtraction and, where applicable, to calculate ratios in order to ensure the repeatability of the analysis.

2.2.8.4. Transmission electron microscopy

Electron microscopy (EM) was conducted with the support of Heiko Siegmund from the pathology department. Cells were resuspended in Cytoblock Reagent (Epredia, Dreieich, Germany) and then surrounded by 4% low-melting agarose. For the embedding process (post-fixation with osmium tetroxide, dehydration, infiltration with EPON), the LYNX microscopy tissue processor (Reichert-Jung, Wetzlar, Germany) was used. Semi-thin-sections (0.75 µm), for the selection of relevant areas and ultra-thin sections (80nm), were cut by using the Reichert

Ultracut S Microtome (Leica-Reichert, Wetzlar, Germany). First, the grids were contrasted with aqueous 2%-uranyl-acetate, followed by 2%-lead-citrate solution for 10 minutes, each. Electron-microscopic analysis was performed using the LEO 912AB transmission electron microscope (Zeiss, Oberkochen, Germany). High-resolution electron microscopy images (5,000x for whole cells, 20,000x for mitochondria) were analyzed using ImageJ. Images were converted to 8-bit grayscale, and the scale was calibrated using the embedded scale bar. Whole-cell and mitochondrial outlines were manually traced using the Freehand Selection Tool, and mitochondrial length and width were measured with the Straight Line Tool. ROIs were added to the ROI Manager and measured via Analyze > Measure. For each group, 5–10 cells were analyzed, including all mitochondria per cell. Quantified parameters included mitochondrial number per cell and mean area.

2.2.8.5. Magnetic resonance Imaging (MRI)

For MRI analysis, animals were transferred to the Preclinical Imaging Platform Erlangen (PIPE, Erlangen, Germany) three days after tumor cell implantation. *In vivo* MRI imaging of the animals was performed in collaboration with Tobias Bäuerle´s group on days 14, 20 and 22 with a preclinical 7T MRI scanner (BioSpec, Bruker BioSpin, Ettlingen, Germany) equipped with a mouse brain surface coil: RF SUC 300 1H M.BR. QSN RO AD (Bruker, Ettlingen, Germany) in a combination with the transmission coil RF RES 300 1H 112/086 QSN TO AD.

During *in vivo* imaging, the animals were anesthetized by inhalation of the mixture of oxygen (0.5 l/min) and isoflurane (1.5 vol %) throughout the entire imaging procedure. Respiratory rate was continuously monitored using breath sensors and maintained at a constant level. To stabilize body temperature, a heating circulator bath from Thermo Fisher Scientific (Waltham,USA) was used.

The imaging protocol included pre- and postcontrast T1-weighted spin echo and T2 TurboRARE sequences. Following imaging sequences were used: coronal T2-weighted RARE (TR 2200 ms, TE 36ms, matrix 361 · 298, resolution 0.050 · 0.050 mm, 4 averages, scan time 5:25 min) and axial T1-weigted RARE before and after the administration of the contrast agent (TR 750 ms, TE 6,50 ms, matrix 265 · 281, resolution 0.060 · 0.060 mm, 3 averages, scan time 5:15 min). During acquiring a of a Dynamic Contrast-Enhanced sequence (DCE_FLASH), the mice received an intravenous bolus injection of a low molecular weight gadolinium chelate agent (0.15 mmol/kg Gadobutrol, Gadovist, Bayer Vital GmbH, Leverkusen, Germany) over a time period of 10 s via a tail vein catheter.

2.2.9. Statistical analysis

Unless otherwise stated, data was analyzed using the unpaired two-sided student's t-test (one variable, two groups) or one-way analysis of variance (ANOVA) (one variable, three or more groups), depending on the experimental design. ANOVA analyses were followed by suitable post-hoc tests, including Dunnett's test (comparing each mean to a control mean), Tukey's test (comparing all means against each other), or Sidak's test (comparing selected pairs of means). Kaplan-Meier survival curves were analyzed using the log-rank test. For contingency tables, chi-square tests were applied. Data are presented as mean ± standard deviation (SD), unless otherwise indicated. Statistical significance was determined at p-values below 0.05 (*$P < 0.05$; **$P < 0.01$; ***$P < 0.001$; ****$P < 0.0001$). Statistics were performed and the data was plotted using the GraphPad Prism 9 and 10 software.

2.2.10. Artificial Intelligence Tools

In the preparation of the thesis, artificial intelligence tools (primarily Grok 4 and ChatGPT 5) were used to assist with paraphrasing, grammar correction, language refinement, and improving the overall clarity and flow of the scientific writing. All AI-generated suggestions were carefully reviewed, critically evaluated, and substantially revised by me. I take full responsibility for the accuracy and final content of the thesis.

3. Results

This study is divided into two main parts, each addressing a distinct but interconnected aspect of brain metastasis biology. The first part underscores the existence of distinct HGPs at the MMPI and highlights their potential prognostic relevance. The second part focuses on elucidating the role of the immune receptor TREM2 in shaping the macrophage phenotype, modulating macrophage-tumor cell interactions, and its impact on brain metastatic colonization *in vivo*.

3.1. Murine breast and colon cancer cell lines

Breast and colorectal cancers represent two of the most common primary tumor types with a high propensity for brain metastasis. Based on this clinical relevance, the initial phase of this study focused on selecting suitable murine models of these cancers.

3.1.1. Characterization of epithelial/mesenchymal features in murine breast cancer and colon cancer cell line models

Cancer cell models were selected based on their known or suspected capacity to metastasize to the brain. Specifically, the breast cancer cell lines E0771-LG and 99LN, and the colorectal cancer cell lines CMT93Var and KPN, were chosen. E0771-LG is derived from a triple-negative murine breast cancer line (Kitamura et al. 2019), whereas 99LN represents a luminal B murine breast cancer model (Wu et al. 2021). CMT93Var is a murine colorectal cancer cell line (Franks and Hemmings 1978), and KPN originates from a murine small-intestinal tumor organoid (Jackstadt et al. 2019). These selected cell lines cell lines were subjected to detailed morphological and gene expression analyses to investigate the phenotypic heterogeneity and to characterize the biological features potentially contributing to their colonization behaviors metastatic potential *in vivo*. Morphologically under 2D conditions, all three cell lines were adherent but exhibited distinct morphology. While 99LN cells grew as rather wide tubular structures, whereas KPN and CMT93Var formed compact, round clusters structures. In contrast, E0771LG cells showed looser structures with fewer attachment points (Figure 10A). To further assess epithelial and mesenchymal traits using established EMT-associated markers, a critical process to cancer invasion and metastasis (Ye and Weinberg 2015), I performed immunofluorescence staining for E-cadherin (Ecad) and Vimentin (Vim), followed by confocal microscopy. Consistent with an epithelial phenotype, 99LN cells showed strong Ecad (green) expression. In comparison, KPN and CMT93Var displayed staining patterns indicative of a

partial epithelial-to-mesenchymal transition (EMT) phenotype. E0771-LG cells showed predominantly mesenchymal traits, characterized by strong Vim (red) expression (Figure 10B).

To better mimic the tumor microenvironment, morphological characterization was extended to three-dimensional (3D) culture conditions. Cells were grown as spheroids using the Hanging Drop method and analyzed by Ecad and Vim immunofluorescence staining. Similar to the 2D results, spheroids from the 99LN, KPN, and CMT93Var cell lines showed strong Ecad expression (green), indicating preserved epithelial traits. In contrast, E0771-LG spheroids displayed high cytoplasmic Vim expression (red), reflecting the mesenchymal characteristics (Figure 10C). To further evaluate epithelial/mesenchymal traits of the cell lines, we assessed the expression of canonical epithelial (*Ecad*, Yes-associated protein 1 (*Yap1)*) and mesenchymal markers (*Vim*, Zinc finger E-box binding homeobox 1 (*Zeb1*)) by qPCR. Interestingly, despite their epithelial morphology, the CMT93Var and KPN cell lines exhibited high expression of both epithelial and mesenchymal markers, consistent with a hybrid epithelial/mesenchymal (E/M) phenotype. Notably, KPN cells expressed lower levels of the EMT-promoting factor *Zeb1* compared to CMT93Var, suggesting subtle differences in EMT status that may underlie their distinct infiltration behaviors (see Results 3.2.1.). This hybrid E/M phenotype is increasingly recognized as a hallmark of partial EMT, which confers migratory and invasive plasticity (Saitoh 2018). The 99LN cell line, consistent with its staining profile, maintained high epithelial and low-to-moderate mesenchymal gene expression, indicating a more epithelial phenotype. Conversely, E0771-LG showed the lowest expression of epithelial markers, along with high expression of the mesenchymal markers, supporting its identity as a breast cancer cell line with fully mesenchymal-like traits (Figure 10D).

Based on these combined molecular and morphological analyses, the colorectal cancer-derived lines CMT93Var and KPN were categorized as partial EMT phenotypes. Among the breast cancer-derived lines, 99LN retained a stable epithelial phenotype, while E0771-LG, with its high mesenchymal signature (Figure 10E).

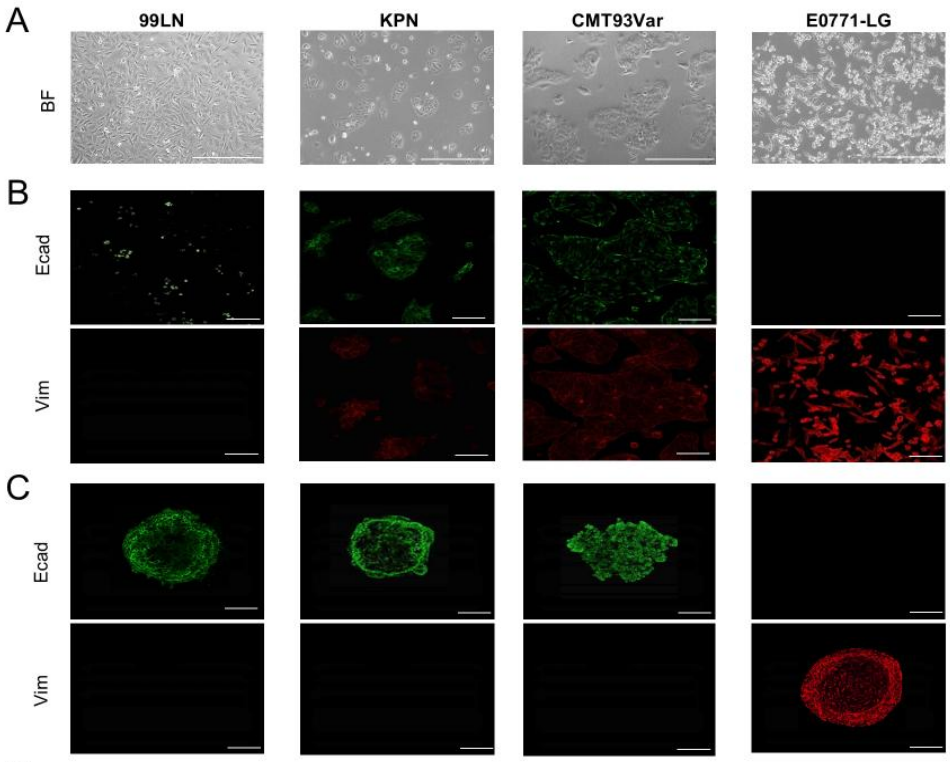

E

Cell line	Marker Expression				EMT Phenotype	Epithelilal barrier formation	Infiltration pattern
	ECAD	YAP1	VIM	ZEB1			
99LN	+	+	-	+	Epithelial	+	Displacing
KPN	+	+	+	-	Partial EMT	+	Displacing
CMT93var	+	+	+	+	Partial EMT	+	Epithelial
E0771-LG	-	-	+	+	Mesenchymal	-	Diffuse

Figure 10. Characterization of epithelial/mesenchymal features in murine breast and colon cancer.

(A) Representative pictures of murine breast and colon cancer cell lines were taken with a bright field (BF) microscope. Scale bars represent 400 µm. (B) Confocal microscopy images after Ecad-conjugated FITC (green) and Vim-conjugated TRITC (red) staining of 2D cell culture models of breast and colon cancer cell lines. (C) Representative confocal microscopy images of spheroids from murine breast and colon cancer cells after Ecad-conjugated FITC (green) and Vim-conjugated TRITC (red) staining. All scale bars represent 50 µm. (D) qRT-PCR analysis of the epithelial markers *Ecad* and *Yap1*, and the mesenchymal markers *Vim* and *Zeb1*. *Gapdh*

and *Pgk1* were used as housekeeping (HK) genes. P-value was calculated with one-way ANOVA followed by Tukey's multiple comparisons tests (*P<0.05, **P<0.01, ***P<0.001, ****P< 0.0001). (E) Summary table of cell lines indicating the relationship between gene expression of certain markers and EMT phenotype.

3.2. Experimental models of brain metastasis

A central aim of this study was to investigate the role of TREM2 signaling in breast and colorectal cancer brain metastasis models that exhibit distinct HGPs. To this end, it was first necessary to characterize the colonization behavior of the selected cancer cell lines *in vivo*. Our group has established a brain colonization model in which tumor cells are stereotactically implanted into the brain of syngeneic mice. This model enables the analysis of both MMPI patterns and mechanisms of the MME within an immunocompetent host, thus providing a physiologically relevant context (Alves de Lima et al. accepted).

3.2.1. Characterization of the HGP at the MMPI in mouse models of brain metastatic colonization

To characterize the colonization behavior and growth patterns of the selected breast cancer (BC) and colon cancer (CC) cell lines (Figure 11) *in vivo*, we stereotactically injected 10^3 cells from each of the murine cancer cell lines, 99LN, KPN, CMT93Var, and E0771-LG, into the right hemisphere of 10–12-week-old immunocompetent syngeneic C57BL/6 mice, as described (Alves de Lima et al. accepted). Among these, the murine colorectal cancer cell line CMT93Var and the breast cancer cell line E0771-LG were previously validated by our group as syngeneic BM models, whereas the murine colorectal cancer line KPN and the breast cancer line 99LN, which were generously provided by Prof. Elisabeth Naschberger and Prof. Lisa Sevenich within the framework of the TRR305 consortium, were established by myself.

In addition to behavioral and neurological assessments (Hanging Wire test), the development of BM was confirmed by histological evaluation and qRT-PCR analysis. The HGPs were assessed on formalin-fixed paraffin-embedded (FFPE) brain sections to define the structural and spatial characteristics of metastatic growth.

Comparative IHC analysis was performed using the epithelial marker cytokeratin 8 (Ck8) and the mesenchymal marker Vim, and revealed distinct HGPs at the MMPI between the injected model cell lines. Mice injected with the breast 99LN and colon KPN cancer cell lines developed brain metastases with well-demarcated boarders and no apparent infiltration into the surrounding parenchyma. Instead, the tumors displaced adjacent brain tissue via expansive growth, resulting in a compressed but intact neighboring architecture (Figure 11A). This growth

modality aligns with what has been previously described as a non-infiltrative or “displacing” HGP. The molecular analysis revealed a significantly higher *Ecad* expression in mice injected with either 99LN or KPN cells compared to the ECM-injected control brains. In contrast, the expression of the mesenchymal marker *Vim* was low and comparable among the control mice and mice with non-infiltrative metastases (Figure 11B).

BM from mice injected with either the CMT93Var or the E0771-LG cell lines exhibited an infiltrative HGP, but markedly different infiltration profiles. While BM derived from the CMT93Var line showed a glandular infiltration of tumor cells into the adjacent brain parenchyma, E0771-LG-derived BM demonstrated a diffuse, poorly circumscribed growth pattern (Fig. 11A), at the mRNA level, CMT93Var BM showed a high *Ck8*, *Ecad* and *Vim* expression, features consistent with partial EMT phenotype and epithelial-infiltrative MMPI pattern. On the other hand, E0771-LG BM displayed a high *Ck8* and *Vim* expression, and low *Ecad* expression, indicative of a more mesenchymal trait, but still retaining their epithelial character (breast carcinoma). These tumors infiltrated the surrounding brain parenchyma in a dispersed and irregular manner, consistent with a "diffuse infiltrative" HGP (Figure 11A and B).

Overall, these findings highlight significant differences in the histological architecture and growth patterns among the four selected murine breast (BCBM) and colorectal cancer BM (CCBM) models. While 99LN and KPN cells predominantly formed non-infiltrative, displacing metastases, the CMT93Var and E0771-LG cells exhibited progressively more infiltrative phenotypes, ranging from epithelial infiltration to diffuse infiltration.

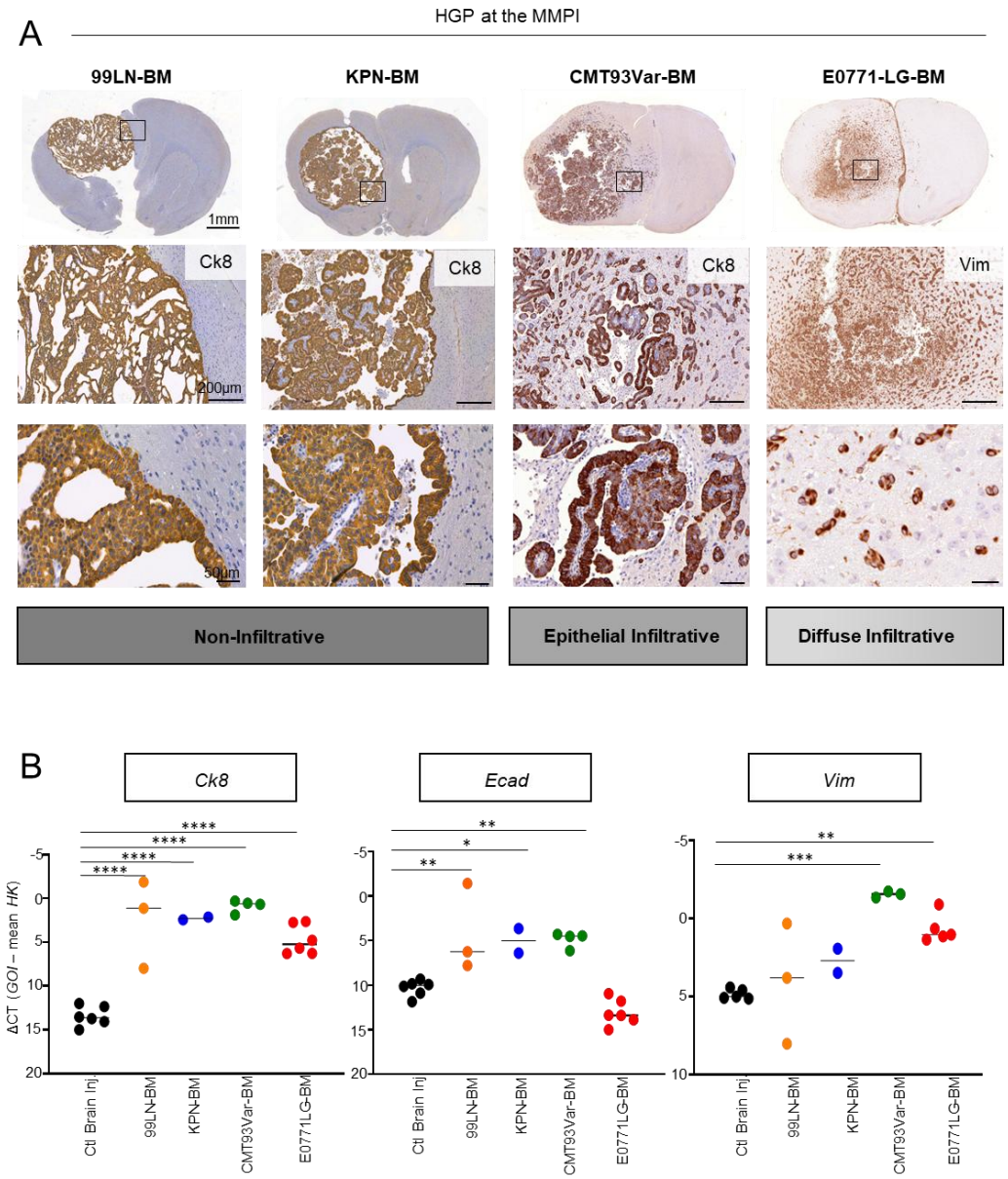

Figure 11. The HGP at the MMPI of BCBM and CCBM mouse models.

(A) IHC staining of Vim and Ck8 in tissue sections from BM of C57BL/6 mice injected with the corresponding cell line. Representative images of coronal brain sections and their MMPI are shown. (B) qRT-PCR analysis of the metastatic epithelial markers *Ck8*, *Ecad*, and the mesenchymal marker *Vim* in ECM-injected control (Ctl) brains and BM from 99LN, KPN, CMT93Var and E0771LG. *Gapdh* and *Pgk1* were used as housekeeping genes. P-value was calculated with one-way ANOVA followed by Tukey's multiple comparisons tests (*P<0.05, **P<0.01, ***P<0.001, ****P< 0.0001).

3.2.2. Impact of the HGP on the neurological cause of death

To further examine growth dynamics and pathophysiological features associated with the HGP of BM, we conducted high-resolution magnetic resonance imaging (MRI) at the preclinical imaging platform Erlangen (PIPE) in collaboration with Prof. Tobias Bäuerle (Department of Radiology, University Hospital Erlangen).

We employed experimental models of BM with distinct HGPs. On the one hand, we used the non-infiltrative TUBO model and, on the other hand, the diffuse infiltrative E0771-LG model. Tumor cells were injected into the right hemisphere of either BALB/C mice or C57BL/6, respectively. MRI scans were performed at different time points during metastatic progression (day 14, 20 and 22 after OP) (Figure 12A).

Notably, although both models reached humane endpoints by day 22, the underlying causes were distinct. In mice bearing TUBO tumors, disease progression was driven primarily by expansive tumor growth that led to significant compression of the adjacent healthy brain parenchyma. In contrast, mice injected with E0771-LG cells exhibited intra-organ dissemination by day 22, including the emergence of a secondary lesion in the contralateral (left) hemisphere (Figure 12B). This phenomenon was also clearly represented via the 3D reconstruction models of both the TUBO and E0771LG tumors (Figure 12B). This highlights a key pathological difference: whereas the non-infiltrative TUBO model causes localized mass effect, the diffuse infiltrative E0771-LG model progresses through broad infiltration and secondary dissemination, leading to the formation of secondary metastases (Komljenovic et al. under revision).

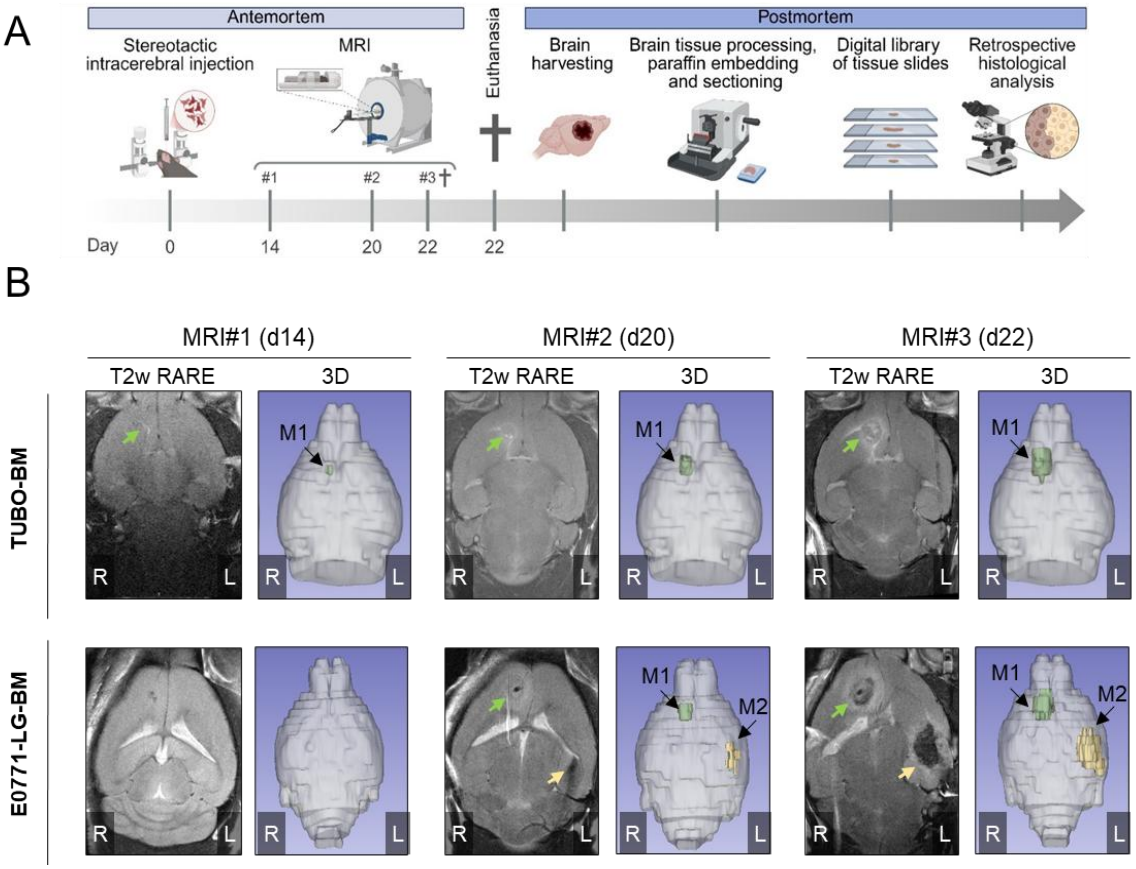

Figure 12. Impact of the HGP on the neurological cause of death.

(A) Schematic overview of the experimental workflow. The diagram depicts the MRI monitoring performed during the antemortem phase following stereotactic intracerebral injection, as well as the postmortem workflow for brain tissue collection, processing, and histological analysis. Created with BioRender.com. (B) Representative coronal T2-weighted MR images and 3D reconstruction pictures at day 14, 20 and 22 of the non-infiltrative model TUBO and the diffuse infiltrative model E0771LG-induced BM. Arrows denote metastatic lesions (M). Primary (M1) and subsequent lesions (M2) are shown in green and yellow, respectively, in the 3D reconstructions. Adapted from (Komljenovic et al. under revision).

3.2.3. Evolution of the HGP in early vs. late colonization

Due to the clinical impact of the HGPs on influencing the cause of neurological death, an early detection of the HGP would be desirable in order to guide therapeutic managements of these patients at early stages. Therefore, we next asked whether the HGP remains stable during different stages of metastatic colonization. To this end, IHC analyses were performed at different time points during metastatic colonization in the non-infiltrative TUBO and the diffuse infiltrative E0771-LG BM models. In the TUBO model, Ecad staining confirmed a well-demarcated, epithelial non-infiltrative HGP at both early (day 8 after OP) and late (day 22 after OP) stages. Conversely, in the E0771-LG model, Vim expression at the MMPI was evident at

both time points, consistent with a stable diffuse infiltrative growth pattern. These findings suggest that the HGP is an intrinsic and temporally conserved property of the tumor cell line, with no observable switch from non-infiltrative to infiltrative or vice versa during disease progression (Figure 13B and C).

In conclusion, our data demonstrate that the HGP at the MMPI is stable and conserved between early and late stages of colonization in both non-infiltrative and infiltrative tumor models (Komljenovic et al. under revision).

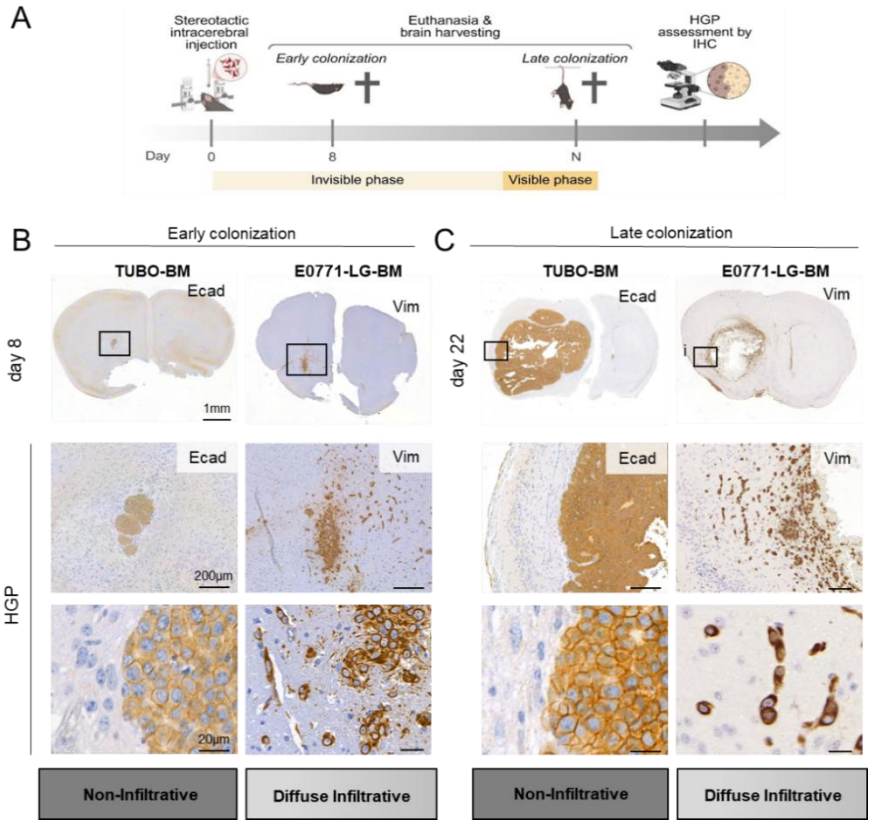

Figure 13. Evolution of the HGP in early vs. late colonization.

(A) Schematic overview of the experimental workflow. Image created with Biorender.com. (B) IHC staining of Ecad and Vim in tissue sections of the non-infiltrative model TUBO and the diffuse infiltrative model E0771LG-induced BM after injection of 10^3 cells at day 8 (early colonization) (C) and at the end point day 22 (late colonization). Scale bar represents 200µm and 20µm, respectively. Adapted from (Komljenovic et al. under revision).

3.2.4. Impact of the HGP on immune phenotypes

The brain MME represents a highly specialized and immunologically distinct niche, composed of resident glial cells, primarily astrocytes and microglia, as well as infiltrating peripheral immune cells, including macrophages and T lymphocytes (Schreurs et al. 2025). These immune cell populations are known to influence various stages of metastatic progression, from initial colonization to the establishment of overt lesions (Huang et al. 2021). Importantly, we hypothesize that the architecture and cellular behavior within the MME are thought to be shaped by the HGP at the MMPI, which governs the physical interaction between tumor cells and the surrounding brain tissue.

To elucidate the relationship between HGP of BM and immune cell infiltration, we conducted a comprehensive immunological characterization in our syngeneic murine models. Specifically, we assessed the distribution and activation status of key immune cell types, microglia/macrophages ($Iba1^+$), astrocytes ($Gfap^+$), and T lymphocytes ($Cd3^+$), by combining immunohistochemical analysis with qRT-PCR of metastatic brain tissues, as proposed by (Galon and Bruni 2019). This integrative approach allowed us to dissect both spatial and transcriptional dynamics of immune infiltration in relation to distinct HGPs and provided valuable insight into the immunological heterogeneity of brain metastases arising from different tumor types and growth behaviors.

3.2.4.1. Characterization of T cells in the metastatic brain

T cells are a critical part of the immune landscape in the BM-MME. Cytotoxic T cells ($CD8^+$) play a tumor-suppressing role and are linked to improved survival rates, while regulatory T cells ($CD4^+$), which suppress immune responses, are correlated with worse prognosis and shorter survival. Notably, T cells are typically absent from healthy brain tissue and only infiltrate the CNS during pathological states, such as the metastatic colonization (Schreurs et al. 2025).

To assess T cell presence within the metastatic lesions, the expression of the Cd3 marker was analyzed *in vivo*, focusing on the metastatic core, MMPI, and adjacent brain tissue. Strikingly, both the 99LN and KPN models showed an almost complete absence of $Cd3^+$ T cells in the MMPI and tumor core, with only a few cells detectable. This suggests a "cold" immune phenotype (Bruni et al. 2020). In contrast, brain metastases formed by CMT93Var and E0771-LG cells displayed notably higher $Cd3^+$ T cell infiltration in both central and peripheral tumor regions, indicating a more reactive phenotype (Figure 14A). These findings were further

validated by qRT-PCR, which demonstrated significantly higher *Cd3* expression in the CMT93Var and E0771-LG models compared to 99LN and KPN, when statistically compared to the ECM-injected control brains (Figure 14B). To further substantiate our findings on T cell infiltration, we extended our immunohistochemical analyses by staining for Cd8, a marker specific for cytotoxic effector T cells. As previously reported by (Galon and Bruni 2019), immune-suppressed tumors typically characterized by poor, but not absent, $CD8^+$ T cell infiltration and high expression of the inhibitory mediators TGF-β and IL-10. In contrast, immune-cold tumors show minimal to no cytotoxic T cell presence. Consistent with our Cd3 staining results, the infiltrative models, E0771-LG and CMT93Var, demonstrated intermediate levels of $CD8^+$ T cell infiltration within the metastatic lesions, with CMT93Var showing comparatively higher $CD8^+$ T cell density. Both models also showed a significantly elevated expression of *Tgf-β*, an immunosuppressive cytokine, indicating an immune-infiltrated yet functionally restrained tumor microenvironment typical of a "T cell–inflamed" or altered immunosuppressed phenotype (Figure 14A and B).

By contrast, the non-infiltrative models, 99LN and KPN, exhibited markedly reduced $CD8^+$ T cell presence, along with lower *Tgf-β* expression levels, consistent with an "immune-cold" phenotype characterized by limited immune cell recruitment and minimal immune activation. These findings further support the hypothesis that the HGP at the MMPI not only influences metastatic infiltration behavior but also plays a critical role in shaping the immune landscape of the brain metastatic microenvironment.

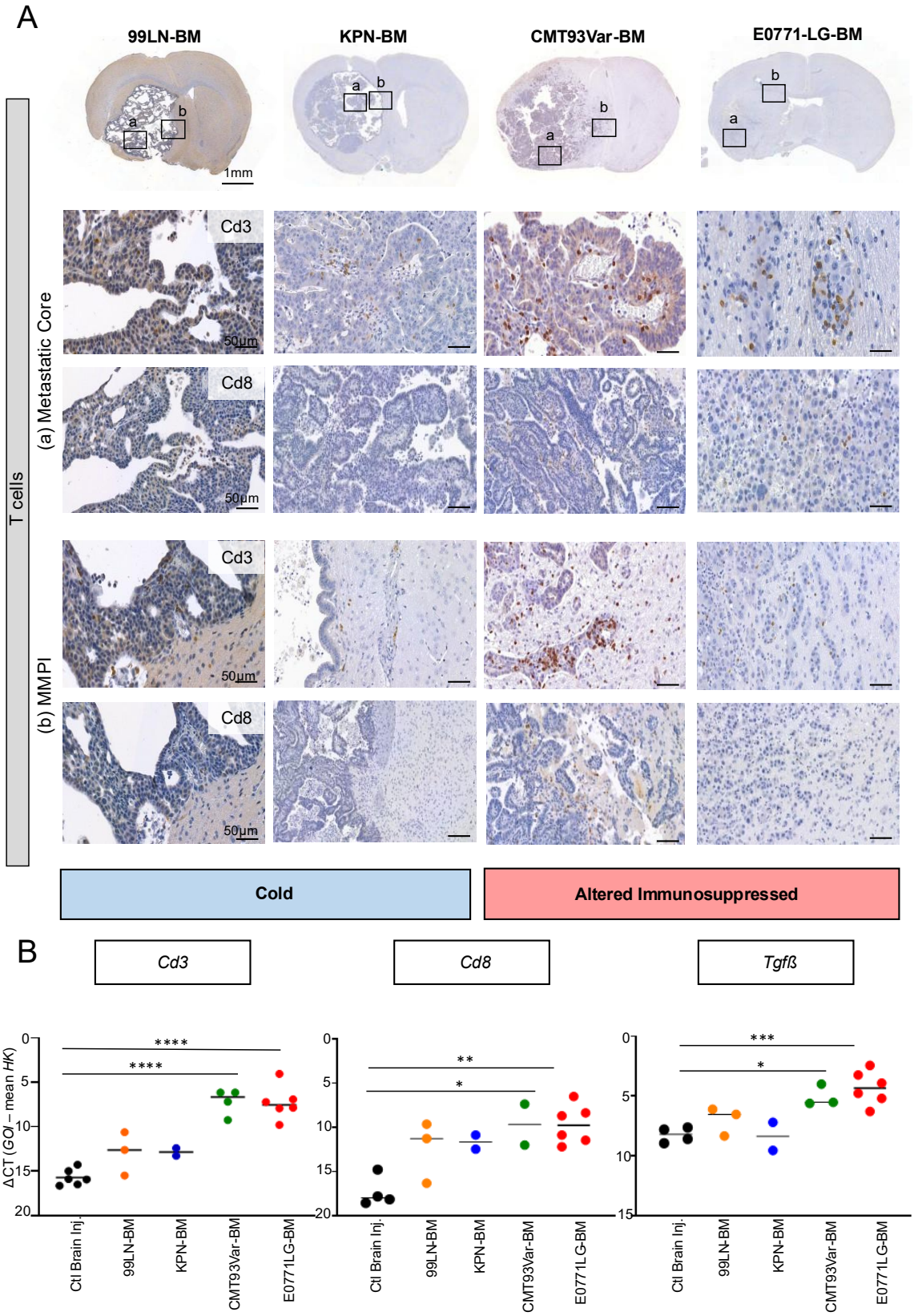

Figure 14. Characterization of CD3+ and CD8+ T cell population in the metastatic brain.

(A) IHC images of brain metastatic tissue after staining of T cell population with Cd3 and Cd8 marker of mice injected with BCBM and CCBM models 99LN, KPN, CMT93Var and E0771-LG. (B) qRT-PCR analysis of *Cd3*, *Cd8* and *Tgf-β* gene expression level in ECM-injected

controls (Ctl) and BM from 99LN, KPN, CMT93Var and E0771-LG. *Gapdh* and *Pgk1* were used as housekeeping (HK) genes. P-value was calculated with one-way ANOVA followed by Tukey's multiple comparisons tests (*P<0.05, **P<0.01, ***P<0.001, ****P< 0.0001).

3.2.4.2. Characterization of astrocytes in the metastatic brain

Astrocytes, characterized by star-shaped morphology under physiological conditions, are the most abundant glial cells of the CNS. In response to tumor cells, astrocytes become activated, infiltrating surrounding tissues and capable of triggering metastasis (Xing et al. 2013). In their activated state, they can be quantified in IHC stainings for Gfap. A strong Gfap staining, described as a marker for brain injury, was observed in all four models, albeit with some differences. In the non-infiltrative 99LN- and KPN models, $Gfap^+$ astrocytes displayed strong activation within the tumor-bearing hemisphere but remained largely confined to the peritumoral region. These astrocytes formed a characteristic glial ring at the MMPI, effectively delineating the tumor boundary and creating a physical barrier between tumor cells and adjacent brain parenchyma (Figure 15A). In contrast, in the infiltrative CMT93Var and E0771-LG models, astrocytes were not restricted to the MMPI but also boarded the metastatic cluster reflecting a more reactive phenotype. Gene expression analysis confirmed these histological findings, with a not significant lower *Gfap* expression in non-infiltrative models compared to the ECM-injected control brains and significantly higher expression in CMT93Var and E0771-LG metastatic tissues (Figure 15B).

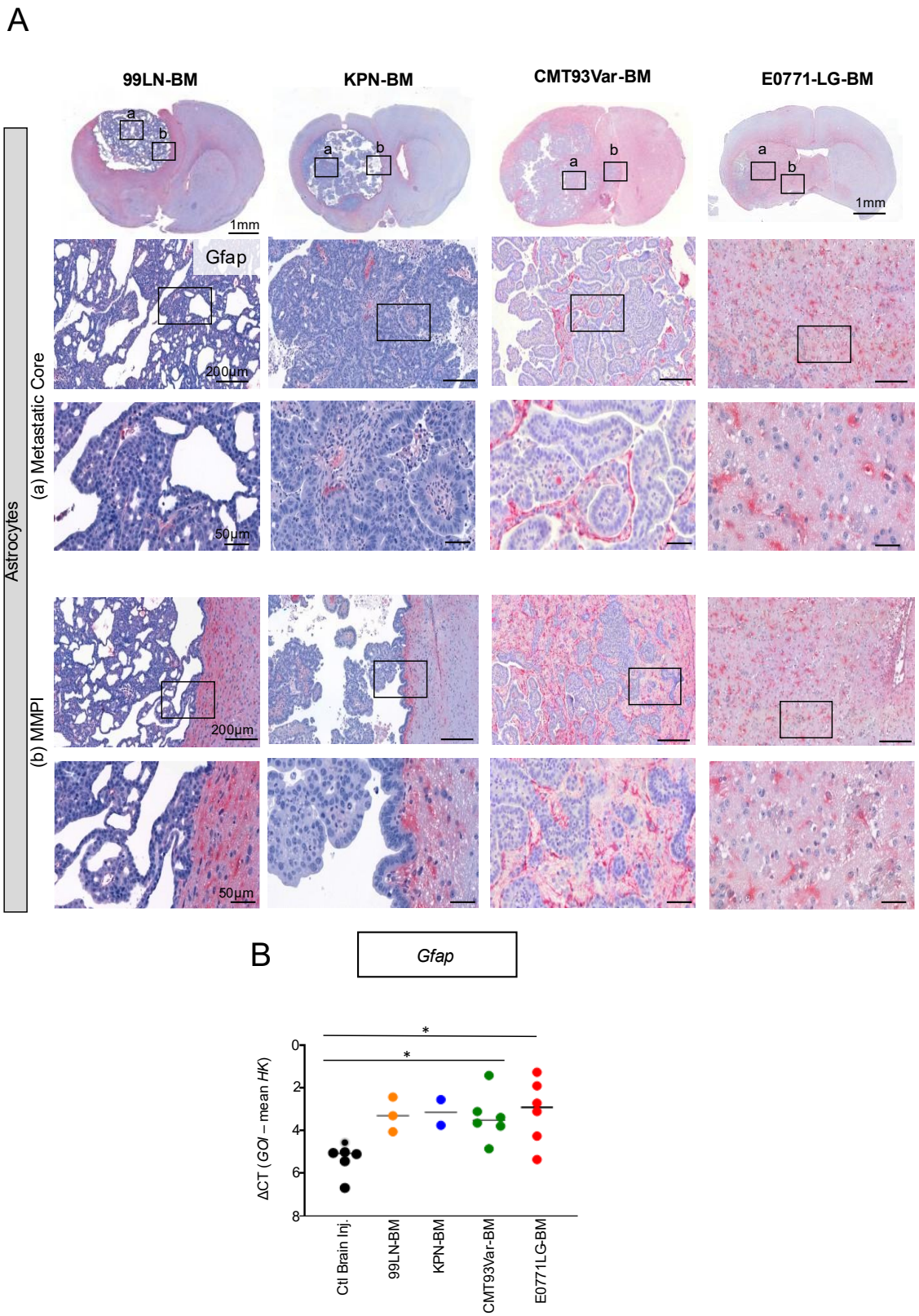

Figure 15. Characterization of astrocyte population in the metastatic brain.

(A) IHC images of brain metastatic tissue after staining of astrocyte population with Gfap marker of mice injected with BCBM and CCBM models 99LN, KPN, CMT93Var and E0771-LG. (B) qRT-PCR analysis of *Gfap* gene expression level in ECM-injected controls (Ctl) and

BM from 99LN, KPN, CMT93Var and E0771-LG. *Gapdh* and *Pgk1* were used as housekeeping (HK) genes. P-value was calculated with one-way ANOVA followed by Tukey's multiple comparisons tests (*P<0.05, **P<0.01, ***P<0.001, ****P< 0.0001).

3.2.4.3. Characterization of MG/BMDM in the metastatic brain

MG and BMDMs represent key immune components within the brain MME. While MG serve as the brain's intrinsic immune surveillance system and are constantly present in the CNS, BMDMs are recruited from the periphery only under pathological conditions, such as infection or tissue damage, where they cross the BBB to enter the brain parenchyma (Bowman et al. 2016). Both cell types play complex roles in tumor progression, capable of promoting or suppressing inflammation depending on their activation state. Their influence on brain tumor dynamics is increasingly recognized, particularly in the context of metastasis, where they contribute to remodeling the local MME (Klemm et al. 2020). To explore the activation of MG and BMDMs during BM, we assessed these cells in multiple syngeneic mouse models using Iba1 as a pan-macrophage marker.

Our analysis revealed that Iba1$^+$ cells, indicative of activated MG/BMDMs, were consistently present at the MMPI and within the metastatic core. Their numbers decreased progressively with distance from the metastatic lesion and were nearly absent in the contralateral (non-injected) hemisphere. Model-specific differences in microglia/macrophage distribution were also evident. In mice injected with the non-infiltrative 99LN and KPN cell lines, Iba1$^+$ cells were primarily localized to the MMPI, with minimal infiltration into the metastatic core. In contrast, the infiltrative models, CMT93Var and E0771-LG, showed a more diffuse presence of Iba1$^+$ cells throughout the entire metastatic lesion. Among these, the E0771-LG model exhibited the most pronounced *Iba1* activation, at mRNA level, as confirmed by qRT-PCR data (Figure 16A and B). Specifically, *Iba1* expression was significantly higher in E0771-LG tumors compared to the ECM-injected control brains and not significant to the limited expression observed in 99LN and KPN models.

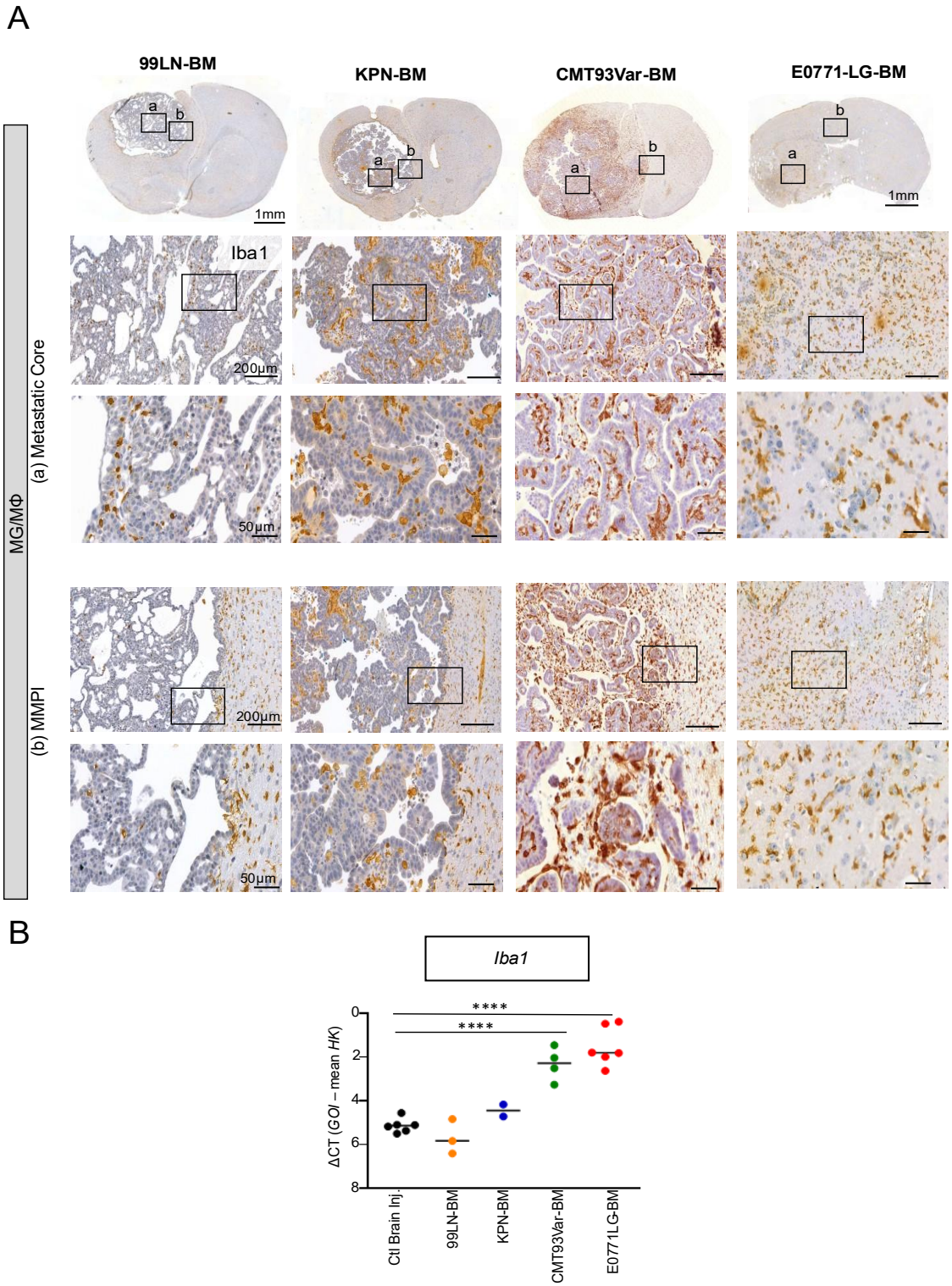

Figure 16. Characterization of MG/BMDM populations in the metastatic brain.

(A) IHC images of brain metastatic tissue after staining of MG/BMDM population with Iba1 marker of mice injected with BCBM and CCBM models 99LN, KPN, CMT93Var and E0771-LG. (B) qRT-PCR analysis of *Iba1* gene expression level in ECM-injected controls (Ctl) and BM from 99LN, KPN, CMT93Var and E0771-LG. *Gapdh* and *Pgk1* were used as housekeeping

(HK) genes. P-value was calculated with one-way ANOVA followed by Tukey's multiple comparisons tests (*P<0.05, **P<0.01, ***P<0.001, ****P< 0.0001).

3.2.4.4. TREM2 expression on MG/BMDM

Given the important role of the MG/BMDM populations during brain metastatic colonization, our previous experiments identified, an organ- and entity-independent myeloid gene signature shared across liver and CNS metastasis models (unpublished data). Interestingly, this signature closely aligns with the recently described and highly conserved "danger- containing" Trem2^{+} macrophage population, identified across multiple states of tissue stress and damage, including Alzheimer's disease, arthritis, atherosclerosis, and adipose tissue inflammation (Culemann et al. 2019). These Trem2^{+} macrophages display a unique immunoregulatory profile whose functional significance is not yet fully understood (Ulrich et al. 2017). Notably, they appear capable of containing tissue damage by physically segregating injured regions and inducing localized immune suppression, a mechanism referred to as "shielding" (Collison 2019).

In several tissue-damage models (joint, muscle), our collaboration partners, the group of Gerhard Krönke, identified a 20-gene signature characteristic of macrophages engaged in this shielding response (Culemann et al. 2019). In parallel, our group generated a 252-gene colonization signature by identifying shared drivers of metastatic colonization in mouse models of breast and colon cancer metastasizing to the brain and liver (unpublished data). Strikingly, six genes overlapped between the shielding signature and the colonization signature, representing strong candidates for mediating shielding-like functions during metastatic colonization. Among these, Trem2 was consistently overexpressed at the mRNA level across all analyzed models (see Introduction 1.2.3).

These findings prompted us to focus on TREM2^{+} macrophages during metastatic colonization, given their potential relevance in shaping the microenvironment and possibly contributing to shielding-like mechanisms in metastasis (Zhong et al., 2024). To begin, we analyzed the expression of *Trem2* in our brain metastasis mouse models. *Trem2* expression remained stable across all conditions, with no significant differences between the tumor models or the ECM-injected control group (Figure 17). In contrast, *ApoE*, a well-established ligand of TREM2 (Deczkowska et al. 2020; Wang et al. 2025), was markedly upregulated in metastatic brain tissue derived from E0771-LG injections. This suggests that TREM2 signaling in brain metastasis may be modulated more prominently at the level of ligand availability rather than receptor abundance, pointing toward model-specific activation dynamics.

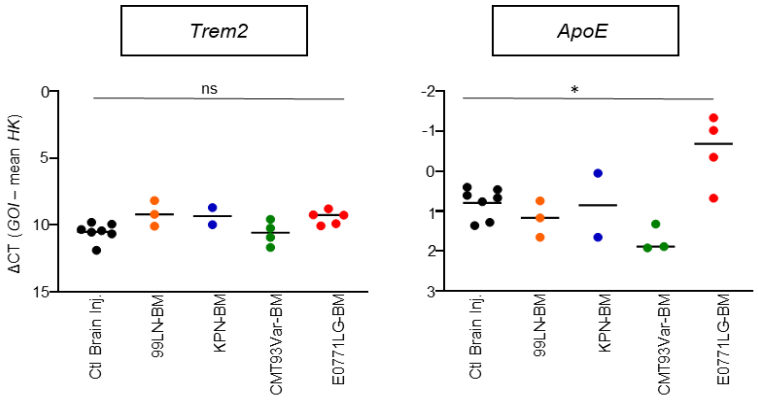

Figure 17. Characterization of TREM2 on MG/BMDM populations in the metastatic brain.

qRT-PCR analysis of *Trem2* and its ligand *ApoE* gene expression level in ECM-injected controls (Ctl) and BM from 99LN, KPN, CMT93Var and E0771-LG. *Gapdh* and *Pgk1* were used as housekeeping (HK) genes. P-value was calculated with one-way ANOVA followed by Tukey's multiple comparisons tests (*P<0.05, **P<0.01, ***P<0.001, ****P< 0.0001, ns= not significant).

3.3. Role of TREM2 during metastatic colonization

Building on the central hypothesis of this doctoral thesis, which posits, as previously mentioned, that TREM2 functions as a key regulator of shielding macrophages during metastatic colonization and contributes to the establishment of an immunosuppressive microenvironment within the brain metastatic niche, we sought to further dissect the mechanisms underlying TREM2-mediated macrophage regulation. To investigate this pathway in more detail, BMDMs were stimulated *in vitro* with established TREM2 ligands under defined conditions (Deczkowska et al. 2020), allowing us to characterize TREM2 pathway activation and its influence on macrophage morphology. These experiments aimed to elucidate the role of TREM2 in shaping macrophage phenotype and function *in vitro*, thereby providing mechanistic insights into tumor–macrophage interactions within the brain metastatic microenvironment.

3.3.1. Characterization of TREM2 signaling in macrophages

Trem2 wildtype (WT) and deficient (KO) mice were used for studying the function of Trem2 in macrophages. Due to the known impact of TREM2 on lipid metabolism (Damisah et al. 2020), we first evaluated potential differences in size and weight of the donor animals. Representative images of WT and KO mice showed no visible phenotypic differences, and body weights were comparable between groups (Figure 18A and B).

Next, Trem2 deletion was confirmed at the genomic level in experimental mice and isolated BMDMs. Genotyping confirmed the presence of the expected 369 bp band in both the Trem2 KO breeding mice (ear sample) and the isolated BMDMs, indicating successful Trem2 deletion *in vivo* and at cellular level (Figure 18C and D).

We then analyzed the maturation and purity of isolated BMDMs by Fluorescence-activated cell sorting (FACS) analysis using CD45, CD11b, Ly6G and Ly6C markers and the gating strategy adapted from (Klemm et al. 2021). CD45 confirmed the leukocyte origin of the cells, CD11b identified the myeloid population, Ly6G excluded residual neutrophils, and Ly6C distinguished the mature macrophage subsets. One day after isolation, the cellular population isolated from WT and TREM2 KO mice consisted of 46% and 48% myeloid (CD45+/Cd11b+) cells, respectively (Figure 18E, upper panel). The myeloid composition significantly increased during the cultivation period, reaching up to 99% and 96% in WT and KO mice at day 7 after isolation (Figure 18E, lower panel). In addition, we observed a significant decrease in the proportion of the Ly6G+/Ly6C+ cells from day 1 to day 7, which shows the elimination of the granulocytes as well as the successful differentiation of monocytes to macrophages, respectively. Importantly, TREM2 did not affect macrophage maturation (Figure 18F).

Additionally, we investigated the role of TREM2 in shaping macrophage responses, particularly following activation of downstream signaling by two of its well-characterized ligands, lipopolysaccharide (LPS) and apolipoproteins such as ApoE. These ligands engage TREM2 signaling to initiate pathways regulating cell survival, proliferation, chemotaxis, and phagocytosis, thereby contributing to immune homeostasis (Li et al. 2023). We evaluated the expression of *Trem2* through its two adaptor proteins/genes: Tyrobp/*Dap12* and Hcst/*Dap10*, in WT and Trem2 KO macrophages, under basal conditions and upon stimulation with ApoE or LPS. The absence of Trem2 did not affect the expression of the adaptor proteins, even upon pathway activation. Solely the stimulation with LPS led to a significant decrease in the expression of Trem2 itself, indicating that TREM2 is dynamically regulated in response to specific inflammatory stimuli, such as LPS, while the downstream adaptor components remain largely unaffected (Figure 18G).

These findings indicate that while TREM2 deficiency does not globally impair macrophage differentiation, its role in macrophage biology is likely mediated through post-transcriptional

mechanisms or context-dependent signaling rather than through baseline transcriptional control.

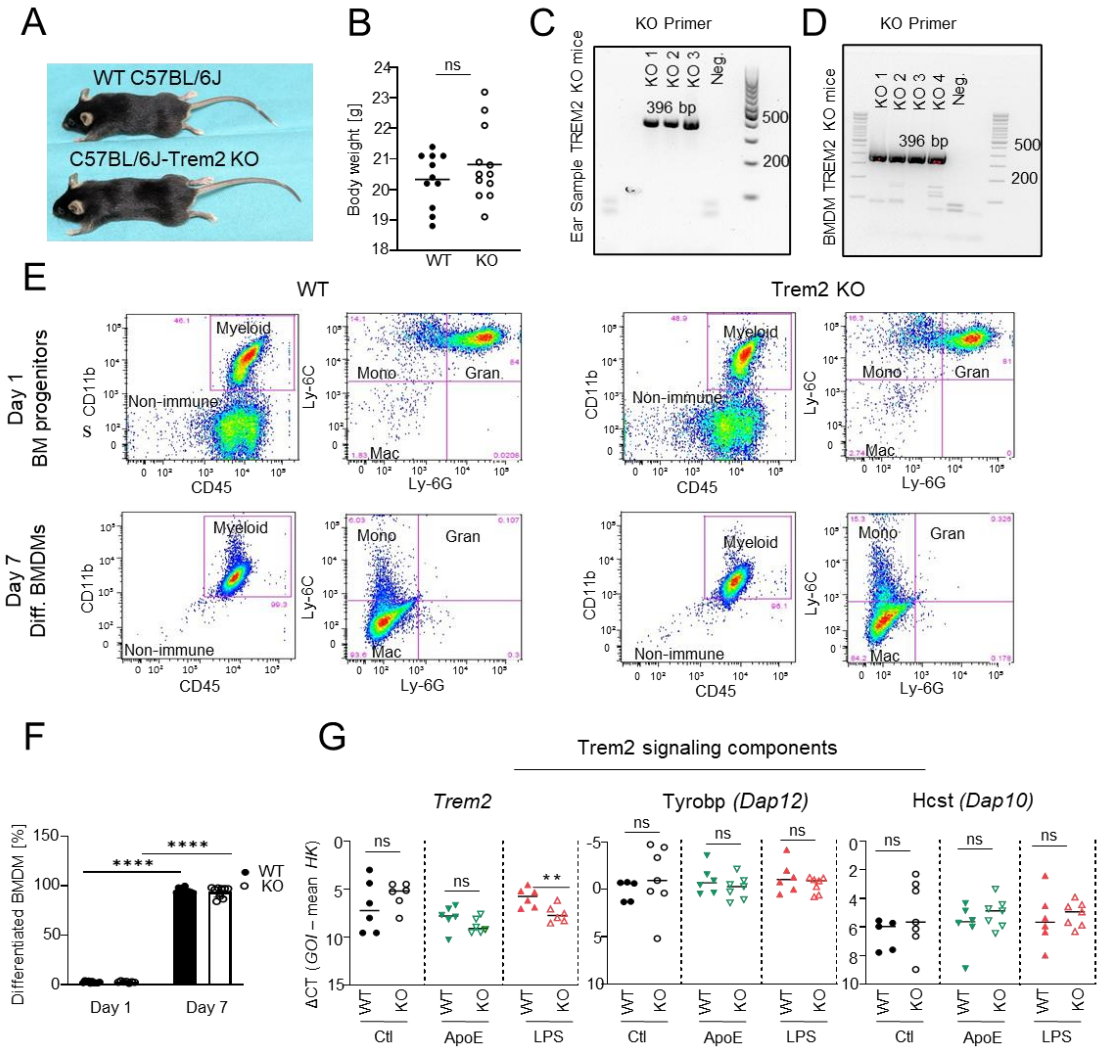

Figure 18. Characterization of TREM2 signaling in macrophages.

(A) Representative images of WT and TREM2 KO mice. (B) Graph representing weight of WT and TREM2 KO mice at 10-12 weeks. (C) Agarose gel electrophoresis (2%) of PCR products and genotyping Trem2 KO ear tissue. (D) Agarose gel electrophoresis (2%) of PCR products and genotyping Trem2 KO BMDM. (E) Representative FACS plots of WT and TREM2 KO BMDMs on day 1 (upper panel) and day 7 (lower panel) with the following gating strategy BMDMs (CD45+CD11b+Ly6C-Ly6G-). (F) Percentage of fully differentiated BMDM in WT and TREM2 KO at day 1 vs. 7. P-value was calculated with unpaired t-test (*P<0.05, **P<0.01, ***P<0.001, ****P< 0.0001, ns=not significant). (G) qRT-PCR analysis of Trem2 signaling components (*Trem2, Dap12 and Dap10*) genes in WT vs. Trem2 KO BMDMs under control (Ctl) conditions or after stimulation with ApoE 1µg/ml or LPS 10 ng/ml for 24h. *Gapdh* and *Pgk1* were used as housekeeping (HK) genes. P-value was calculated with ROUT Outliner Test followed by unpaired t test (*P<0.05, **P<0.01, ***P<0.001, ****P< 0.0001, ns=not significant).

3.3.2. Characterization of TREM2-dependent polarization and lipid-associated markers in macrophages

To further assess the impact of TREM2 on macrophage polarization and inflammatory responses, we performed qRT-PCR analysis on BMDMs under control (unstimulated) conditions and following stimulation with ApoE or LPS, targeting genes involved in inflammatory signaling and immunomodulation. Therefore, we analysed the expression of proinflammatory cytokines and the classical M1 (*Tnfα, Il-1ß,* and *Il-6*) and M2 (*Arg1*, *Mrc1* and *Spp1*) polarization markers revealed distinct but inconsistent expression patterns between Trem2 KO and WT BMDMs, indicating no stable biological effect. Our results revealed no significant changes in the expression of the proinflammatory genes (*Il-1ß,* and *Il-6*) between WT and Trem2 KO macrophages. However, for the M1-associated pro-inflammatory cytokine *Tnfα*, Trem2 KO BMDMs showed higher basal expression and further induction upon ApoE stimulation compared with WT. In contrast, LPS, despite being a well-established activator of M1 responses, did not substantially alter *Tnfα* expression in either genotype. Among M2-associated genes, *Arg1* was significantly upregulated in WT BMDMs at baseline, whereas *Mrc1* (CD206) was reduced compared with TREM2 KO BMDMs. Notably, *Spp1* expression remained unchanged between WT and TREM2 KO BMDMs. Neither ApoE nor LPS stimulation significantly altered *Arg1*, *Mrc1* or *Spp1* expression, suggesting a complex and marker-specific regulation of M2 genes in the absence of TREM2 (Figure 19A and B). This contradictory regulation points to an altered transcriptional responsiveness in BMDMs, potentially reflecting TREM2-dependent cellular states that influence polarization capacity.

Besides its known role as a TAM marker (Nakamura and Smyth 2020), TREM2 has been more extensively studied in the context of neurodegenerative diseases, particularly in Alzheimer's disease. There, TREM2 plays a beneficial role in clearing amyloid-β plaques and myelin debris (Nugent et al. 2020; Wang et al. 2015). Consistent with previous findings (McQuade et al. 2020), we observed a basal downregulation of glycoprotein NMB (*Gpnmb*) and lipoprotein lipase (*Lpl*) expression, both of them involved in lipid clearance, in Trem2 KO BMDMs under basal conditions. Interestingly, this effect was lost upon pathway activation, indicating that TREM2-dependent regulation of lipid-handling genes is context-dependent and may be overridden by strong external stimuli, such as ApoE or LPS, which can engage alternative signaling pathways to maintain lipid metabolism in macrophages (Figure 19C). To assess further surface markers involved in lipid uptake, we performed flow cytometric analysis of CD36 and CD9 cell surface receptors that play crucial roles in the transport and signaling of

fatty acids and other lipids (Jaitin et al. 2019). Both markers showed reduced fluorescence intensity in TREM2 KO BMDMs, with CD36 being significantly downregulated under basal conditions (Figure 19D).

Taken together, our findings indicate that TREM2 deficiency shapes baseline transcriptional programs toward a partial M1-like phenotype, consistent with previous reports (Fang et al. 2024; Molgora et al. 2020; Nakamura and Smyth 2020). However, our results only partially align with these studies, as we observed a marked upregulation of the M2 marker *Mrc1* in Trem2 KO BMDMs, suggesting that polarization outcomes are highly dependent on the specific type of stimulation applied. This underscores that TREM2 acts as a context-dependent regulator of macrophage polarization rather than a fixed determinant of M1/M2 states. Furthermore, the loss of TREM2 appears to impair macrophage lipid trafficking, reflected by reduced expression of genes and surface proteins involved in lipid uptake, intracellular transport, and metabolic clearance.

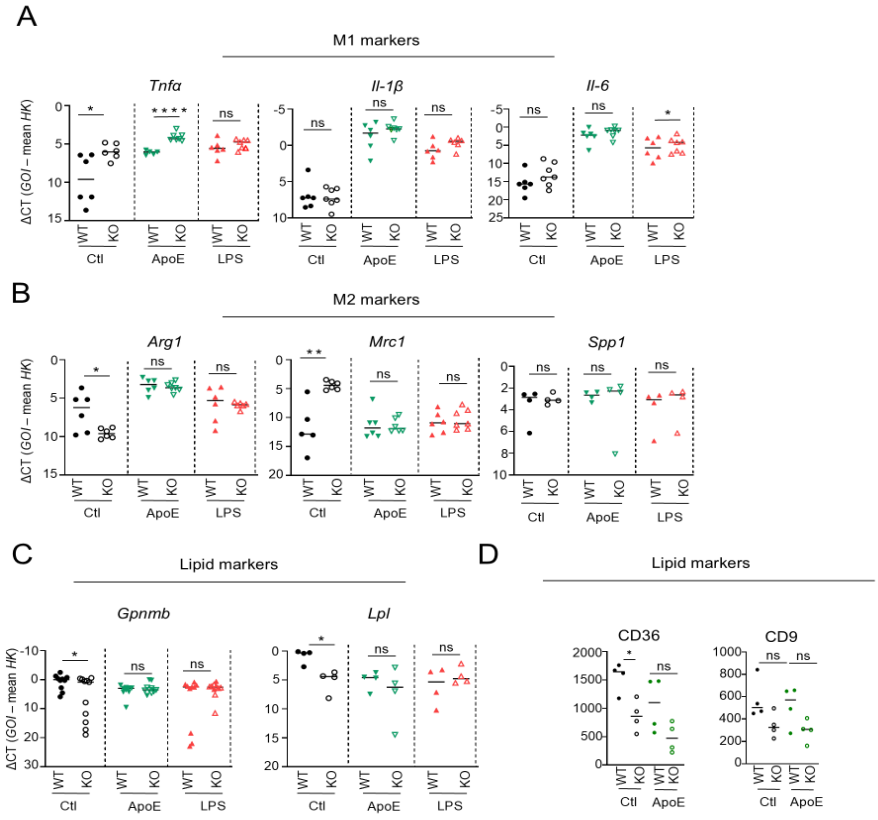

Figure 19. Characterization of TREM2-dependent polarization and lipid-associated markers in macrophages.

(A) qRT-PCR analysis of M1 (*Tnfα, Il-1ß & Il-6*) and (B) M2 (*Arg1*, *Mrc1 & Spp1*) genes in WT vs. Trem2 KO BMDMs under control conditions (Ctl) or after stimulation with ApoE 1µg/ml or LPS 10 ng/ml for 24h. *Gapdh* and *Pgk1* were used as housekeeping (HK) genes. P-value was calculated with ROUT Outliner Test followed by unpaired t test (*P<0.05, **P<0.01,

***P<0.001, ****P< 0.0001, ns=not significant) (C) qRT-PCR analysis of the Lipid genes (*Gpnmb* & *Lpl*) in WT vs. Trem2 KO BMDMS under Ctl, ApoE 1µg/ml or LPS 10 ng/ml stimulation for 24h. *Gapdh* and *Pgk1* were used as housekeeping (HK) genes. P-value was calculated with ROUT Outliner Test followed by unpaired t test (*P<0.05, **P<0.01, ***P<0.001, ****P< 0.0001, ns=not significant). (D) FACS analysis of the lipid-associated markers (CD36 & CD9) in WT vs. Trem2 KO BMDMS under Ctl or ApoE 1µg/ml stimulation. Data represent mean fluorescence intensity (MFI) values, calculated by subtracting the isotype control MFI from the sample MFI. P-value was calculated with unpaired t-test (*P<0.05, **P<0.01, ***P<0.001, ****P< 0.0001, ns=not significant).

3.3.3. Effect of TREM2 on macrophage morphology and lipid metabolism

Given that TREM2 functions as a lipid-sensing receptor in macrophages, shaping their metabolic and functional state in lipid-rich environments (Damisah et al. 2020), we next examined how it influences lipid-associated morphological changes. In particular, we analyzed the cytoskeletal architecture of isolated BMDMs under basal conditions and after 24-hour stimulation with known TREM2 ligands, ApoE, or LPS (Deczkowska et al. 2020) using phalloidin-conjugated TRITC (red) staining. We identified four distinct morphologies among BMDMs (Figure 20A), three of which are well-described in the literature: rounded, elongated, and star-like (Menzyanova et al. 2019). The fourth morphology, defined as the foamy phenotype, is increasingly recognized as the lipid-laden macrophage morphology (Pang et al. 2024). Under basal conditions and following LPS stimulation, the rounded and elongated morphologies were predominant, with occasional star-like cells. Strikingly, the foamy phenotype was most prominent upon ApoE stimulation, particularly in TREM2 KO BMDMs. The quantification confirmed a significantly increased proportion of foamy macrophages in the TREM2 KO BMDMs following ApoE stimulation, but not with LPS alone (Figure 20B). These findings indicate that TREM2-deficient BMDMs adopt a foamy phenotype upon ApoE stimulation, reflecting the critical role of TREM2 in modulating macrophage responses to lipid cues (Jaitin et al. 2019).

Foamy macrophages in Trem2-deficient settings have been linked to impaired cholesterol efflux, where free cholesterol is esterified by acyl-CoA:cholesterol acyltransferase (ACAT), leading to intracellular cholesterol ester accumulation (Nugent et al. 2020). To further dissect this process, we performed lipidomic profiling of WT and TREM2 KO BMDMs under basal, ApoE, and LPS stimulation conditions in collaboration with Gerhard Liebisch group. Among membrane lipids, free cholesterol (FC) levels were significantly elevated in WT compared to TREM2 KO BMDMs across all conditions, suggesting reduced cholesterol accumulation in WT cells. In contrast, phosphatidylcholine (PC), a major membrane phospholipid facilitating lipid transport, was markedly upregulated in TREM2 KO BMDMs upon ApoE and LPS

stimulation, whereas sphingomyelin (SM), a critical regulator of cholesterol homeostasis and transport (Wang et al. 2015), was significantly downregulated in the same conditions. These opposing changes in PC and SM indicate impaired cholesterol trafficking and storage in TREM2 KO BMDMs, consistent with the observed foamy phenotype. No significant differences were detected in storage lipids, or lysosomal lipids between WT and TREM2 KO cells (Figure 20C).

Together, these findings demonstrate that TREM2 deficiency disrupts cholesterol homeostasis and promotes lipid-laden macrophage phenotypes specifically upon ApoE stimulation, highlighting a key role for TREM2 in maintaining macrophage lipid balance under lipid-rich conditions.

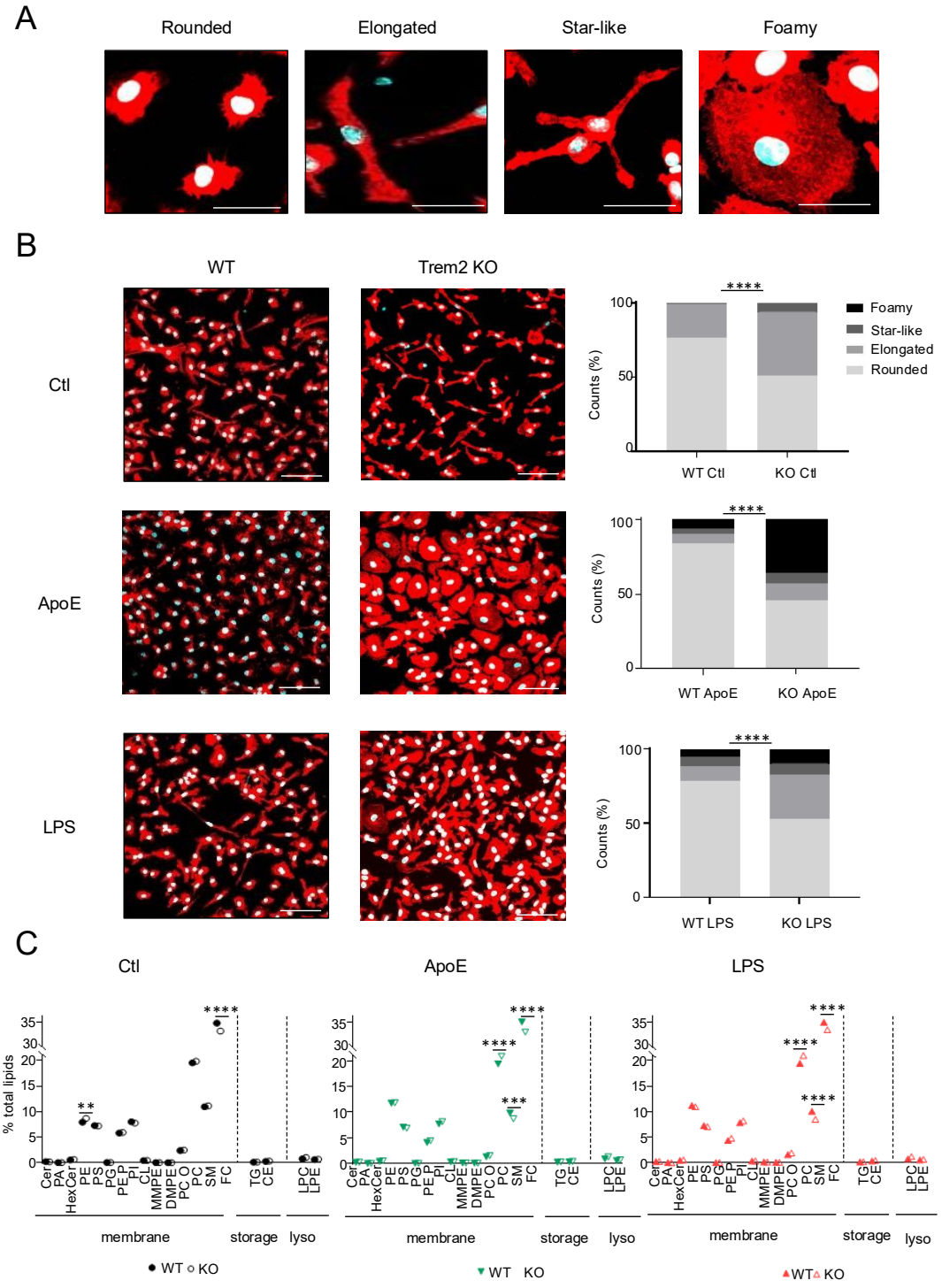

Figure 20. Characterization of TREM2's effect on macrophage morphology and lipid metabolism.

(A) Representative confocal images of each BMDM morphology after phalloidin-conjugated TRITC (red) staining. Scale bars represent 50 µm. (B) Representative confocal images (left) and corresponding quantification of the percentual counts (right) of WT and Trem2 KO BMDM under control conditions (Ctl) or after stimulation with ApoE 1µg/ml or LPS 10 ng/ml for 24h and Phalloidin-conjugated TRITC (red) staining. Scale bars represent 100 µm. P-value was calculated using Mann-Whitney test; (*P < 0.05, **P < 0.01, ***P < 0.001, ****P< 0.000,

ns=not significant). (C) Percentual quantification of the total lipid classes in WT and Trem2 KO BMDMs under Ctl, ApoE 1µg/ml, or LPS 10 ng/ml stimulation. Lipid classes were grouped into membrane, storage, and lysosomal (lyso) lipids (for all lipid abbreviations see 6.3.). Each point represents the mean value. P-value was calculated using two-way ANOVA with multiple comparisons; (*P < 0.05, **P < 0.01, ***P < 0.001, ****P< 0.000, ns=not significant).

3.3.4. Effect of TREM2 on mitochondrial morphology, quantity and function

Given the pivotal role of mitochondria in maintaining energy homeostasis and orchestrating lipid metabolic processes (Li et al. 2024), and building upon our findings on TREM2 in downregulation of lipid associated markers and acquisition of a foamy morphology, we next investigated mitochondrial morphology, quantity and function. For this, BMDMs from WT and TREM2 KO mice were analyzed under basal conditions or following stimulation with ApoE or LPS using a combination of techniques, including electron microscopy (EM), immunofluorescence (IF), flow cytometry (FACS), real-time oxygen consumption measurements, as well as assessments of mitochondrial membrane potential and calcium dynamics.

EM analysis revealed rounded or elongated mitochondria under all conditions, with no signs of pathological morphology such as swelling, cristae disruption, or fragmentation. Additionally, we did not observe any significant differences in the number of mitochondria per cell and the total mitochondrial area between control, ApoE-, or LPS-treated groups (Figure 21).

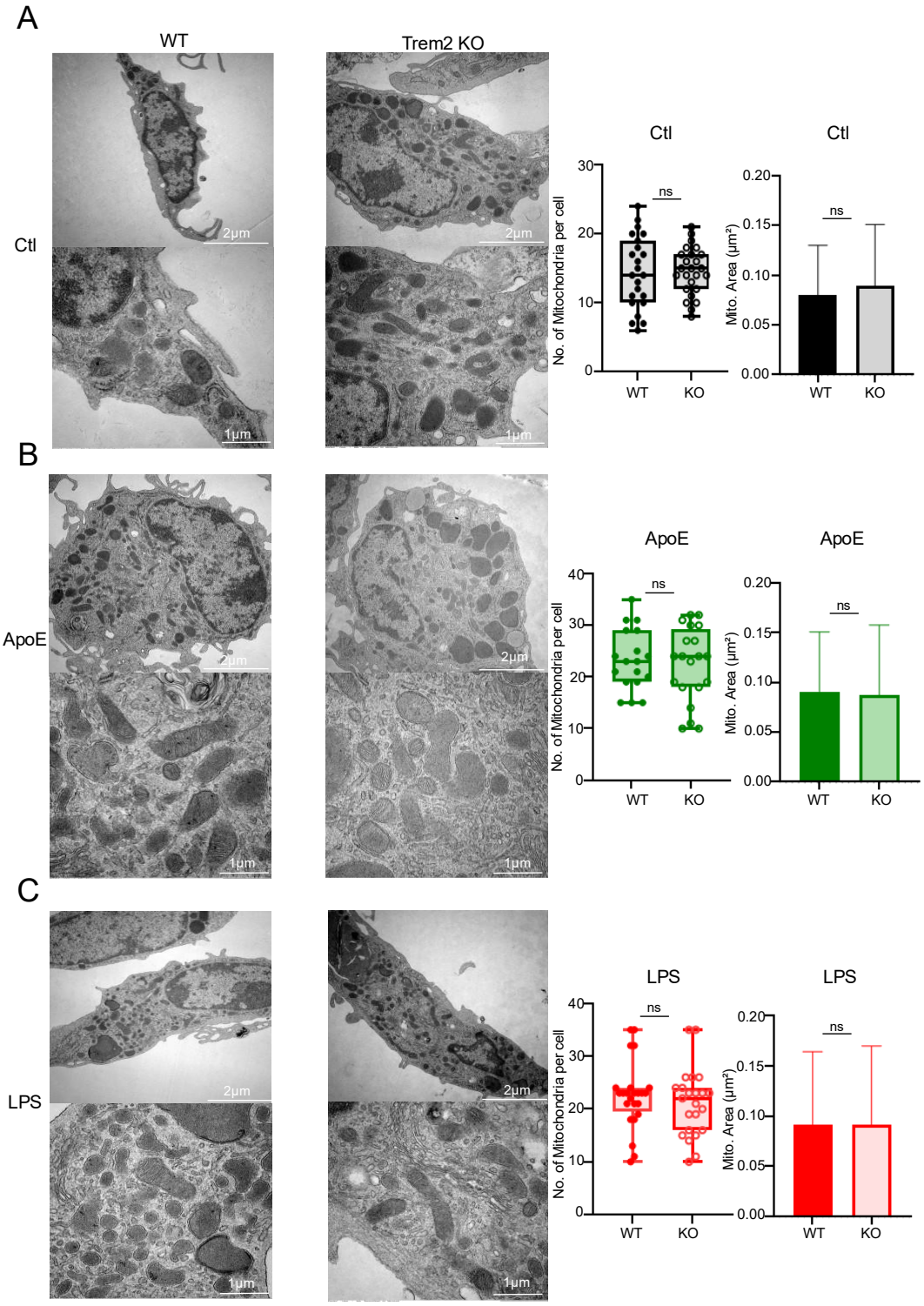

Figure 21. Characterization of TREM2's effect on mitochondrial morphology upon electron microscopy imaging.

(A) Representative electron microscopy images showing mitochondrial morphology (left) and quantification of mitochondrial number per cell and mitochondrial area (µm²) (right) of (A) untreated (Ctl) WT and TREM2 KO BMDMs. (B) WT and TREM2 KO BMDMs stimulated with ApoE 1µg/ml, and (C) WT and TREM2 KO BMDMs stimulated with LPS 10 ng/ml for

24h. Scale bars represent 2µm and 1µm, respectively. P-value was calculated with unpaired t-test * = WT vs. KO (ns=not significant).

To further assess the mitochondrial morphology and numbers, we employed an additional approach by staining BMDMs with MitoTracker Green, a dye that accumulates in the mitochondrial matrix and reveals overall mitochondrial shape, size, and network pattern (Neikirk et al. 2023). Interestingly, mitochondria in TREM2 KO BMDMs exhibited a more fragmented or punctate morphology compared to WT BMDMs, which displayed a more interconnected mitochondrial network (Figure 22A). These observations are consistent with previous reports (Ulland and Colonna 2018; van Lengerich et al. 2023). These differences in the shift from networked to punctate mitochondrial morphology in Trem2 KO BMDMs, were not seen in electron microscopy (Figure 21), suggesting functional or metabolic alterations rather than gross structural changes. Next, we employed MitoTracker Green for flow cytometric quantification of mitochondrial content. Across all conditions, basal, ApoE-stimulated, and LPS-stimulated, the mean fluorescence intensity was generally lower in TREM2 KO BMDMs, albeit not significant. Notably, under ApoE stimulation, this reduction was statistically significant compared to WT BMDMs (Figure 22B). To assess mitochondrial function, we conducted respirometry using a PreSens system to measure oxygen consumption. In all three conditions (basal, ApoE, and LPS stimulation), TREM2 KO BMDMs exhibited elevated oxygen consumption, with the most pronounced difference observed following LPS stimulation (Figure 22C). This contrasts with prior reports of reduced mitochondrial respiration in Trem2 KO myeloid cells (Ulland and Colonna 2018) and suggests that these cells fail to undergo the expected glycolytic switch under inflammatory conditions.

Additionally, we evaluated mitochondrial membrane potential (MMP) using ratiometric fluorophore JC-1 (5,5’,6,6’-tetrachloro-1,1’,3,3’-tetraethylbenzimidazolylcarbocyanineiodide) staining. Under normal conditions, complexes I, III, and IV of the electron transport chain actively pump protons into the intermembrane space, thereby maintaining the mitochondrial electrochemical gradient. A decrease in membrane potential, reflected by a lower green/red fluorescence ratio in JC-1 staining, indicates mitochondrial depolarization and suggests potential dysfunction in these complexes (Sivandzade et al. 2019). Upon ApoE stimulation, TREM2 KO BMDMs showed a significantly reduced membrane potential, while LPS stimulation led to a significantly increased membrane potential compared to WT LPS (Figure 22D).

Mitochondria play a critical role in Ca^{2+} homeostasis, which is essential for numerous signalling pathways, enzyme function, and cellular metabolism. Driven by their negative membrane potential, they attract and accumulate calcium ions within the mitochondrial matrix, thereby directly influencing and regulating cellular Ca^{2+} dynamics. With their capability to store or release calcium ions, mitochondria serve as calcium buffers with both beneficial and detrimental effects (Dong et al. 2017). The MMP, along with Ca^{2+}-conducting channels (e.g. voltage-dependent anion channel, VDAC) and the activity of Ca^{2+}-transporting proteins in the IMM (e.g. mitochondrial calcium uniporter, MCU), influence the extent of mitochondrial Ca^{2+} uptake (Bravo-Sagua et al. 2017). Using Ca^{2+}-sensitive dyes, the cytosolic $[Ca^{2+}]_c$, as well as mitochondrial $[Ca^{2+}]_m$ levels, were investigated. Cytosolic Ca^{2+} concentrations were measured by loading the cells with the ratio metric dye Fura-2, which is characterised by two excitation spectra depending on its Ca^{2+}- bound or Ca^{2+}-free state, and is directly related to the cytosolic amount of calcium. For the assessment of the mitochondrial Ca^{2+} levels, the intensity-based dye Rhod-2/AM was used. Fura-2 and Rhod-2 fluorescence measurements in TREM2 KO and WT BMDMs While cytosolic calcium levels remained unchanged under basal conditions, mitochondrial calcium levels were significantly reduced in TREM2 KO BMDMs, indicating mitochondrial dysfunction (Figure 22E) (van Lengerich et al. 2023). Following ApoE and LPS stimulation, both cytosolic and mitochondrial calcium levels were significantly lower in TREM2 KO BMDMs compared to WT (Figure 22E). Collectively, these results suggest that TREM2 deficiency leads to mitochondrial dysfunction in BMDMs, as evidenced by altered mitochondrial structure, content, calcium homeostasis and impaired bioenergetic function relative to WT cells.

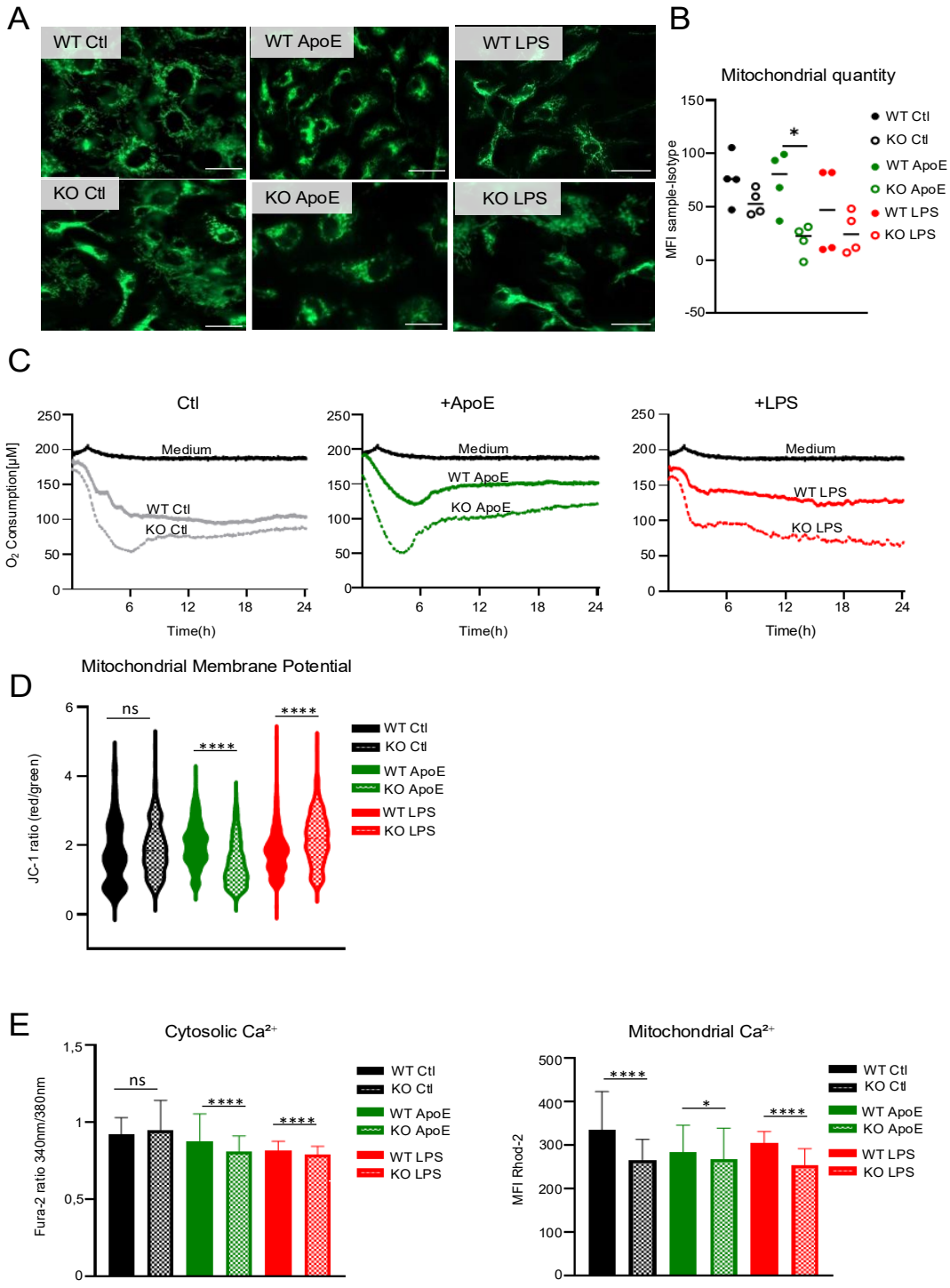

Figure 22. Characterization of TREM2's effect on mitochondrial morphology and function.

(A) MitoTracker green images of WT vs. TREM2 KO BMDMs either unstimulated Ctl or with ApoE 1µg/ml, LPS 10 ng/ml stimulation for 24h. Scale bar represent 20 µm. (B) FACS quantative analysis of MitoTracker green in WT vs. TREM2 KO BMDMs either unstimulated Ctl or with ApoE 1µg/ml, LPS 10 ng/ml stimulation for 24h. Data represent mean fluorescence

intensity (MFI) values, calculated by subtracting the isotype control MFI from the sample MFI. P-value was calculated with unpaired t-test (*P<0.05, **P<0.01, ***P<0.001, ****P< 0.0001, ns=not significant). (C) PreSens line graphs showing oxgen consumption in µM of WT vs. TREM2 KO BMDMs either unstimulated Ctl or with ApoE 1µg/ml, LPS 10 ng/ml stimulation for 24h. (D) Violin plot of the median JC-1 fluorescent ratio of red/green (JC-1 aggregates/monomers) showing MMP of the WT vs. TREM2 KO BMDMs either unstimulated Ctl or with ApoE 1µg/ml, LPS 10 ng/ml stimulation for 24h. P-value was calculated with unpaired t-test * = WT vs. KO (*P<0.05, **P<0.01, ***P<0.001, ****P< 0.0001, ns=not significant). (E) Analysis of cytosolic and mitochondrial Ca^{2+} concentrations in WT vs. TREM2 KO BMDMs either unstimulated Ctl or with ApoE 1µg/ml, LPS 10 ng/ml stimulation for 24h, using Fura-2 and Rhod-2 dyes, respectively. Column bar graphs show cytosolic Ca^{2+} levels as indicated by Fura-2/AM fluorescence ratio $F_{340/380}$ while the mitochondrial Ca^{2+} concentration as indicated by Rhod-2/AM mean fluorescence intensity (MFI). P-value was calculated with unpaired t-test * = WT vs. KO (*P<0.05, **P<0.01, ***P<0.001, ****P< 0.0001, ns=not significant).

3.3.5. Summary of TREM2's effect on shaping macrophage responses in a context-dependent manner *in vitro*

To provide a comprehensive overview of our previously described results on the role of TREM2 in regulating macrophage function, we summarized gene/protein expression profiles, cell morphology, and metabolic parameters in WT and TREM2 KO BMDMs under basal conditions and following ApoE or LPS stimulation in Table 20. Overall, TREM2 loss did not lead to a uniform shift toward either a pro- or anti-inflammatory phenotype. Instead, we observed stimulus-dependent and sometimes contradictory changes across transcriptional, morphological, and metabolic readouts. At the transcriptional level, WT macrophages generally showed reduced expression of the pro-inflammatory marker *Tnfα* and elevated *Arg1*, whereas TREM2 KO macrophages displayed increased *Tnfα* expression and higher *Mrc1* levels, highlighting the absence of a consistent TREM2-driven polarization program. Morphologically, WT BMDMs tended to adopt elongated or star-like shapes under stimulation, whereas TREM2 KO BMDMs displayed a pronounced foamy phenotype characterized by lipid accumulation, particularly following ApoE stimulation. These differences were accompanied by distinct metabolic and lipidomic adaptations: Across all conditions, WT BMDMs consistently displayed higher proportions of free cholesterol (FC) and sphingomyelin (SM), whereas TREM2 KO BMDMs showed elevated phosphatidylcholine (PC) levels specifically following ApoE and LPS stimulation. Functionally, WT macrophages demonstrated reduced oxygen consumption, a more interconnected mitochondrial network, enhanced mitochondrial performance, increased membrane potential, and tightly controlled Ca^{2+} flux. In contrast, TREM2-deficient macrophages exhibited increased oxygen consumption, fragmented

mitochondrial architecture, impaired mitochondrial function, diminished membrane potential, and disrupted Ca^{2+} regulation.

Collectively, these results demonstrate that Trem2 deficiency does not impose a uniform macrophage phenotype. Instead, **Trem2 modulates transcriptional, morphological, and metabolic responses in a highly context-dependent manner**, with effects varying according to the type of external stimulus.

Table 20. Overview of TREM2's effect on shaping macrophage responses in a context-dependent manner.

Condition	Gene/ protein expression	Morphology	Lipidomics	Mitochondrial status
WT Ctl	↓M1(*Tnfα*), M2 (↑ *Arg1*, ↓*Mrc1*),↑ Lipid genes/proteins	Rounded/ Elongated	Free cholesterol (FC)↑	↓O_2, ↑mito. Ca^2
KO Ctl	↑M1(*Tnfα*), M2 (↓*Arg1*, ↑*Mrc1*), ↓ Lipid genes/proteins	Rounded/ Elongated	Free cholesterol (FC) ↓	↑O_2, ↓mito. Ca^{2+}
WT ApoE	↓M1(*Tnfα*)	Rounded	Free cholesterol (FC)↑, sphingomyelin (SM)	↑Mitochondria, ↓O_2, ↑ membrane potential (MMP), ↑ cyto.,mito.Ca^{2+}
KO ApoE	↑M1(*Tnfα*)	Foamy dominant/ Rounded	Phosphatidylcholine (PC) ↑	↓Mitochondria, ↑O_2, ↓ membrane potential (MMP), ↓ cyto., mito Ca^{2+}
WT LPS	No sign. changes	Elongated/star-like	Free cholesterol (FC)↑, sphingomyelin (SM)	↓O_2, ↑membrane potential (MMP), ↑cyto., mito Ca^{2+}
KO LPS	No sign. changes	Rounded/Elongated	Phosphatidylcholine (PC) ↑	↑O_2, ↓membrane potential (MMP), ↓cyto., mito Ca^{2+}

Summary table showing WT and TREM2 KO BMDMs either unstimulated Ctl or with ApoE 1µg/ml, LPS 10 ng/ml stimulation. Gene and protein expression changes of M1 (*Tnfα*) and M2 markers (*Arg1*, *Mrc1*) as well as lipid-related genes (*Gpnmb*, *Lpl*) /proteins (CD36, CD9) are indicated. Cellular morphology is categorized as rounded, elongated, star-like, or foamy. Lipidomics data reflect the proportion of total membrane lipids. Mitochondrial parameters include oxygen consumption (O_2), overall mitochondrial function; mitochondrial membrane potential (MMP), and cytosolic/mitochondrial Ca^{2+} levels. Arrows indicate the direction of change (↑ increase, ↓ decrease) relative to WT Ctl, ApoE or LPS stimulation.

3.3.6. Impact of TREM2 on tumor/macrophage interplay *in vitro*

Besides the role of TREM2 in regulating macrophage lipid metabolism, it has been implicated as a TAM marker, where it influences both tumor growth and immune evasion (Binnewies et al. 2021). To investigate TREM2's role in this context, we assessed how its deletion affects macrophage–tumor cell interactions *in vitro*. Using 3D co-culture systems and migration assays, we evaluated the capacity of TREM2-deficient macrophages to engage with tumor cells relative to their wild-type counterparts. This approach allowed us to dissect the specific contributions of TREM2 signaling to the dynamic interplay between tumor cells and macrophages, laying the groundwork for our subsequent *in vivo* analyses.

3.3.6.1. Effect of TREM2 on the tumor/macrophage interplay

Given TREM2's pivotal role in shaping the immune landscape (Binnewies et al. 2021), we next sought to investigate the interactions between BMDMs and tumor cells with distinct HGPs, namely non-infiltrative, epithelial infiltrative and diffuse infiltrative, by establishing 3D co-culture spheroids. WT and TREM2 KO BMDMs were co-seeded at a 1:1 ratio with either KPN, 99LN (non-infiltrative brain metastasis models), E0771-LG (diffuse infiltrative model), or CMT93Var (epithelial infiltrative model). Prior to spheroid formation, BMDMs were labeled with IB4-568, and all cells were counterstained with DAPI to allow tracking. The spheroid formation phase lasted up to three days (Day −3 to Day 0), during which cultures were monitored to assess their growth, morphology, and cell–cell interactions over time.

Fluorescence imaging enabled visualization of BMDM distribution within the tumor spheroids. In the 99LN and KPN (non-infiltrative) models, BMDMs consistently failed to integrate into the tumor spheroids and instead formed independent spheroids with no apparent interaction with the tumor cells. Inspired by (Galon and Bruni 2019), we referred to this as a "separated" phenotype (Figure 23A). In contrast, spheroids derived from the diffuse infiltrative E0771-LG model showed pronounced BMDM infiltration into the tumor core, forming a unified structure that reflects an "inclusive" phenotype (Figure 23A). The epithelial infiltrative CMT93Var model exhibited an "exclusive" phenotype, in which macrophages co-localized with tumor cells in the same spheroid but remained predominantly at the periphery.

Importantly, these distinct interaction patterns were consistent across both WT and TREM2 KO BMDMs, indicating that TREM2 does not significantly influence macrophage behavior in this context. Instead, the observed differences in macrophage–tumor interaction appeared to be governed by the tumor's HGP.

To further explore the role of TREM2 in macrophage migration and tumor interaction, we performed two-well migration assays using WT and Trem2 KO BMDMs co-cultured with either 99LN or E0771-LG tumor cells. In line with the observations from our 3D spheroid assays, the non-infiltrative 99LN model consistently maintained a well-defined boundary, exhibiting minimal macrophage recruitment regardless of TREM2 expression. In contrast, the diffusely infiltrative E0771-LG model facilitated robust macrophage migration toward the tumor cells. Consistently with the previous assay, this effect was similarly observed in both WT and Trem2 KO BMDMs (Figure 23B).

Overall, these findings suggest that the degree and spatial organization of macrophage–tumor cell interaction in 3D co-culture settings are determined primarily by the intrinsic HGP of the tumor cells, rather than by TREM2-dependent signaling in macrophages. They also suggest that macrophage migration toward tumor cells is strongly influenced by the HGP phenotype of the tumor rather than by TREM2-dependent signaling.

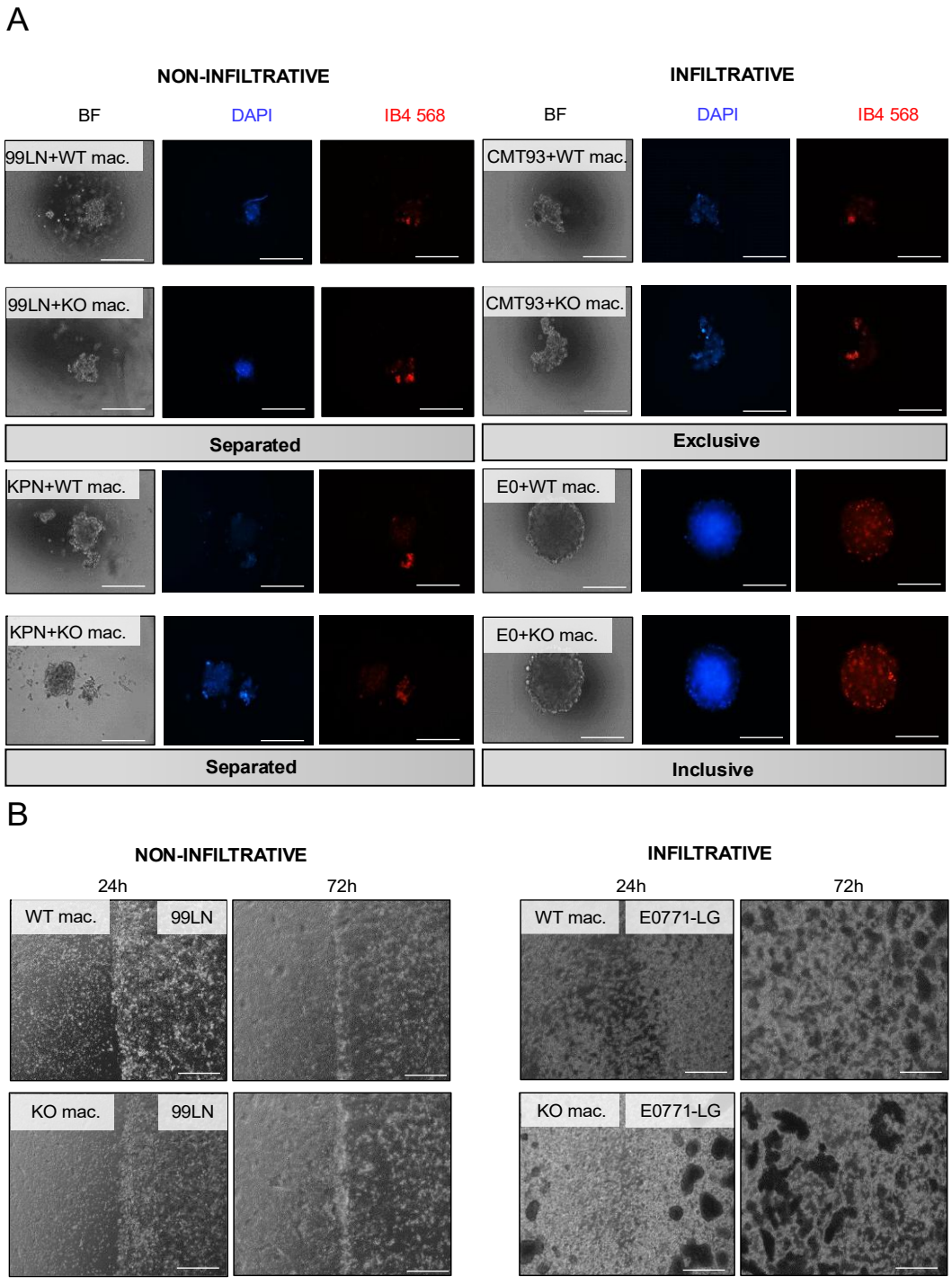

Figure 23. Effects of TREM2 on tumor/macrophage interplay in vitro.

(A) Representative images of 3D tumor spheroids generated by co-culturing tumor cells (99LN, KPN, CMT93Var, and E0771-LG) with WT or TREM2 KO BMDMs at a 1:1 ratio. BMDMs were labeled with Cytopainter Deep Red dye, and nuclei of tumor cells and BMDMs were counterstained with DAPI. Images were acquired at 10x magnification. Scale bars represent 400 µm. (B) Representative images of migration assay at 24h and 72h showing E0771-LG and 99LN tumor cells seeded in two-well inserts and co-cultured with either WT or TREM2 KO BMDMs. Scale bars represent 1000 µm.

3.3.7. Impact of TREM2 on experimental models of brain metastasis

Considering the critical role of myeloid cells in driving metastatic progression, and their responsiveness to TREM2 signaling, it became essential to investigate how TREM2 influences macrophage activity during CNS colonization *in vivo*. Our working hypothesis posited that disrupting TREM2 signaling would impair the tumor-promoting functions of BMDMs and microglia, typically associated with their M2-like, TREM2-driven shielding. As a result, we anticipated that TREM2 KO mice would exhibit extended survival compared to WT controls.

To address this, we employed our well-established BM syngeneic mouse models (Alves de Lima et al. accepted). The following sections detail a comprehensive comparison between WT and TREM2 KO mice, encompassing overall survival, colonization index (CI), metastatic architecture at the MMPI, immune cell infiltration patterns, and cytokine expression profiles.

3.3.7.1. Effects of TREM2 on HGP, CI and survival in brain metastasis mouse models

Taking into account the emerging role of TREM2 in macrophage function (Sun et al. 2023), together with the previously reported heterogeneous effects of TREM2 during tumor progression (see Table 21), we aimed to investigate its impact across various HGPs in our experimental metastasis mouse models. For the analysis of the metastatic colonization, we selected and characterized models with different HGPs. Tissue sections from the infiltrative models (E0771-LG, CMT93Var) and non-infiltrative models (KPN, 99LN) were stained using IHC with Ck8 to visualize tumor architecture. This allowed us to clearly distinguish the distinct HGPs among the four models: the diffuse infiltrative model E0771-LG exhibited extensive, disorganized infiltration of tumor cells into the surrounding tissue; CMT93Var, classified as an epithelial infiltrative model, displayed a more structured growth with tumor cells forming glandular-like or cohesive clusters; in contrast, the non-infiltrative models KPN and 99LN demonstrated a pushing growth pattern, with tumor masses sharply demarcated from the adjacent parenchyma and compressing surrounding healthy tissue. Despite these distinct morphological differences among the models, no significant alterations in HGPs were observed between WT and TREM2 KO conditions (Figure 24A).

In E0771-LG-injected mice (the diffuse infiltrative model), the appearance of metastasis occurred very early in both WT and TREM2 KO mice, showing a severe impact on the survival of the animals with median of 2 to 3 weeks after intracortical injection. Interestingly, TREM2 did not show any significant effect on the overall survival of the mice; both WT and TREM2

KO models reached very similar endpoints with the median OS of WT=14.5 days and TREM2 KO 16 days (Figure 24B). In mice injected with CMT93Var (the epithelial infiltrative model) we found very low successful colonization with a percentage of WT 46% and TREM2 KO 33% (Figure 24C). There were no differences between WT and TREM2 KO mice injected with the cell line, since both groups developed neurological symptoms at a median OS of WT= 85.5 days and TREM2 KO= 71 days after injection (Figure 24B). In 99LN and KPN-injected mice (the non-infiltrative models) TREM2 did not show any significant effect on survival as the mice reach very similar endpoints. In order to compare the colonization capacity of E0771-LG, CMT93Var, KPN and 99LN BM models in WT and TREM2 KO syngeneic mice, the CI was calculated (Figure 24C). The diffuse-infiltrative model E0771-LG retained its high colonizing capacity in WT mice as well as in the TREM2 KO mice (CI_{WT}=0.69, CI_{KO}=0.625). The CMT93Var model displayed the least aggressive colonization potential in WT as well as TREM2 KO mice (CI_{WT}=0.054, CI_{KO}=0.046). The colonization potential of the non-infiltrative models KPN and 99LN had a very slight change in both WT and KO mice (KPN CI_{WT}=0.12, CI_{KO}=0.08) (99LN CI_{WT}=0.14, CI_{KO}=0.12) (Figure 24D). These results indicate that TREM2 does not significantly influence either the HGP, survival, or colonization efficiency in these BM models.

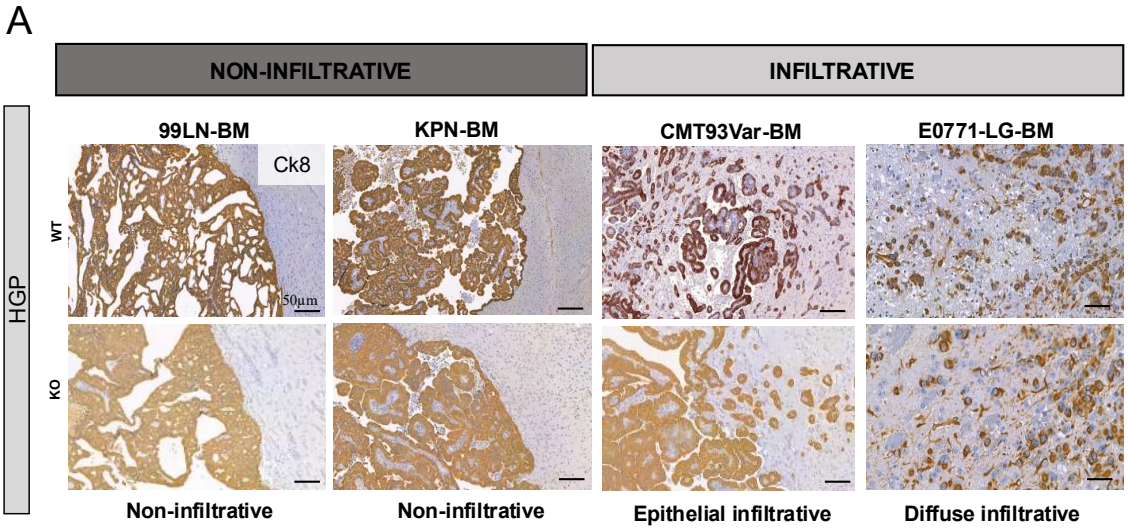

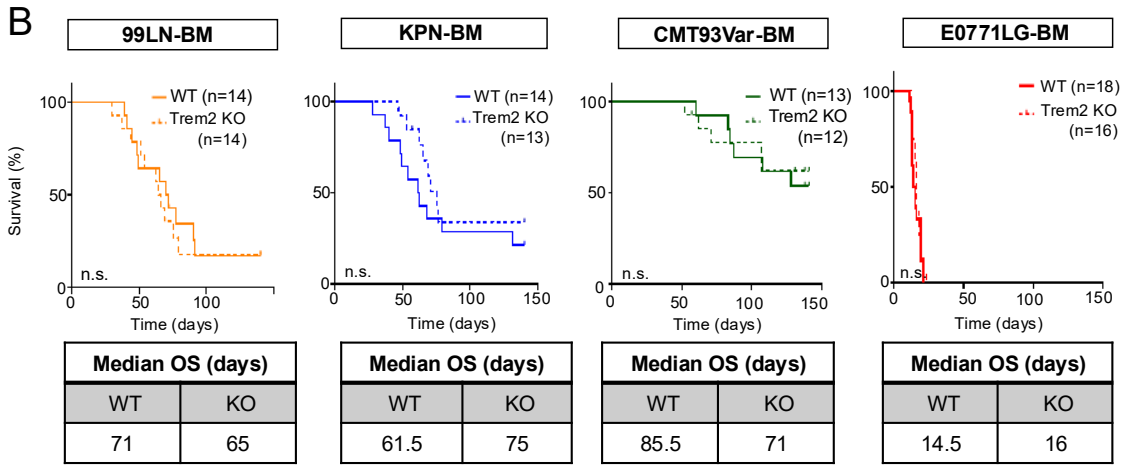

Median OS (days)	
WT	KO
71	65

Median OS (days)	
WT	KO
61.5	75

Median OS (days)	
WT	KO
85.5	71

Median OS (days)	
WT	KO
14.5	16

C

$$CI = \frac{successful\ \ colonization\ \ (\%)}{injected\ \ cells\ \ (N)\ x\ median\ \ OS\ (days)}\ x\ 100$$

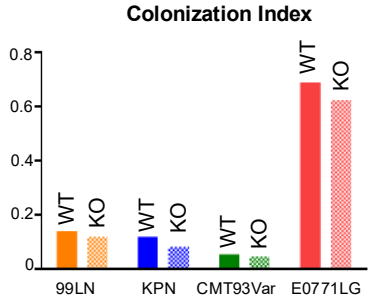

D

Geno type	Inj. Cells	Event of Mets.	Success. Coloniz-ation	Mdn OS days	Coloniz ation Index
99LN	WT	1000	11/14	79%	71	0.140
	KO	1000	11/14	79%	65	0.12
KPN	WT	1000	10/14	71%	61.5	0.12
	KO	1000	8/13	62%	75	0.08
CMT93Var	WT	1000	6/13	46%	85.5	0.054
	KO	1000	4/12	33%	71	0.046
E0771-LG	WT	1000	18/18	100%	14.5	0.69
	KO	1000	16/16	100%	16	0.625

Figure 24. Effects of TREM2 in BCBM and CCBM mouse models on HGP, CI and overall survival.

(A) Representative IHC staining of Ck8 showing the HGP in tissue sections of WT vs. Trem2 KO 99LN, KPN, CMT93Var & E0771-LG-induced BM. Scale bars represent 50 µm. (B) Kaplan-Meier curve showing the overall survival (OS) of the WT and TREM2 KO syngeneic mice injected with breast (99LN, E0771-LG) and colorectal cancer (KPN, CMT93Var) cell

lines. P-value was calculated with Log-rank (Mantel-Cox) test (n.s.= not significant). (C) Colonization index (CI) comparison among WT vs. Trem2 KO injected with 99LN, KPN, CMT93Var & E0771-LG cell lines. The mathematical equation is depicted. (D) Summary table illustrating the parameters considered for the comparative evaluation of WT and TREM2 KO mice in terms of event of metastasis, successful colonization, median overall survival (OS) and colonization index.

3.3.7.2. The microenvironment in TREM2 KO brain metastasis mouse models

The impact of TREM2 signaling on the immune landscape of brain-MME was assessed through immunohistochemical analysis and mRNA expression profiling, as previously described (see Methods 2.2.3). To characterize the activation states of key immune and glial populations, we employed markers specific for microglia/macrophages (Iba1), astrocytes (Gfap), and T cells (Cd3). Comparative analysis of brain metastatic tissues from WT and TREM2 KO mice were performed to assess differences in immune cell activation and spatial distribution.

3.3.7.2.1. Characterization of MG/BMDM in TREM2 KO metastatic brain mouse models

In BM, TAMs comprising both tissue-resident MG and BMDMs, represent a major immunosuppressive cell population within the brain-MME, particularly when polarized toward an M2-like phenotype (Klemm et al. 2020). While the specific roles of these ontogenetically distinct TAM subsets in BM remain unclear, our previous data indicate that TREM2 is a common driver for shielding during metastatic colonization (unpublished data). Accordingly, disrupting TREM2 signaling, as in TREM2 KO mice, could offer a therapeutic strategy to reduce the M2-TAM population and, by extension, the immunosuppressive burden in the brain-MME.

In this study, the overall distribution of MG/BMDMs was comparable between WT and KO mice, regardless of the tumor model. Iba1-positive macrophages were consistently localized to the metastatic core and the MMPI, with no evidence of activation in the contralateral, non-injected hemisphere. Furthermore, gene expression analysis of *Iba1* revealed no significant differences in macrophage abundance between WT and KO mice across all four BM models (E0771LG, CMT93Var, KPN and 99LN) (Figure 25), indicating that TREM2 deletion does not impact TAM recruitment or overall density in this context.

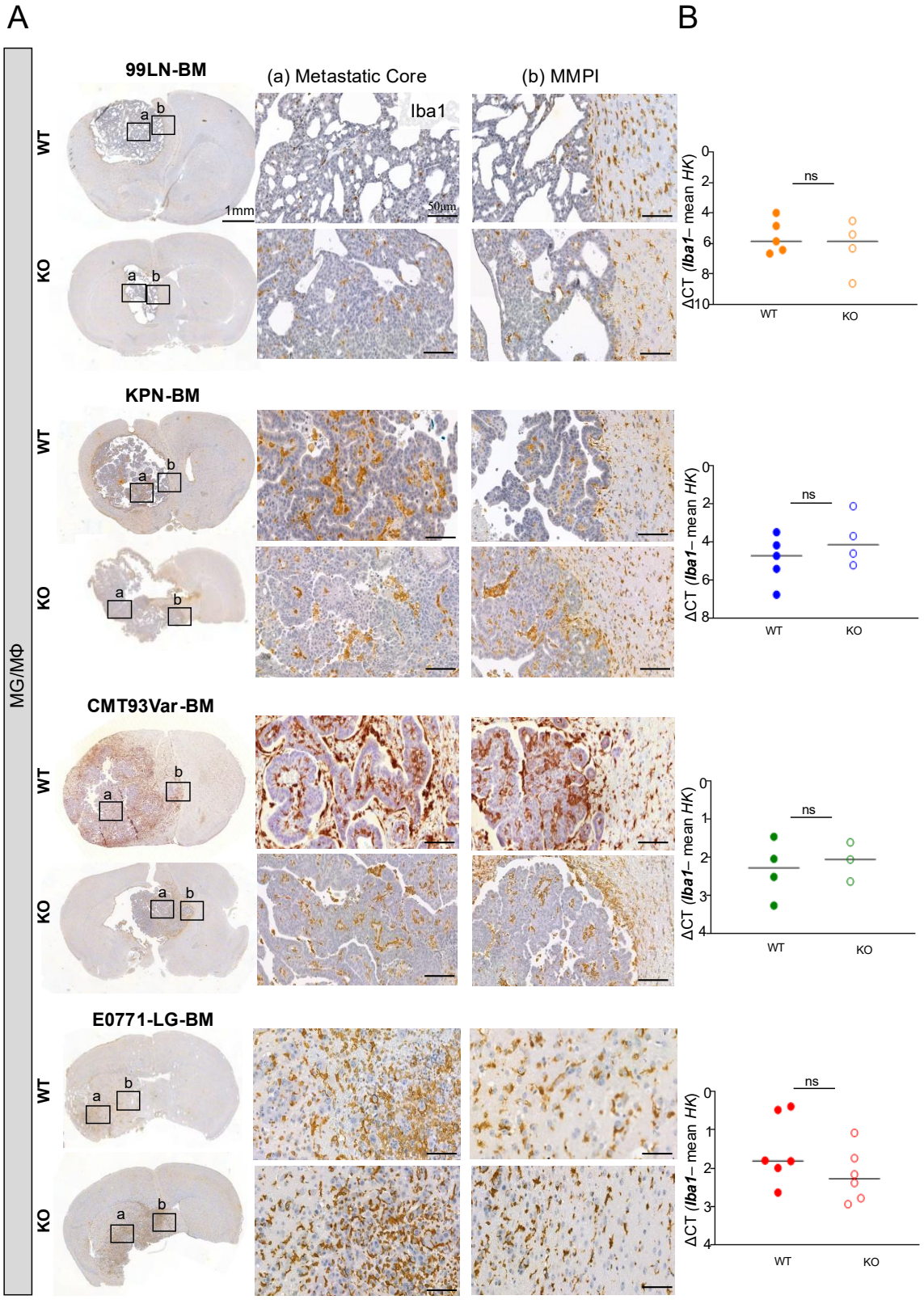

Figure 25. Characterization of MG/BMDM population in the metastatic brain of WT and TREM2 KO mice.

(A) IHC images of brain tissues after staining of MG/BMDM populations with Iba1 marker of WT and KO mice injected with 99LN, KPN, CMT93Var and E0771LG. Representative images

of coronal brain sections and magnifications of the MMPI and metastatic core are shown. Scale bars indicate 200 µm and 50 µm, respectively. (B) qRT-PCR analysis of *Iba1* gene expression levels between WT and KO-derived brain tissues injected with the corresponding BM model (99LN, KPN, CMT93Var and E0771LG). *Gapdh* and *Pgk1* were used as housekeeping (HK) genes. P-value was calculated with unpaired t-test (ns=not significant).

3.3.7.2.2. Characterization of astrocytes in TREM2 KO metastatic brain mouse models

Astrocytes, as key regulators of central nervous system homeostasis, play a dynamic role in shaping the tumor microenvironment in BM. Beyond their classical supportive functions, reactive astrocytes can acquire tumor-promoting properties by engaging in cross-talk with immune and tumor cells, contributing to an immunosuppressive niche that fosters metastatic progression (Zhou et al. 2025). Notably, the precise interactions between TREM2 signaling and astrocyte function remain unclear, making it particularly important to investigate the role of reactive astrocytes in the absence of TREM2.

Immunohistological analysis revealed that reactive astrocytes were consistently localized around metastatic regions, with no observable differences in their distribution between WT and TREM2 KO mice (Figure 26). In the non-infiltrative models (KPN and 99LN), a pronounced glial boundary, characterized by Gfap-positive cells, surrounded the metastases, without any infiltration into the metastatic core, regardless of TREM2 status. Similarly, in the infiltrative models (E0771LG and CMT93Var), both WT and KO mice showed comparable patterns of reactive astrocyte clustering, with dense populations of Gfap-positive cells closely surrounding infiltrative tumor growth.

These findings were further supported by qRT-PCR analysis, which showed no significant differences in *Gfap* expression between WT and KO mice injected with any of the BM models (Figure 26). Overall, these results indicate that TREM2 signaling does not modulate astrocyte activation or distribution in the brain-MME, regardless of the metastatic growth pattern.

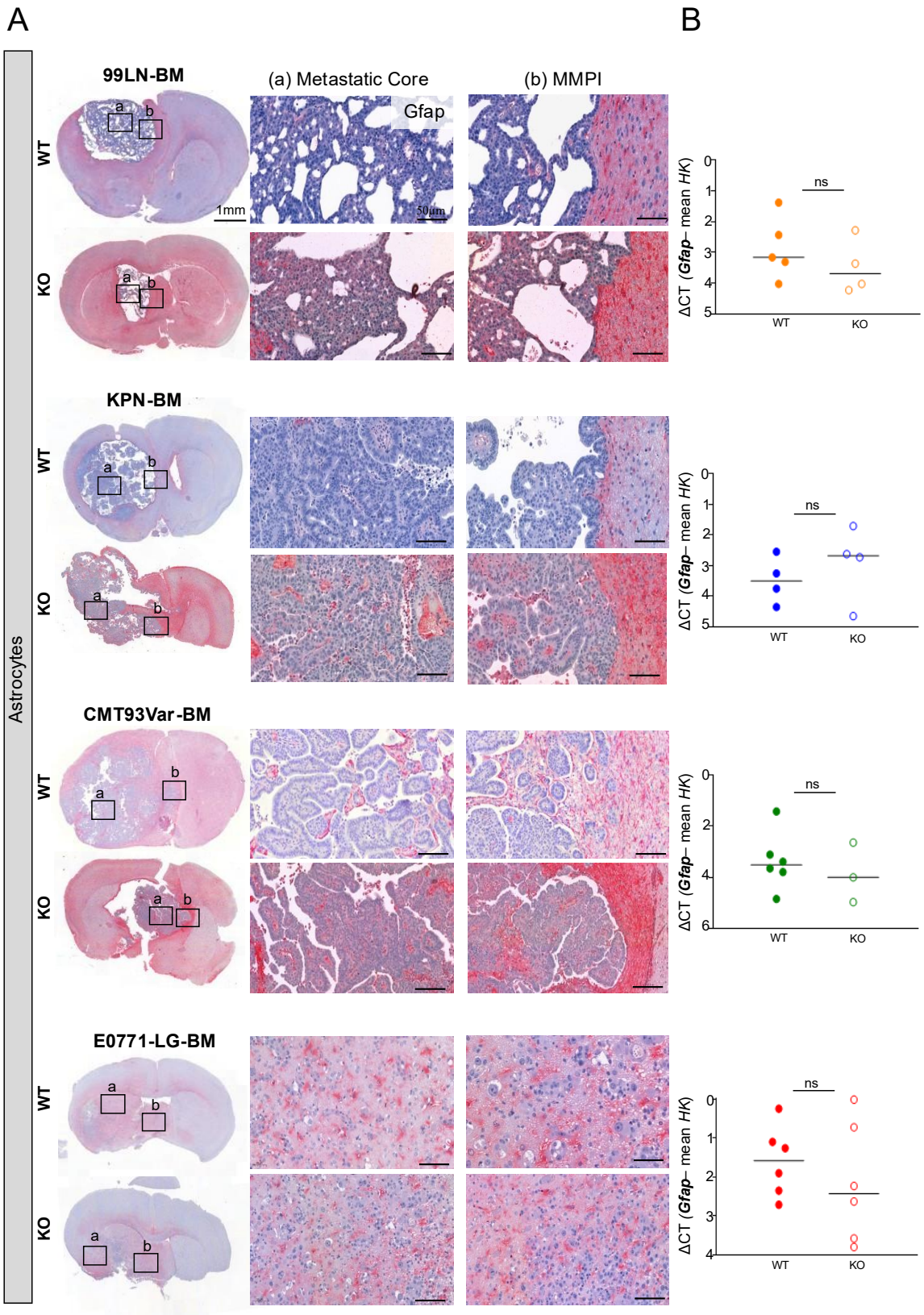

Figure 26. Characterization of astrocytes population in the metastatic brain of WT and TREM2 KO mice.

(A) IHC images of brain tissues after staining of astrocyte populations with Gfap marker of WT and KO mice injected with 99LN, KPN, CMT93Var and E0771LG. Representative images of

coronal brain sections and magnifications of the MMPI and metastatic core are shown. Scale bars indicate 200 µm and 50 µm, respectively. (B) qRT-PCR analysis of *Gfap* gene expression levels between WT and KO-derived brain tissues injected with the corresponding BM model (99LN, KPN, CMT93Var and E0771LG). *Gapdh* and *Pgk1* were used as housekeeping (HK) genes. P-value was calculated with unpaired t-test (ns=not significant).

3.3.7.2.3. Characterization of T cells in TREM2 KO metastatic brain mouse models

Under physiological conditions, T cell-mediated responses in the brain are typically limited. However, the function and presence of T cells can be significantly modulated by the surrounding brain microenvironment (Zakaria et al. 2018). Given that TREM2 is both expressed and secreted within the brain metastatic microenvironment, we assessed whether the absence of functional TREM2 signaling might influence the immunosuppressive landscape, specifically the T cell compartment.

In line with previous findings in WT mice, no Cd3-positive T cells were detected within the metastatic core or at the MMPI of KPN and 99LN tumors in TREM2 KO mice, further supporting the classification of these models as immunologically "cold." Conversely, the infiltrative models E0771LG and CMT93Var showed comparable levels of T cell infiltration in both WT and KO mice. In these models, Cd3-positive T cells were consistently present throughout the metastatic regions, including the MMPI zones, highlighting their more "immune-infiltrated" nature (Figure 27).

To complement the histological observations, gene expression analysis of *Cd3* was performed using qRT-PCR. Consistently, no significant differences in *Cd3* expression were observed between WT and KO conditions across all four BM models (Figure 27), indicating that TREM2 deficiency does not markedly affect T cell recruitment in this setting.

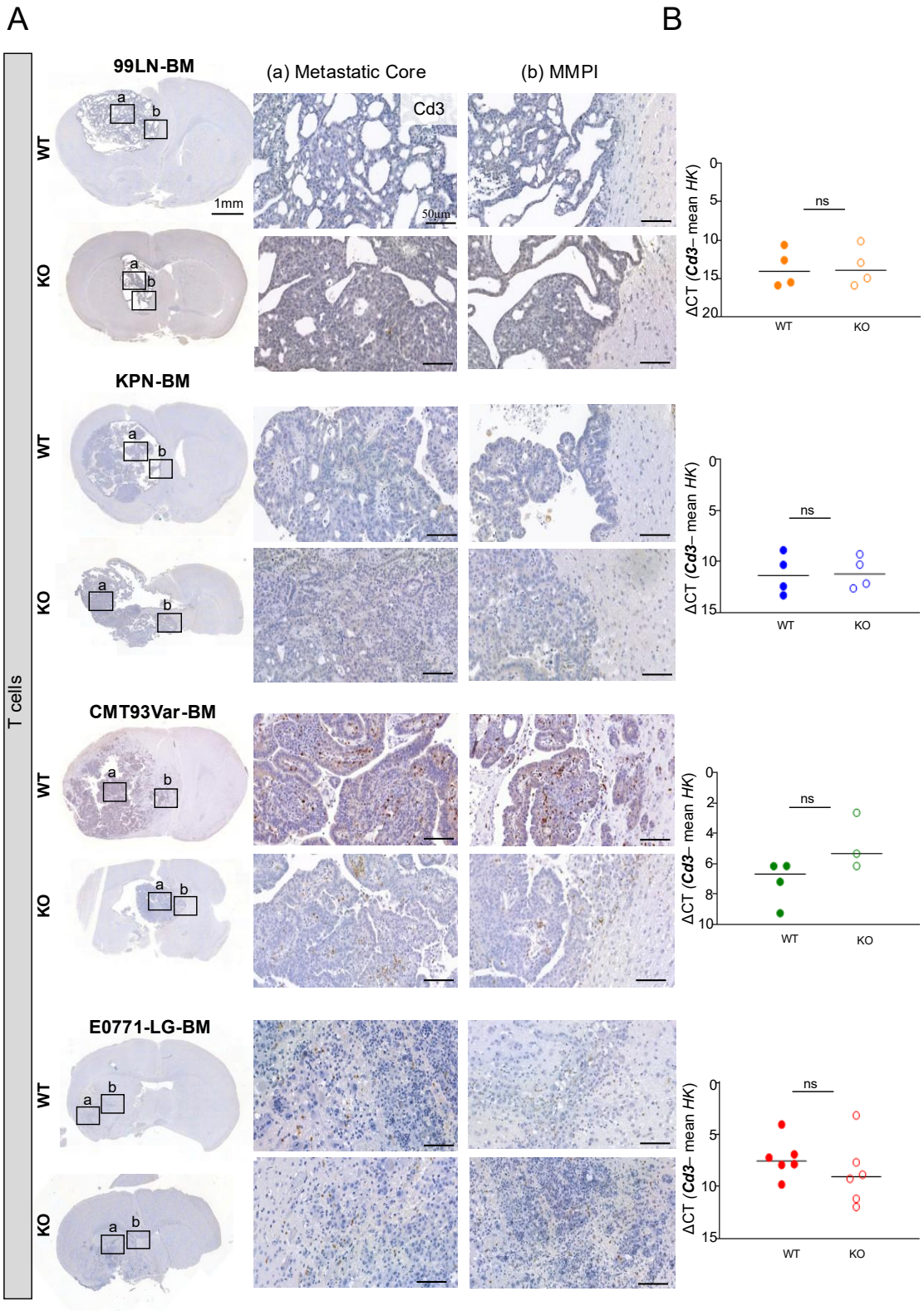

Figure 27. Characterization of T cells population in the metastatic brain of WT and TREM2 KO mice.

(A) IHC images of brain tissues after staining of T cells populations with Cd3 marker of WT and KO mice injected with 99LN, KPN, CMT93Var and E0771LG. Representative images of coronal brain sections and magnifications of the MMPI and metastatic core are shown. Scale bars indicate 200 µm and 50 µm, respectively. (B) qRT-PCR analysis of *Cd3* gene expression

levels between WT and KO-derived brain tissues injected with the corresponding BM model (99LN, KPN, CMT93Var and E0771LG). *Gapdh* and *Pgk1* were used as housekeeping (HK) genes. P-value was calculated with unpaired t-test (ns=not significant).

3.3.7.2.4. Effect of TREM2 on the MME of brain metastasis mouse models

To further assess the impact of TREM2 deletion on the brain microenvironment across the different metastatic models, we analyzed the expression of TREM2-associated genes (*Trem2*, *ApoE*, *Gpnmb*, and *Lpl*) alongside cytokine-related markers (*Il6*, *Il10*, and *Tgfß)* at the transcriptomic level. These data together with the immune markers were summarized and visualized as a heatmap (Figure 28), which revealed no significant differences between WT and TREM2 KO mice.

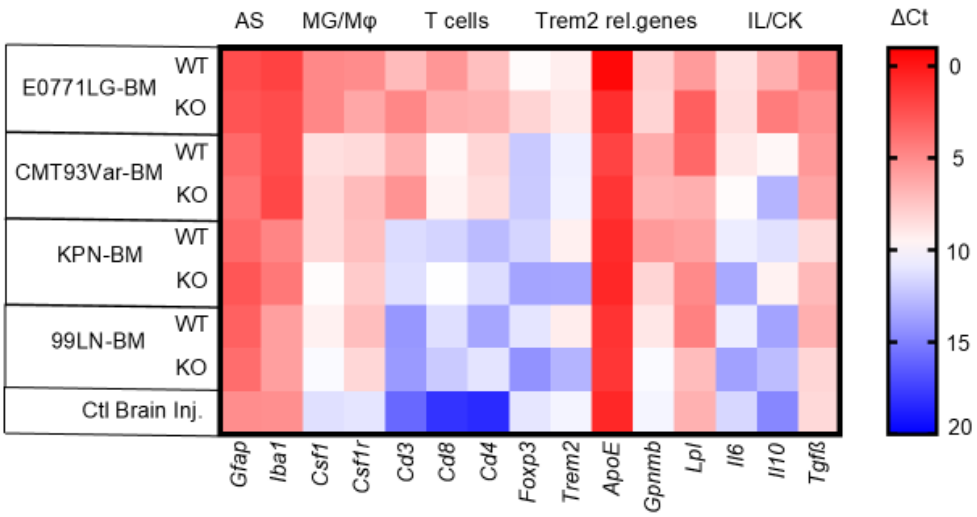

Figure 28. TREM2's effect in the MME of brain metastasis mouse models.

Heatmap displaying qRT-PCR analysis of selected genes within the injection site of BM tissue from WT and Trem2 KO mice across the E0771-LG, CMT93Var, 99LN, and KPN models. *Gapdh* and *Pgk1* were used as housekeeping (HK) genes. P-value was calculated with unpaired t-test WT vs. KO (ns=not significant).

Taken together, our comprehensive immunological evaluation, including histological and gene expression analyses, showed no detectable alterations in immune cell recruitment, cytokine expression, or tumor growth patterns in the brain MME of WT versus KO mice injected with 99LN, KPN, CMT93Var and E0771LG cells. These findings suggest that TREM2 deletion does not substantially influence immune dynamics or HGPs in the models and under the experimental conditions tested.

3.3.8. Summary of TREM2's distinct roles during tumor progression *in vivo*

To place our findings in the context of existing literature and resolve controversial findings on the role of TREM2 in tumor progression, we compiled and compared published studies investigating the role of TREM2 in WT versus TREM2 KO mice across various tumor types and experimental settings (Table 21). In our hands, using BM mouse models, genetic deletion of TREM2 did not alter survival outcomes, suggesting a limited or context-specific role of TREM2 in this setting. However, the broader literature reveals a striking inconsistency in outcomes depending on tumor type, immune context, and experimental parameters. For example, in glioma and pancreatic cancer models, TREM2 deficiency has been associated with improved survival, often in combination with therapies such as CSF1R or IL-1β inhibition, or AAV-mediated delivery of anti-PD1 (Yang et al. 2025; Zhong et al. 2024). In contrast, several studies using models of sarcoma, colorectal cancer, mammary tumors, or hepatocellular carcinoma report that TREM2 loss worsens survival, particularly when tumors are implanted subcutaneously or when anti-TREM2 or anti-PD1 therapies are involved (Molgora et al. 2020; Binnewies et al. 2021; Sun et al. 2023; Guo et al. 2025; Pierro et al. 2024). Furthermore, some reports, including ours, show no measurable effect of TREM2 deletion on tumor growth or survival, even under controlled housing and dietary conditions (Zheng et al. 2023; Peshoff et al. 2024). These divergent findings suggest that the function of TREM2 in tumor biology is highly context-dependent and may be shaped by factors such as tumor origin, colonization stage, immune microenvironment, microbiome status, and the use of immunotherapies. This highlights the need for standardized models to disentangle tumor-intrinsic versus microenvironmental contributions to TREM2 function.

Table 21. Overview of TREM2's distinct roles during tumor progression.

Effect Category	Reference	Mouse Strain	Age	Microbiome	Housing	Diet	Tumor Type	Injection Type	Therapy Used
(A) TREM2 Improves survival									
(A) Improves survival	Yang et al.,2025	C57BL/6 vs. TREM2 KO	~4-5 weeks	Ablated with antibiotics in some experiments	Standard at MDACC	Not specified	PDAC	Orthotopic 0.3×10^6 cells in 50 µL PBS	CSF1R inhibitor, IL-1ß inhibitor
(A) Improves survival	Zhong et al., 2024	C57BL/6 vs. TREM2 KO	8 weeks	specific-pathogen-free (SPF) status	12-h light-dark cycle at 24°C 26°C and 50–70% humidity	Not specified	GL261, CT-2A or EO771 cells	Intracranial $1.0x10^5$ in 2.5µl PBS	AAV-mediated TREM2 + anti-PD-1
(B) TREM2 worsens survival									
(B) Worsens survival	Molgora et al.,2020	C57BL/6 vs. TREM2 KO	8-10 weeks	SPF	Cohoused from birth, separated at injection	Not specified	Sarcoma (MCA1956), Colorectal (MC38), Mammary (PyMT)	Subcutaneous 10^6cells/mouse in 100µl PBS	Anti-PD1 (IP), anti-TREM2 (IP)
(B) Worsens survival	Binneweis et al., 2021	C57BL/6 vs. TREM2 KO	8--10 weeks	Not specified	Not specified	Ad libitum	Colorectal (CT26) and Ovarian Cancer (EMT6)	Subcutaneous $0.5x10^6$ EMT6 cells or $1x10^6$ CT26 cells	Anti-TREM2 mAb
(B) Worsens survival	Sun et al., 2023	C57BL/6 vs. TREM2 KO	6-8 weeks	Not specified	Standard	Not specified	SB28 and NPAC54B GBM	Orthotopic 10,000 cells for SB28 tumor 2000 cells for NPAC54B glioma	Anti-PD1
(B) Worsens survival	Pierro et al., 2023	C57BL/6 vs. TREM2 KO	8-9 weeks	Not specified	12h light/dark, 20--25°C, 30--70% humidity	LFD (lean), HFD (obese), switch (weight loss)	Breast Cancer (E0771 PDL1)	Orthotopic (mammary fat pad), $3.0x10^5$ in PBS	Anti-PD1
(B) Worsens survival	Guo et al, 2025	C57BL/6 vs. TREM2 KO	4 weeks	Not specified	Not specified	Not specified	Hepatocellular Carcinoma	Orthotopic and subcutaneous 3×10^6 Hepa 1–6 cells (1:1 mixed Matrigel)	anti-mouse CD8α
(C) TREM2 does not affect survival									
(C) No Effect	Zheng et al., 2023	C57BL/6 vs. TREM2 KO	8-14 weeks	Not specified	Standard (21-22°C, 55% humidity, IVC, 12h light/dark)	Ad libitum	Glioma (GL261)	Intracranial $5x10^4$ GL261 cells 1-2 µL PBS	None
(C) No Effect	Peshoff et al., 2023	C57BL/6 vs. TREM2 KO	8- 14 weeks	Not specified	Standard (21-22°C, 55% humidity, IVC, 12h light/dark)	Ad libitum	CT-2A-luc GL261-Luc	Intracranial $2x10^4$ CT-2A-luc or $1.0x10^5$ GL261-luc in serum-free DMEM	None

Summary table showing the comparative overview of studies investigating how TREM2 expression affects tumor progression and survival outcomes in mice. Studies are grouped into three categories: (A) TREM2 improves survival, (B) TREM2 worsens survival, and (C) TREM2 does not affect survival. Key experimental variables are shown, including mouse strain, age, microbiome status, housing conditions, diet, tumor type, injection type, and therapeutic interventions. Differences in tumor model, experimental setup, and immune modulation may underlie the observed discrepancies in TREM2 function across studies.

4. Discussion

BM continue to pose a significant clinical challenge due to their high mortality and the limited understanding of the biological mechanisms that drive their emergence and progression. The variability between patients and the frequent late-stage diagnosis of metastatic brain lesions contribute to the disease's rapid and often irreversible advancement. As such, unraveling the cellular and molecular events that govern the establishment of secondary tumors in the brain is vital, particularly the transition from early seeding to overt macrometastatic growth and subsequent secondary dissemination.

In this study, we investigate the brain metastatic colonization process with a specific emphasis on the different HGPs at the MMPI, a site increasingly acknowledged for its diagnostic and prognostic value. By employing models with both functional and deficient TREM2 signaling, a receptor involved in shaping the immune landscape, we aim to dissect how immune modulation influences metastatic behavior. Additionally, we explore how TREM2 affects macrophage lipid metabolism, offering insight into its role beyond immune regulation. Altogether, these findings enhance our understanding of how specific growth patterns at the MMPI correlate with immune activity and demonstrate the broader relevance of TREM2 in both tumor progression and macrophage metabolic function.

4.1. The different HGPs at the MMPI in BM models

Infiltrative HGPs correlate with worse survival rates than non-infiltrative growth patterns in patients with BM (Blazquez et al. 2020b; Siam et al. 2015; Proescholdt et al. 2025). These growth patterns not only offer clinical relevance but also reflect diverse underlying biological processes that contribute to metastatic progression. Notably, the extent to which tumor cells infiltrate the brain parenchyma has been identified as the most significant prognostic determinant, with highly infiltrative HGPs linked to markedly worse patient outcomes (Blazquez et al. 2020b; Proescholdt et al. 2025). The heterogeneity of these growth patterns suggests that different HGPs may harbor unique therapeutic susceptibilities. However, meaningful investigation into the biology of these colonization strategies demands robust experimental systems that mirror the diversity seen in human disease. In response to this need, the current study employs syngeneic mouse models specifically chosen to model both infiltrative and non-infiltrative HGPs, providing a relevant platform to explore the mechanisms and potential interventions associated with each pattern.

4.2. Limitations of the epithelial/mesenchymal status on the HGP in predicting colonization efficiency

In this study, four syngeneic murine models were employed to investigate the cellular and molecular dynamics of BM: two colorectal cancer models (CMT93Var and KPN) and two breast cancer models (E0771LG and 99LN). Following intracerebral injection into immunocompetent mice, each cell line exhibited distinct colonization indices and progressed to symptomatic BM at varying rates. Subsequent immunohistochemical analyses demonstrated marked differences in the HGPs among the models.

The E0771LG and CMT93Var models displayed an infiltrative growth pattern, characterized by active penetration of tumor cells into the brain parenchyma. In contrast, the 99LN and KPN models exhibited non-infiltrative growth, wherein tumor masses expanded by compressing surrounding brain tissue without direct parenchymal infiltration. These findings are consistent with previously established HGP at the MMPI classifications (Blazquez et al. 2020b), reinforcing the validity of the models. While the infiltrative nature of E0771LG and CMT93Var had been previously described within our laboratory, the HGPs of KPN and 99LN were characterized here for the first time. Their designation as non-infiltrative models represent a key contribution of this work.

To explore the potential determinants underlying these divergent colonization behaviors, the epithelial and mesenchymal phenotypes of the tumor cells were analyzed both *in vitro* and *in vivo*. All four cell lines exhibited adherent growth and co-expression of epithelial and mesenchymal markers to varying extents. Histological and transcriptomic analyses revealed a gradient of epithelial identity across the models. Notably, *Ecad* expression was relatively similar among CMT93Var, KPN, and 99LN, whereas E0771LG exhibited markedly reduced levels. Regarding mesenchymal traits, *Vim* expression varied more substantially: 99LN demonstrated the lowest levels, followed by intermediate expression in KPN and CMT93Var, while E0771LG showed the highest expression. These patterns align with EMT frameworks that associate stronger epithelial traits with reduced infiltration (Yang et al. 2020).

Interestingly, both CMT93Var and KPN exhibited a hybrid E/M phenotype, characterized by simultaneous expression of high *Ecad* and moderate to high *Vim* levels, particularly at the mRNA level. This suggests a partial EMT state, which has been associated with enhanced plasticity and context-dependent metastatic behavior (Haerinck and Berx 2021).

Consistent with clinical observations linking non-infiltrative HGPs to better prognosis (Proescholdt et al. 2025), the non-infiltrative 99LN and KPN models exhibited relatively low colonization indices (CI = 0.12–0.14), indicating reduced metastatic efficiency. In contrast, the infiltrative models exhibited more aggressive colonization profiles. Despite its partial EMT phenotype, CMT93Var demonstrated a low colonization index (CI = 0.054), indicating that MMPI infiltration does not necessarily equate to high metastatic competence. Conversely, E0771LG characterized by mesenchymal-like traits, exhibited rapid and aggressive parenchymal colonization (CI = 0.6), associated with early onset of clinical symptoms and reduced survival. Its elevated membrane-associated *Vim* expression likely contributes to its enhanced dissemination and infiltrative capacity (Huang et al. 2022).

Collectively, these data underscore the complexity of HGP-mediated metastatic progression and support the association of mesenchymal features with increased infiltration and poorer outcomes in BM. However, the findings also highlight that E/M status alone does not fully account for colonization efficiency, suggesting that additional molecular and microenvironmental factors are at play.

4.3. Distinct HGPs dictate the metastatic behaviour and cause of death

In this project, we employed the well-characterized diffuse infiltrative E0771LG model alongside the non-infiltrative TUBO model to investigate differences in early versus late stages of brain colonization. Remarkably, our results revealed that the HGP remains consistent over time, whether during early or late colonization phases, the growth pattern does not change.

However, the most critical finding of this investigation is that the HGP has a strong influence on the neurological cause of death. In the case of the infiltrative E0771LG model, mouse mortality was associated with intra-organ dissemination, as a secondary metastatic lesion developed, ultimately leading to death. In contrast, mice injected with the non-infiltrative TUBO model succumbed due to localized pressure effects, specifically in the right hemisphere of the brain, where tumor growth caused fatal compression of surrounding brain tissue.

These observations underscore the prognostic significance of the HGP in BM. This is the first study to demonstrate that distinct HGPs not only dictate metastatic behavior but also determine the underlying cause of mortality (Komljenovic et al. under revision).

4.4. The HGP at the MMPI determines the immune landscape

The HGP at the MMPI is thought to shape immune cell infiltration during BM and thereby influence the host's immune response and clinical outcome (Proescholdt et al. 2025). However, this concept has not been thoroughly validated in the literature. To examine the potential link between HGPs and immune infiltration, we analyzed key immune populations, including activated MG/BMDMs, astrocytes, and T cells, in BM derived from four selected BCBM and CCBM models.

The infiltrative models, CMT93Var and E0771LG, displayed robust immune infiltration across all cell types assessed. These models exhibited pronounced MG/BMDMs accumulation, particularly large aggregates of Iba1-positive cells within and surrounding the tumor mass. Similarly, T cells (Cd3-positive) were detected both at the MMPI and within the tumor core, with significantly higher presence compared to non-infiltrative models. They also showed high *Tgfß* expression pointing to a more immune suppressive microenvironment. Astrocyte activation, as well exhibited high infiltration not only confined to the MMPI, but also with evidence of astrocytic infiltration into the tumor core. These macroscopic findings were corroborated by increased gene expression of immune-specific markers, strongly linking infiltrative HGP with highly immune suppressed tumor microenvironments.

In contrast, the non-infiltrative models, 99LN and KPN, showed markedly limited immune cell presence. Only small clusters of activated MG/BMDMs were observed in the tumor core, with little to no Iba1-positive cell accumulation at the MMPI. Yet, both models exhibited a prominent glial capsule composed primarily of reactive astrocytes encasing the metastatic mass. This glial "pseudo-capsule" has been previously characterized by our group (Blazquez et al. 2020b) and is indicative of a displacement-based metastatic growth pattern. Notably, no Cd3-positive T cells were detected within the tumor core or at the MMPI in these models, reflecting an immunologically “deserted” landscape. This glial response at the MMPI in non-infiltrative models likely represents a coordinated defense mechanism of the CNS against infiltrating tumor cells.

Despite this barrier, MG and BMDMs presence at the brain-tumor interface in non-infiltrative models could paradoxically support metastatic survival, possibly contributing to immune evasion. Collectively, these findings highlight a clear association between the HGP and the extent of immune cell infiltration. When stratified by immune profile, models exhibiting infiltrative HGP showed high expression of immune-suppressive markers and were

predominantly classified as “altered-immune suppressed”. Conversely, models with non-infiltrative HGP correspond to “cold tumors,” lacking significant T cell infiltration (Galon and Bruni 2019).

Importantly, the immune-desert phenotype of cold tumors is associated with poor response to CIs (Bonaventura et al. 2019). While combination ICIs are more effective in tumors with high immune infiltration and immune suppression, the clinical challenge lies in converting cold tumors into immune-responsive states. However, the scarcity of reliable murine models of cold tumors has hindered the development of effective therapeutic strategies.

Remarkably, the 99LN and KPN models established in this study offer robust, syngeneic representations of cold tumors. These models provide a valuable platform to investigate mechanisms of immune exclusion and to test novel therapies aimed at promoting T cell infiltration, ultimately supporting efforts to reprogram immune-desert metastases into immunologically active, treatment-responsive tumors.

4.5. TREM2 as a critical regulator of macrophage lipid homeostasis

In the second major part of this work, examining TREM2 as a potential candidate of shielding during brain metastatic colonization and its role in macrophage morphology and function, we uncovered a particularly interesting finding. Upon activation of the TREM2 signaling pathway, specifically via its known ligand ApoE, we observed the emergence of a distinctive foamy phenotype in Trem2 KO BMDMs. This phenotype was not evident in WT cells but appeared exclusively in Trem2 KO BMDMs following ApoE stimulation. ApoE, an apolipoprotein involved in lipid transport, appears to drive lipid accumulation in these cells, leading to the formation of lipid-laden "foamy" macrophages. This phenotype was previously described by (Pang et al. 2024) in the context of Alzheimer’s disease, where TREM2 is known to exert a protective role.

TREM2 has been shown to facilitate the phagocytic clearance of amyloid-β plaques and myelin debris by microglia/macrophages. This function is mediated through mechanisms involving Liver X receptor (LXR) activation and ATP-binding cassette (ABC) transporters, which support cholesterol efflux. In the absence of TREM2, these pathways are disrupted, resulting in impaired cholesterol clearance and intracellular lipid buildup (Pang et al. 2024).

To elucidate the mechanism underlying the observed foamy phenotype, we analyzed different lipid classes, membrane, storage, and lysosomal, in WT and TREM2 KO BMDMs, both under control conditions and following ApoE or LPS stimulation. Consistent with our previous

findings, TREM2 KO BMDMs exhibited, across all conditions reduced free cholesterol (FC) in the membrane lipid fraction relative to total lipids, coupled with upregulation of phosphatidylcholine (PC) and downregulation of sphingomyelin (SM) upon ApoE and LPS stimulation.

This suggests disruptions in the membrane dynamics and cholesterol esterification processes, both of which are essential for lipid droplet biogenesis and the characteristic foamy macrophage phenotype, a process that typically involves macrophage uptake of modified lipoproteins, followed by ACAT-mediated esterification of free cholesterol and subsequent storage as cholesteryl esters in cytoplasmic lipid droplets (Wang et al. 2015).

Given the central role of mitochondria in lipid metabolism, we next investigated mitochondrial structure and function. Using MitoTracker Green, a fluorescent dye suitable for live-cell imaging, we observed a marked shift toward a punctate and fragmented mitochondrial morphology in Trem2 KO BMDMs (McQuade et al. 2020). In contrast, WT BMDMs displayed a more interconnected, network-like mitochondrial structure. Interestingly, electron microscopy (EM) did not reveal any significant morphological differences between genotypes in terms of mitochondrial area or number. This discrepancy may reflect functional or biochemical alterations, such as changes in mitochondrial protein content, redox state, or dynamics, that affect MitoTracker labeling which provides real-time visualization based on thiol reactivity in live cells, without altering the underlying membrane structure detectable by EM. Additionally, EM's limited sampling and fixation process may miss subtle or transient changes visible in live-cell imaging.

When we quantified mitochondrial content using MitoTracker Green and flow cytometry, we detected significantly reduced mitochondrial abundance in Trem2 KO BMDMs, especially following ApoE stimulation. We then assessed mitochondrial function by measuring oxygen consumption using the PreSens system. Oxygen consumption was consistently higher in Trem2 KO BMDMs, with the biggest difference observed under LPS stimulation. This observation contradicts previous reports of reduced mitochondrial respiration in TREM2 KO myeloid cells (Ulland and Colonna 2018) and instead suggests that these cells fail to undergo the expected glycolytic switch under inflammatory conditions, relying instead on mitochondrial respiration as a compensatory mechanism to meet metabolic demands, suggesting that loss of TREM2 imposes metabolic stress and drives compensatory overactivation of oxidative metabolism.

To evaluate mitochondrial membrane potential (MMP), we used JC-1 staining. Upon ApoE stimulation, Trem2 KO BMDMs exhibited significantly lower MMP compared to WT,

indicating mitochondrial dysfunction. However, under LPS stimulation, MMP levels were elevated in Trem2 KO cells, suggesting a stimulation-dependent variation in mitochondrial response.

Since mitochondria also play a key role in calcium homeostasis, we further analyzed both cytosolic and mitochondrial calcium levels. While basal cytosolic calcium remained unchanged across genotypes, mitochondrial calcium levels were significantly reduced in Trem2 KO BMDMs following both ApoE and LPS stimulation.

Collectively, our findings suggest that TREM2 is a critical regulator of lipid homeostasis in macrophages, facilitating lipid clearance and cholesterol efflux via LXR and ABC transporter pathways. Moreover, the absence of TREM2 results in pronounced mitochondrial dysfunction, reflected in altered mitochondrial morphology, reduced mitochondrial abundance, decreased membrane potential, and impaired calcium regulation. These insights further highlight the multifaceted role of TREM2 in maintaining macrophage metabolic health and functionality.

4.6. TREM2 does not affect tumor/macrophage dynamics *in vitro*

To investigate the role of TREM2 in macrophage function during tumor progression, we employed a range of *in vitro* approaches, focusing particularly on tumor–macrophage interactions. Our initial experiments involved establishing 3D spheroids using the hanging drop method. Tumor spheroids were formed from the four murine cancer cell lines (E0771LG, 99LN, CMT93Var, and KPN), each co-seeded with either WT or TREM2 KO BMDMs and were analyezed in the tumor spheroid formation phase.

Strikingly, tumor–macrophage interactions were not significantly altered by the loss of TREM2. Instead, the observed phenotypes appeared to correlate with the HGP of the respective tumor models. The diffusely infiltrative model E0771LG exhibited an inclusive phenotype, in which tumor cells and macrophages integrated uniformly into a single, well-organized 3D structure. In contrast, the CMT93Var model, representing an epithelial infiltrative growth pattern, displayed a more exclusive organization: macrophages remained largely confined to the periphery of the spheroid, showing minimal infiltartion into the tumor core.

The most striking phenotypes were observed with the non-infiltrative models, KPN and 99LN. In these cases, macrophages consistently segregated themselves from the tumor cells and formed distinct spheroids entirely separate from the tumor mass. We refer to this as a “separated” phenotype. Importantly, this segregation occurred regardless of TREM2

expression, indicating that the spatial organization of macrophages within the spheroids is driven by tumor-intrinsic factors linked to the HGP rather than by TREM2-dependent signaling.

To further assess whether TREM2 influences macrophage dynamics in a different context, we performed a co-culture migration assay. As seen in the spheroid assays, tumor–macrophage interactions varied depending on the tumor model. The E0771LG model again demonstrated strong chemoattraction, with macrophages migrating rapidly toward the tumor cells. In contrast, macrophage migration was notably restricted in the 99LN model, with tumor cells maintaining a clearly defined boundary that limited immune cell infiltration.

Consistent with the spheroid findings, TREM2 deficiency did not significantly affect macrophage migration in this experimental setup. Both WT and KO BMDMs exhibited similar migratory patterns, reinforcing the conclusion that TREM2 does not modulate tumor-directed macrophage migration *in vitro*. This observation contrats with a recent publication by (Cao et al. 2025), which described a pro-migratory role for TREM2 within the gastric cancer microenvironment.

Collectively, these data indicate that the functional impact of TREM2 is highly context-dependent and varies according to tumor type and experimental conditions. In our models, tumor HGP, not TREM2 expression, primarily governs the nature and extent of tumor–macrophage interaction and macrophage migratory behavior. These findings suggest that TREM2 does not play a major functional role in shaping macrophage–tumor dynamics *in vitro*.

4.7. TREM2 does not alter brain metastatic colonization *in vivo*

TREM2 is widely recognized in the literature for its dual role in immune suppression and tumor progression. Numerous studies have reported that anti-TREM2 therapies can lead to reduced tumor burden and improved outcomes (Binnewies et al. 2021; Molgora et al. 2020; Sun et al. 2023; Zhong et al. 2024). More recently, however, some studies have suggested a tumor-suppressive role for TREM2, where high expression levels were associated with better prognosis (Zhong et al. 2024). Conversely, other reports have found no significant benefit of TREM2 modulation on immune responses or survival outcomes (Peshoff et al. 2024; Zheng et al. 2023) (Table 21). This wide range of findings has contributed to ongoing controversy regarding the true functional role of TREM2 in cancer, prompting further investigation into the context-dependent factors that may influence its activity.

In our study, we utilized four syngeneic BM models, two derived from breast cancer cell lines (E0771LG and 99LN) and two from colon cancer cell lines (CMT93Var and KPN). Across all

four models, TREM2 depletion did not result in any significant differences in mouse survival, colonization index, or immune infiltration. Interestingly, the lack of effect was consistent regardless of whether the tumors developed in a relatively “cold” microenvironment with low immune activity or in a more immunosuppressed context. IHC analysis using Iba1 demonstrated comparable levels of macrophage and microglial infiltration in both WT and TREM2 KO mice, further supporting the idea that TREM2 is not essential for the recruitment or accumulation of these populations in BM. Similarly, neither Gfap staining for astrocytes nor Cd3 staining for T cells revealed any significant alterations in immune cell composition between WT and KO models.

In light of this, our findings suggest that, in contrast to prior assumptions, TREM2 signaling does not substantially influence the establishment of an immunosuppressive brain metastatic environment. Rather, its contribution to tumor progression appears to be context-dependent and not uniformly conserved across BM.

We propose that the function of TREM2 is likely dependent on several context-specific variables. These may include the specific tumor model used, the age of the mice, and the stage of metastatic colonization. Additionally, environmental factors such as microbiome composition, which can vary significantly between animal facilities, may also influence experimental outcomes and TREM2-related effects; which are not systematically recorded at all. As highlighted by (Rodriguez-Baena et al. 2025), MG and BMDMs, the primary cells expressing TREM2, exhibit high functional plasticity. They may play an immunosuppressive role during early stages of colonization, transitioning to a tumor-promoting phenotype during later stages. Therefore, these factors must be carefully considered when interpreting the role of TREM2 in metastatic progression. Thus, it could inhibit certain processes during extravasation and very early colonization, thereby supporting later colonization. However, this supportive function cannot be a clinically significant factor, as no relevant effect was measurable in OS in all four tested metastatic colonization models derived from two entities. In addition, these models differ in their HGP and immune composition, so that a wide range of metastatic models were part of this pre-clinical trial.

Taken together, these findings emphasize the need for careful consideration of experimental context when interpreting the role of TREM2 in tumor immunity and disease progression.

4.8. Future research prespectives

The role of TREM2 in the context of metastatic colonization and tumor progression remains highly controversial and unresolved. As previously discussed, TREM2 has been reported to exhibit dual, and sometimes conflicting functions, acting as either tumor-promoting, tumor-suppressive, or even functionally irrelevant depending on the experimental context. These inconsistencies highlight the need for a deeper investigation into the factors that modulate TREM2 function in view of a potential future translation into the clinic.

Our findings indicate a strong link between TREM2 and lipid metabolism, which in contrast to the colonization experiments, fits very well with the existing literature. Similar to the publications (McQuade et al. 2020; Pang et al. 2024; Ulland and Colonna 2018), we can describe that TREM2 plays an essential role in lipid shuttling and that this affects mitochondrial function. This raises new questions about how systemic metabolic states, such as those induced by a high-fat diet (HFD) (Pierro et al. 2024), might influence TREM2's role in tumor biology. It would be of great interest to design an experiment investigating tumor progression in mice subjected to an HFD. This could reveal whether TREM2's tumor-promoting or suppressive effects become more pronounced, or remain absent, under altered lipid metabolic conditions.

Moreover, future studies should aim to systematically analyze multiple influencing factors within the same experimental framework. This includes using various tumor models, different injection sites (e.g., intracardiac, intracranial, or orthotopic), and mice of different ages. Another critical but often overlooked variable is the microbiome, which can differ significantly across animal facilities and could profoundly influence immune cell behavior and thus TREM2 function (Yang et al. 2025).

It is also essential to distinguish between early and late stages of metastatic colonization when assessing TREM2's role. Macrophages, and particularly MG in the CNS, are highly plastic and may assume different phenotypes across the progression timeline (Rodriguez-Baena et al. 2025). This temporal plasticity could be key to understanding the divergent roles attributed to TREM2 across studies.

In summary, only by considering a broader spectrum of variables, including diet, tumor type, colonization stage, host age, and microbiome status, can we begin to unravel the true function of TREM2 in metastatic disease and immune regulation.

5. Summary and Conclusions

The prognostic value of infiltrative HGP at the MMPI highlights their relevance as a critical target in the fight against BM. To investigate the biological mechanisms underlying brain metastatic colonization, we utilized a panel of syngeneic BM models representing either infiltrative or displacing HGPs.

E0771LG and CMT93Var cell lines, previously established in our group, demonstrated infiltrative HGP at the MMPI, with moderate to high metastatic potential. These models were characterized by mesenchymal and partial EMT traits, respectively. In contrast, the KPN and 99LN models, both exhibiting displacing HGP at MMPI, were newly established as syngeneic BM models. KPN displayed epithelial characteristics with mesenchymal-like features, while 99LN showed more epithelial phenotype. Importantly, in line with previous reports associating displacing HGPs with better prognosis, our data revealed that these models also showed very low colonization capacity and reduced metastatic potential.

Furthermore, we demonstrated that the HGP remains consistent between early and late stages of colonization in both non-infiltrative (TUBO) and infiltrative (E0771LG) models. However, the clinical endpoint and disease progression differed markedly. In non-infiltrative models, death was primarily due to local pressure effects, such as compression of the right brain hemisphere. In contrast, infiltrative models showed widespread intra-organ dissemination, leading to secondary lesion formation, a more aggressive mode of progression.

Immune characterization of the brain-MME revealed a strong association between the HGPs and immune cell infiltration. Infiltrative HGP models were marked by enhanced immune infiltration within the tumor core and significant activation of macrophage and astrocyte populations. Conversely, displacing HGP models showed minimal T cell infiltration and lower overall immune cell presence, indicative of an immunologically “cold” or immune-excluded microenvironment.

Based on the degree of immune infiltration, our models were further categorized: KPN and 99LN represent novel “cold tumor” models, while E0771LG and CMT93Var represent “altered immune-suppressed” tumors. This classification offers valuable tools for future immunotherapy research, particularly for studying resistance to immune checkpoint inhibitors and strategies to convert “cold” tumors into “hot” immune-responsive phenotypes.

In parallel, we investigated the role of TREM2 in macrophage–tumor interactions. Contrary to some published findings, TREM2 disruption had no effect on tumor–macrophage interplay *in vitro* (spheroid formation assays), nor did it influence macrophage migration *in vitro* or *in vivo*. Importantly, TREM2 KO had no observable effect on HGP, survival, immune activation, or colonization potential across the four metastatic models (breast and colon origin). Thus, in our models, TREM2 did not influence brain colonization or progression, irrespective of the different HGPs.

Nevertheless, in line with previous findings TREM2 demonstrated a critical role in regulating lipid metabolism and mitochondrial function in BMDMs. TREM2 KO led to a foamy macrophage phenotype, characterized by lipid accumulation, altered mitochondrial morphology (more punctate/fragmented), decreased mitochondrial quantity, and lower mitochondrial membrane potential. Furthermore, TREM2 deficiency disrupted calcium homeostasis, particularly in mitochondrial calcium uptake, further confirming mitochondrial dysfunction.

Taken together, our findings support a model in which HGPs serve as powerful prognostic markers of disease progression, immune exclusion, and therapeutic resistance in BM. These patterns may serve as future diagnostic markers and therapeutic targets. Additionally, while TREM2 did not modulate metastatic colonization or immune infiltration in the brain in our models, it plays a vital role in macrophage lipid homeostasis and mitochondrial health (Table 22 and Figure 29). This work provides new insights into both the tumor–immune interface in BM and TREM2's role in the metabolic regulation of macrophages.

Table 22. Summary of tumor model characteristics and macrophage phenotypes in WT and TREM2 KO.

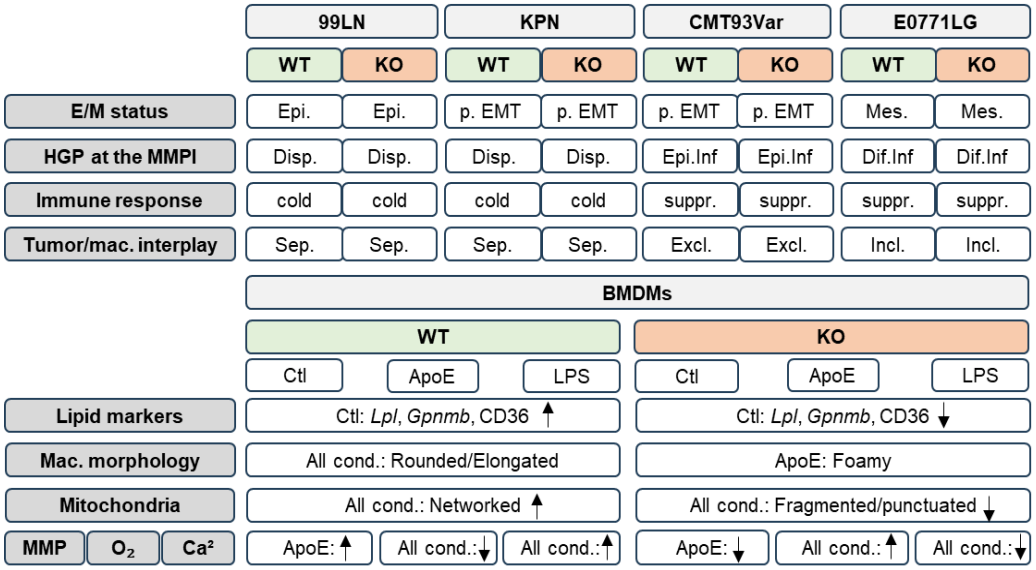

The upper panel compares four tumor models (99LN, KPN, CMT93Var, E0771LG) in WT and TREM2 KO settings with respect to epithelial/mesenchymal (E/M) status (epithelial, mesenchymal or partial EMT), HGPs at the MMPI (displacing, epithelial infiltrative or diffuse infiltrative), immune response (cold or immune suppressed), and tumor–macrophage interplay (separated, exclusive or inclusive). These parameters were largely comparable between WT and TREM2 KO tumors within each model. The lower panel summarizes BMDMs phenotypes under control (Ctl), ApoE, and LPS stimulation. WT BMDMs showed higher expression of lipid-associated markers (*Lpl*, *Gpnmb*, CD36), rounded/elongated morphology, and networked mitochondria across conditions. In contrast, TREM2 KO BMDMs exhibited reduced lipid marker expression, a foamy morphology (most evident upon ApoE stimulation), fragmented/punctuated mitochondrial networks, and consistent alterations in mitochondrial membrane potential (MMP), oxygen levels (O_2), and Ca^{2+} handling across all stimulation conditions.

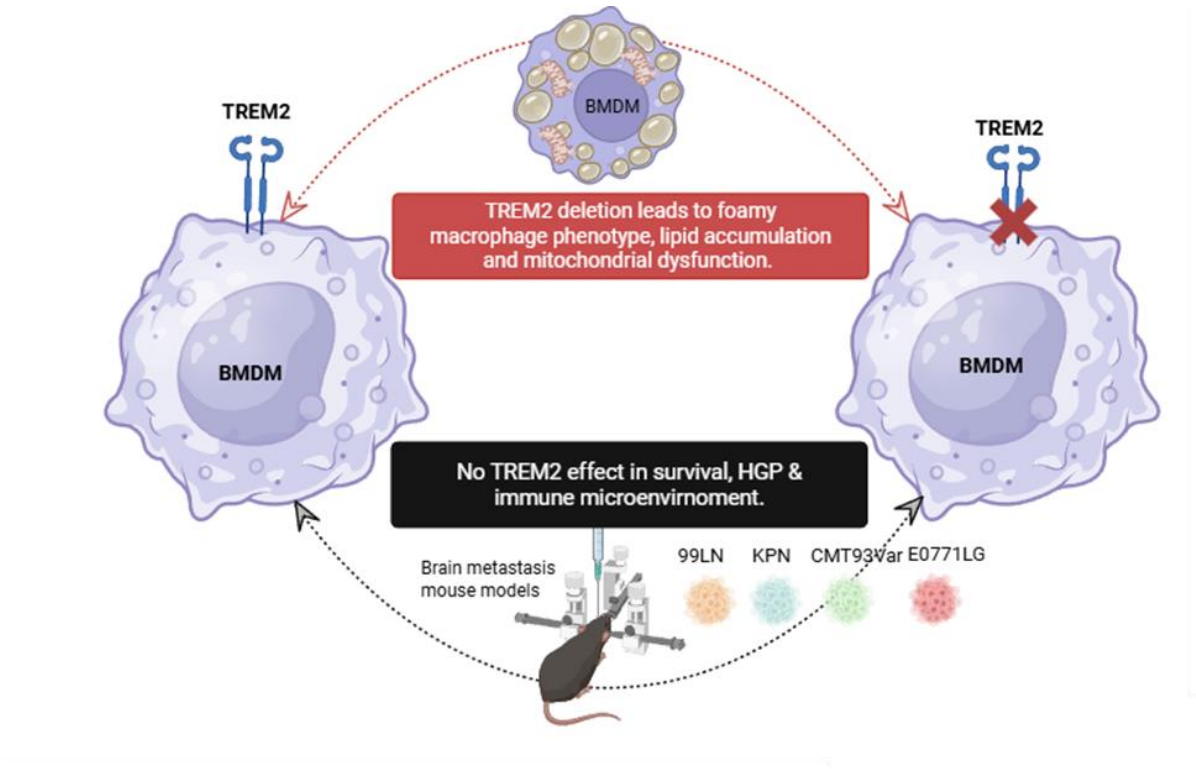

Figure 29. Schematic illustration summarizing TREM2's effect on BMDMs and BM mouse models.

Schematic overview illustrating the impact of TREM2 on BMDMs. Loss of TREM2 induces a foamy macrophage phenotype characterized by lipid accumulation. TREM2 deficiency does not affect overall survival, HGP, or the immune microenvironment in BM mouse models. Findings are consistent across multiple BM mouse models (99LN, KPN, CMT93Var, and E0771LG). Image created with Biorender.com.

6. Appendix

6.1. List of Tables

6.2. List of Figures

6.3. Abbreviations

ACAT1	acetyl-CoA acetyltransferase 1
AD	alzheimer's disease
ANOVA	analysis of variance
ApoE	apolipoprotein E
BBB	blood-brain barrier
BBM	blood-brain metastasis barrier
BCBM	breast cancer brain metastasis
BF	bright field
BM	brain metastasis
BMDM	bone marrow-derived macrophages
BSA	bovine serum albumin
BSO	buthionine sulfoximine
Ca2+	calcium
CCBM	colon cancer brain metastasis
Cd3	cluster of differentiation 3
CE	cholesteryl ester
Cer	ceramide
CI	colonization index
Ck19	cytokeratin-19
Ck8	cytokeratin-8
CL	cardiolipin
CNS	central nervous system
CSF1R	colony-stimulating factor 1 receptor
Ctl	control
CTL4	cytotoxic T-lymphocyte antigen 4
DAB	diaminobenzidine
DAM	disease-associated microglia
DAMPs	damage-associated molecular patterns
DAP12/10	dnax-activating protein of 12 kDa/10kDa
ddH2O	double-distilled water
DEG	differentially expressed gene
dH2O	distilled water
DMEM	Dulbecco's modified Eagle medium
DMPE	Dimethylphosphatidylethanolamine
DMSO	dimethyl sulfoxide

Ecad	E-cadherin
ECM	extracellular matrix
EDTA	ethylenediaminetetraacetic acid
E/M	epithelial/mesenchymal
EM	electron microscope
EMT	epithelial-mesenchymal transition
EtOH	ethanol
ERK1/2	extracellular signal-regulated kinase 1/2
FACS	fluorescence-activated cell sorter
FC	Free cholesterol
FCS	fetal calf serum
FITC	fluorescein isothiocyanate
FFPE	formalin-fixed paraffin-embedded
Gfap	glial fibrillary acidic protein
GOI	gene of interest
HER2	human epidermal growth factor receptor 2
HexCer	hexosylceramide
HFD	high-fat diet
HGP	histological growth pattern
HK	housekeeping gene
Iba1	allograft inflammatory factor 1
ICIs	Immune checkpoint inhibitors
IF	immunofluorescence
IHC	immunohistochemistry
ITAM	immunoreceptor tyrosine-based activation motif
JC-1	5',6,6'-tetrachloro-1,1',3,3'-tetraethylbenzimidazolylcarbocyanineiodide
KO	knockout
LPC	lysophosphatidylcholine
LPE	lysophosphatidylethanolamine
LPS	lipopolysaccharide
LXR	liver x receptor
MAPK	mitogen-activated protein kinase
MG	microglia
MME	metastatic microenvironment
MMP	mitochondrial membrane potential
MMPE	Monomethylphosphatidylethanolamine
MMPI	macro-metastasis/organ parenchyma interface

MRI	Magnetic resonance imaging
MSI-H/dMMR	microsatellite instability-high / deficient mismatch repair
mRNA	messenger RNA
n.s.	not significant
OS	overall survival
oxCE	oxidized CE
PA	phosphatidic acid
PBS	phosphate buffered saline
PC	phosphatidylcholine
PC O	phosphatidylcholine-ether
PE	phosphatidylethanolamine
PE P	PE based plasmalogen
PG	phosphatidylglycerol
PI	phosphatidylinositol
PI3K	phosphoinositide 3-kinase
PFA	paraformaldehyde
PLCγ	phospholipase Cγ
PS	phosphatidylserine
qRT-PCR	quantitative real-time polymerase chain reaction
RNA	ribonucleic acid
ROI	region of interest
SDS	sodium dodecyl sulfate
SM	sphingomyelin
SYK	spleen tyrosine kinase
TAMs	tumor-associated macrophages
TG	Triglyceride
TGF-β	transforming growth factor-β
TME	tumor microenvironment
TREM2	triggering receptor expressed on myeloid cells 2
TRITC	tetramethylrhodamine
qRT PCR	quantitative real-time PCR
Vim	vimentin
WT	wildtype

Measurement units:

bp	base pairs
°C	degree Celsius
g	gram
g	relative centrifugal force
h	hour
l	liter
m	meter
M	Molar
min	minute
n	number
n	sample size
rpm	revolutions per minute
s	second

Metric prefixes:

c	centi (10^{-2})
m	milli (10^{-3})
µ	micro (10^{-6})
n	nano (10^{-9})

7. Bibliography

Achrol, Achal Singh; Rennert, Robert C.; Anders, Carey; Soffietti, Riccardo; Ahluwalia, Manmeet S.; Nayak, Lakshmi et al. (2019): Brain metastases. In: *Nature reviews. Disease primers* 5 (1), S. 5. DOI: 10.1038/s41572-018-0055-y.

Alves de Lima J, Pukrop T, Blazquez R: Modelling Brain Metastasis: Standardized analysis of metastatic colonization and histological growth patterns by stereotactic intracortical injection J Vis Exp. (accepted).

Binnewies, Mikhail; Pollack, Joshua L.; Rudolph, Joshua; Dash, Subhadra; Abushawish, Marwan; Lee, Tian et al. (2021): Targeting TREM2 on tumor-associated macrophages enhances immunotherapy. In: *Cell reports* 37 (3), S. 109844. DOI: 10.1016/j.celrep.2021.109844.

Blazquez, R.; Sparrer, D.; Wendl, C.; Evert, M.; Riemenschneider, M. J.; Krahn, M. P. et al. (2020a): The macro-metastasis/organ parenchyma interface (MMPI) - A hitherto unnoticed area. In: *Seminars in cancer biology* 60, S. 324–333. DOI: 10.1016/j.semcancer.2019.10.012.

Blazquez, Raquel; Rietkötter, Eva; Wenske, Britta; Wlochowitz, Darius; Sparrer, Daniela; Vollmer, Elena et al. (2020b): LEF1 supports metastatic brain colonization by regulating glutathione metabolism and increasing ROS resistance in breast cancer. In: *International journal of cancer* 146 (11), S. 3170–3183. DOI: 10.1002/ijc.32742.

BLIGH, E. G.; DYER, W. J. (1959): A rapid method of total lipid extraction and purification. In: *Canadian journal of biochemistry and physiology* 37 (8), S. 911–917. DOI: 10.1139/o59-099.

Bonaventura, Paola; Shekarian, Tala; Alcazer, Vincent; Valladeau-Guilemond, Jenny; Valsesia-Wittmann, Sandrine; Amigorena, Sebastian et al. (2019): Cold Tumors: A Therapeutic Challenge for Immunotherapy. In: *Frontiers in immunology* 10, S. 168. DOI: 10.3389/fimmu.2019.00168.

Bowman, Robert L.; Klemm, Florian; Akkari, Leila; Pyonteck, Stephanie M.; Sevenich, Lisa; Quail, Daniela F. et al. (2016): Macrophage Ontogeny Underlies Differences in Tumor-Specific Education in Brain Malignancies. In: *Cell reports* 17 (9), S. 2445–2459. DOI: 10.1016/j.celrep.2016.10.052.

Bravo-Sagua, Roberto; Parra, Valentina; López-Crisosto, Camila; Díaz, Paula; Quest, Andrew F. G.; Lavandero, Sergio (2017): Calcium Transport and Signaling in Mitochondria. In: *Comprehensive Physiology* 7 (2), S. 623–634. DOI: 10.1002/cphy.c160013.

Bruni, Daniela; Angell, Helen K.; Galon, Jérôme (2020): The immune contexture and Immunoscore in cancer prognosis and therapeutic efficacy. In: *Nature reviews. Cancer* 20 (11), S. 662–680. DOI: 10.1038/s41568-020-0285-7.

Cacho-Díaz, Bernardo; García-Botello, Donovan R.; Wegman-Ostrosky, Talia; Reyes-Soto, Gervith; Ortiz-Sánchez, Elizabeth; Herrera-Montalvo, Luis Alonso (2020): Tumor microenvironment differences between primary tumor and brain metastases. In: *Journal of translational medicine* 18 (1), S. 1. DOI: 10.1186/s12967-019-02189-8.

Cao, Qianqian; Sun, Dianshui; Tu, Can; Wang, Jihua; Fu, Runjia; Gong, Rumei et al. (2025): Defining gastric cancer ecology: the crucial roles of TREM2+ macrophages and fibroblasts in

tumor microenvironments. In: *Communications biology* 8 (1), S. 514. DOI: 10.1038/s42003-025-07512-2.

Chamberlain, Marc C.; Baik, Christina S.; Gadi, Vijayakrishna K.; Bhatia, Shailender; Chow, Laura Q. M. (2017): Systemic therapy of brain metastases: non-small cell lung cancer, breast cancer, and melanoma. In: *Neuro-oncology* 19 (1), i1-i24. DOI: 10.1093/neuonc/now197.

Collison, Joanna (2019): Synovial macrophages shield the joints. In: *Nature reviews. Rheumatology* 15 (10), S. 573. DOI: 10.1038/s41584-019-0295-6.

Colonna, Marco; Wang, Yaming (2016): TREM2 variants: new keys to decipher Alzheimer disease pathogenesis. In: *Nature reviews. Neuroscience* 17 (4), S. 201–207. DOI: 10.1038/nrn.2016.7.

Cortes, Javier; Cescon, David W.; Rugo, Hope S.; Nowecki, Zbigniew; Im, Seock-Ah; Yusof, Mastura Md et al. (2020): Pembrolizumab plus chemotherapy versus placebo plus chemotherapy for previously untreated locally recurrent inoperable or metastatic triple-negative breast cancer (KEYNOTE-355): a randomised, placebo-controlled, double-blind, phase 3 clinical trial. In: *Lancet (London, England)* 396 (10265), S. 1817–1828. DOI: 10.1016/S0140-6736(20)32531-9.

Cotechini, Tiziana; Atallah, Aline; Grossman, Arielle (2021): Tissue-Resident and Recruited Macrophages in Primary Tumor and Metastatic Microenvironments: Potential Targets in Cancer Therapy. In: *Cells* 10 (4). DOI: 10.3390/cells10040960.

Culemann, Stephan; Grüneboom, Anika; Nicolás-Ávila, José Ángel; Weidner, Daniela; Lämmle, Katrin Franziska; Rothe, Tobias et al. (2019): Locally renewing resident synovial macrophages provide a protective barrier for the joint. In: *Nature* 572 (7771), S. 670–675. DOI: 10.1038/s41586-019-1471-1.

Damisah, Eyiyemisi C.; Rai, Anupama; Grutzendler, Jaime (2020): TREM2: Modulator of Lipid Metabolism in Microglia. In: *Neuron* 105 (5), S. 759–761. DOI: 10.1016/j.neuron.2020.02.008.

Deczkowska, Aleksandra; Weiner, Assaf; Amit, Ido (2020): The Physiology, Pathology, and Potential Therapeutic Applications of the TREM2 Signaling Pathway. In: *Cell* 181 (6), S. 1207–1217. DOI: 10.1016/j.cell.2020.05.003.

Dong, Zhiwei; Shanmughapriya, Santhanam; Tomar, Dhanendra; Siddiqui, Naveed; Lynch, Solomon; Nemani, Neeharika et al. (2017): Mitochondrial Ca2+ Uniporter Is a Mitochondrial Luminal Redox Sensor that Augments MCU Channel Activity. In: *Molecular cell* 65 (6), 1014-1028.e7. DOI: 10.1016/j.molcel.2017.01.032.

Doron, Hila; Pukrop, Tobias; Erez, Neta (2019): A Blazing Landscape: Neuroinflammation Shapes Brain Metastasis. In: *Cancer research* 79 (3), S. 423–436. DOI: 10.1158/0008-5472.CAN-18-1805.

Er, Ekrem Emrah; Valiente, Manuel; Ganesh, Karuna; Zou, Yilong; Agrawal, Saloni; Hu, Jing et al. (2018): Pericyte-like spreading by disseminated cancer cells activates YAP and MRTF for metastatic colonization. In: *Nature cell biology* 20 (8), S. 966–978. DOI: 10.1038/s41556-018-0138-8.

Fang, Chao; Zhong, Rui; Lu, Shuai; Yu, Gang; Liu, Zhilin; Yan, Chengyuan et al. (2024): TREM2 promotes macrophage polarization from M1 to M2 and suppresses osteoarthritis

through the NF-κB/CXCL3 axis. In: *International journal of biological sciences* 20 (6), S. 1992–2007. DOI: 10.7150/ijbs.91519.

Franks, L. M.; Hemmings, V. J. (1978): A cell line from an induced carcinoma of mouse rectum. In: *The Journal of pathology* 124 (1), S. 35–38. DOI: 10.1002/path.1711240108.

Galon, Jérôme; Bruni, Daniela (2019): Approaches to treat immune hot, altered and cold tumours with combination immunotherapies. In: *Nature reviews. Drug discovery* 18 (3), S. 197–218. DOI: 10.1038/s41573-018-0007-y.

Gofrit, Ofer N.; Gofrit, Ben; Roditi, Yuval; Popovtzer, Aron; Frank, Steve; Sosna, Jacob; Goldberg, S. Nahum (2022): Patterns of metastases progression- The linear parallel ratio. In: *PloS one* 17 (9), e0274942. DOI: 10.1371/journal.pone.0274942.

Guerreiro, Rita; Wojtas, Aleksandra; Bras, Jose; Carrasquillo, Minerva; Rogaeva, Ekaterina; Majounie, Elisa et al. (2013): TREM2 variants in Alzheimer's disease. In: *The New England journal of medicine* 368 (2), S. 117–127. DOI: 10.1056/NEJMoa1211851.

Guo, Hanrui; Wang, Meiling; Ni, Caiya; Yang, Chun; Fu, Chunxue; Zhang, Xiaoman et al. (2025): TREM2 promotes the formation of a tumor-supportive microenvironment in hepatocellular carcinoma. In: *Journal of experimental & clinical cancer research : CR* 44 (1), S. 20. DOI: 10.1186/s13046-025-03287-w.

Haerinck, Jef; Berx, Geert (2021): Partial EMT takes the lead in cancer metastasis. In: *Developmental cell* 56 (23), S. 3174–3176. DOI: 10.1016/j.devcel.2021.11.012.

Huang, Yuhe; Hong, Weiqi; Wei, Xiawei (2022): The molecular mechanisms and therapeutic strategies of EMT in tumor progression and metastasis. In: *Journal of hematology & oncology* 15 (1), S. 129. DOI: 10.1186/s13045-022-01347-8.

Huang, Yu-Kuan; Busuttil, Rita A.; Boussioutas, Alex (2021): The Role of Innate Immune Cells in Tumor Invasion and Metastasis. In: *Cancers* 13 (23). DOI: 10.3390/cancers13235885.

Jackstadt, Rene; van Hooff, Sander R.; Leach, Joshua D.; Cortes-Lavaud, Xabier; Lohuis, Jeroen O.; Ridgway, Rachel A. et al. (2019): Epithelial NOTCH Signaling Rewires the Tumor Microenvironment of Colorectal Cancer to Drive Poor-Prognosis Subtypes and Metastasis. In: *Cancer cell* 36 (3), 319-336.e7. DOI: 10.1016/j.ccell.2019.08.003.

Jaitin, Diego Adhemar; Adlung, Lorenz; Thaiss, Christoph A.; Weiner, Assaf; Li, Baoguo; Descamps, Hélène et al. (2019): Lipid-Associated Macrophages Control Metabolic Homeostasis in a Trem2-Dependent Manner. In: *Cell* 178 (3), 686-698.e14. DOI: 10.1016/j.cell.2019.05.054.

Kitamura, Takanori; Kato, Yu; Brownlie, Demi; Soong, Daniel Y. H.; Sugano, Gaël; Kippen, Nicolle et al. (2019): Mammary Tumor Cells with High Metastatic Potential Are Hypersensitive to Macrophage-Derived HGF. In: *Cancer immunology research* 7 (12), S. 2052–2064. DOI: 10.1158/2326-6066.CIR-19-0234.

Klemm, Florian; Maas, Roeltje R.; Bowman, Robert L.; Kornete, Mara; Soukup, Klara; Nassiri, Sina et al. (2020): Interrogation of the Microenvironmental Landscape in Brain Tumors Reveals Disease-Specific Alterations of Immune Cells. In: *Cell* 181 (7), 1643-1660.e17. DOI: 10.1016/j.cell.2020.05.007.

Klemm, Florian; Möckl, Aylin; Salamero-Boix, Anna; Alekseeva, Tijna; Schäffer, Alexander; Schulz, Michael et al. (2021): Compensatory CSF2-driven macrophage activation promotes

adaptive resistance to CSF1R inhibition in breast-to-brain metastasis. In: *Nature cancer* 2 (10), S. 1086–1101. DOI: 10.1038/s43018-021-00254-0.

Komljenovic D, Bäuerle T, Alves de Lima J, Trigueros-López L, Dietz C, Winter Z, Araceli T, Strotzer Q, Wendl C, Brendel M, Proescholdt M, Evert K, Pukrop T, Blazquez R: Intracranial pressure or whole brain destruction: two causes of neurological death explained by fundamentally different metastatic colonization patterns (under revision).

Li, Shangbiao; Shen, Yuchen; Dong, Chengtao; Yin, Shengqi; Zhou, Dong; Zhou, Aidong (2025): The molecular and immune microenvironmental landscape of brain metastases: Implications for novel treatment options. In: *Cell Investigation* 1 (1), S. 100005. DOI: 10.1016/j.clnves.2024.100005.

Li, Ya; Zhang, Huhu; Yu, Chunjuan; Dong, Xiaolei; Yang, Fanghao; Wang, Mengjun et al. (2024): New Insights into Mitochondria in Health and Diseases. In: *International journal of molecular sciences* 25 (18). DOI: 10.3390/ijms25189975.

Li, Yueran; Xu, Huifang; Wang, Huifang; Yang, Kui; Luan, Jiajie; Wang, Sheng (2023): TREM2: Potential therapeutic targeting of microglia for Alzheimer's disease. In: *Biomedicine & pharmacotherapy = Biomedecine & pharmacotherapie* 165, S. 115218. DOI: 10.1016/j.biopha.2023.115218.

Liebisch, Gerhard; Lieser, Bernd; Rathenberg, Jan; Drobnik, Wolfgang; Schmitz, Gerd (2004): High-throughput quantification of phosphatidylcholine and sphingomyelin by electrospray ionization tandem mass spectrometry coupled with isotope correction algorithm. In: *Biochimica et biophysica acta* 1686 (1-2), S. 108–117. DOI: 10.1016/j.bbalip.2004.09.003.

Massagué, Joan; Obenauf, Anna C. (2016): Metastatic colonization by circulating tumour cells. In: *Nature* 529 (7586), S. 298–306. DOI: 10.1038/nature17038.

McQuade, Amanda; Kang, You Jung; Hasselmann, Jonathan; Jairaman, Amit; Sotelo, Alexandra; Coburn, Morgan et al. (2020): Gene expression and functional deficits underlie TREM2-knockout microglia responses in human models of Alzheimer's disease. In: *Nature communications* 11 (1), S. 5370. DOI: 10.1038/s41467-020-19227-5.

Menzyanova, Natalia G.; Pyatina, Svetlana A.; Shabanov, Alexander V.; Nemtsev, Ivan V.; Stolyarov, Dmitry P.; Dryganov, Dmitry B. et al. (2019): The Morphology and Phenotype of Monocyte-Macrophages When Cultured on Bionanofilms Substrates with Different Surface Relief Profiles. In: *Biomolecules* 10 (1). DOI: 10.3390/biom10010065.

Molgora, Martina; Esaulova, Ekaterina; Vermi, William; Hou, Jinchao; Chen, Yun; Luo, Jingqin et al. (2020): TREM2 Modulation Remodels the Tumor Myeloid Landscape Enhancing Anti-PD-1 Immunotherapy. In: *Cell* 182 (4), 886-900.e17. DOI: 10.1016/j.cell.2020.07.013.

Nakamura, Kyohei; Smyth, Mark J. (2020): TREM2 marks tumor-associated macrophages. In: *Signal transduction and targeted therapy* 5 (1), S. 233. DOI: 10.1038/s41392-020-00356-8.

Neikirk, Kit; Marshall, Andrea G.; Kula, Bartosz; Smith, Nathan; LeBlanc, Sharonda; Hinton, Antentor (2023): MitoTracker: A useful tool in need of better alternatives. In: *European journal of cell biology* 102 (4), S. 151371. DOI: 10.1016/j.ejcb.2023.151371.

Novikov, Nikita M.; Zolotaryova, Sofia Y.; Gautreau, Alexis M.; Denisov, Evgeny V. (2021): Mutational drivers of cancer cell migration and invasion. In: *British journal of cancer* 124 (1), S. 102–114. DOI: 10.1038/s41416-020-01149-0.

Nugent, Alicia A.; Lin, Karin; van Lengerich, Bettina; Lianoglou, Steve; Przybyla, Laralynne; Davis, Sonnet S. et al. (2020): TREM2 Regulates Microglial Cholesterol Metabolism upon Chronic Phagocytic Challenge. In: *Neuron* 105 (5), 837-854.e9. DOI: 10.1016/j.neuron.2019.12.007.

Overman, Michael J.; Lonardi, Sara; Wong, Ka Yeung Mark; Lenz, Heinz-Josef; Gelsomino, Fabio; Aglietta, Massimo et al. (2018): Durable Clinical Benefit With Nivolumab Plus Ipilimumab in DNA Mismatch Repair-Deficient/Microsatellite Instability-High Metastatic Colorectal Cancer. In: *Journal of clinical oncology : official journal of the American Society of Clinical Oncology* 36 (8), S. 773–779. DOI: 10.1200/JCO.2017.76.9901.

Pang, Lizhi; Zhou, Fei; Chen, Peiwen (2024): Lipid-Laden Macrophages Recycle Myelin to Feed Glioblastoma. In: *Cancer research* 84 (22), S. 3712–3714. DOI: 10.1158/0008-5472.CAN-24-3362.

Peshoff, Mekenzie M.; Gupta, Pravesh; Oberai, Shivangi; Trivedi, Rakesh; Katayama, Hiroshi; Chakrapani, Prashanth et al. (2024): Triggering receptor expressed on myeloid cells 2 (TREM2) regulates phagocytosis in glioblastoma. In: *Neuro-oncology* 26 (5), S. 826–839. DOI: 10.1093/neuonc/noad257.

Pierro, Elysa W.; Cottam, Matthew A.; An, Hanbing; Lehmann, Brian D.; Pietenpol, Jennifer A.; Wellen, Kathryn E. et al. (2024): Trem2 deficiency attenuates breast cancer tumor growth in lean, but not obese or weight loss, mice and is associated with alterations of clonal T cell populations. In: *bioRxiv : the preprint server for biology*. DOI: 10.1101/2024.09.25.614811.

Proescholdt, Martin A.; Araceli, Tommaso; Schebesch, Karl-Michael; Doenitz, Christian; Wendl, Christina; Evert, Katja et al. (2025): MetInfilt: A prospective trial highlighting the importance of the histological growth pattern in brain metastases. In: *Translational oncology* 60, S. 102480. DOI: 10.1016/j.tranon.2025.102480.

Quail, Daniela F.; Joyce, Johanna A. (2017): The Microenvironmental Landscape of Brain Tumors. In: *Cancer cell* 31 (3), S. 326–341. DOI: 10.1016/j.ccell.2017.02.009.

Reiling, N.; Klug, K.; Krallmann-Wenzel, U.; Laves, R.; Goyert, S.; Taylor, M. E. et al. (2001): Complex encounters at the macrophage-mycobacterium interface: studies on the role of the mannose receptor and CD14 in experimental infection models with Mycobacterium avium. In: *Immunobiology* 204 (5), S. 558–571. DOI: 10.1078/0171-2985-00093.

Rodriguez-Baena, Francisco Javier; Marquez-Galera, Angel; Ballesteros-Martinez, Pablo; Castillo, Alba; Diaz, Eva; Moreno-Bueno, Gema et al. (2025): Microglial reprogramming enhances antitumor immunity and immunotherapy response in melanoma brain metastases. In: *Cancer cell* 43 (3), 413-427.e9. DOI: 10.1016/j.ccell.2025.01.008.

Saitoh, Masao (2018): Involvement of partial EMT in cancer progression. In: *Journal of biochemistry* 164 (4), S. 257–264. DOI: 10.1093/jb/mvy047.

Schreurs, Luca D.; vom Stein, Alexander F.; Jünger, Stephanie T.; Timmer, Marco; Noh, Ka-Won; Buettner, Reinhard et al. (2025): The immune landscape in brain metastasis. In: *Neuro-oncology* 27 (1), S. 50–62. DOI: 10.1093/neuonc/noae219.

Schulz, Michael; Sevenich, Lisa (2021): TAMs in Brain Metastasis: Molecular Signatures in Mouse and Man. In: *Frontiers in immunology* 12, S. 716504. DOI: 10.3389/fimmu.2021.716504.

Siam, Laila; Bleckmann, Annalen; Chaung, Han-Ning; Mohr, Alexander; Klemm, Florian; Barrantes-Freer, Alonso et al. (2015): The metastatic infiltration at the metastasis/brain parenchyma-interface is very heterogeneous and has a significant impact on survival in a prospective study. In: *Oncotarget* 6 (30), S. 29254–29267. DOI: 10.18632/oncotarget.4201.

Sivandzade, Farzane; Bhalerao, Aditya; Cucullo, Luca (2019): Analysis of the Mitochondrial Membrane Potential Using the Cationic JC-1 Dye as a Sensitive Fluorescent Probe. In: *Bio-protocol* 9 (1). DOI: 10.21769/BioProtoc.3128.

Solomou, Georgios; Young, Adam M. H.; Bulstrode, Harry J. C. J. (2024): Microglia and macrophages in glioblastoma: landscapes and treatment directions. In: *Molecular oncology* 18 (12), S. 2906–2926. DOI: 10.1002/1878-0261.13657.

Sultan, Ahmed S.; Vila, Taissa; Hefni, Eman; Karlsson, Amy J.; Jabra-Rizk, Mary Ann (2019): Evaluation of the Antifungal and Wound-Healing Properties of a Novel Peptide-Based Bioadhesive Hydrogel Formulation. In: *Antimicrobial agents and chemotherapy* 63 (10). DOI: 10.1128/AAC.00888-19.

Sun, Rui; Han, Rowland; McCornack, Colin; Khan, Saad; Tabor, G. Travis; Chen, Yun et al. (2023): TREM2 inhibition triggers antitumor cell activity of myeloid cells in glioblastoma. In: *Science advances* 9 (19), eade3559. DOI: 10.1126/sciadv.ade3559.

Ulland, Tyler K.; Colonna, Marco (2018): TREM2 - a key player in microglial biology and Alzheimer disease. In: *Nature reviews. Neurology* 14 (11), S. 667–675. DOI: 10.1038/s41582-018-0072-1.

Ulland, Tyler K.; Song, Wilbur M.; Huang, Stanley Ching-Cheng; Ulrich, Jason D.; Sergushichev, Alexey; Beatty, Wandy L. et al. (2017): TREM2 Maintains Microglial Metabolic Fitness in Alzheimer's Disease. In: *Cell* 170 (4), 649-663.e13. DOI: 10.1016/j.cell.2017.07.023.

Ulrich, Jason D.; Ulland, Tyler K.; Colonna, Marco; Holtzman, David M. (2017): Elucidating the Role of TREM2 in Alzheimer's Disease. In: *Neuron* 94 (2), S. 237–248. DOI: 10.1016/j.neuron.2017.02.042.

Valiente, Manuel; Ahluwalia, Manmeet S.; Boire, Adrienne; Brastianos, Priscilla K.; Goldberg, Sarah B.; Lee, Eudocia Q. et al. (2018): The Evolving Landscape of Brain Metastasis. In: *Trends in cancer* 4 (3), S. 176–196. DOI: 10.1016/j.trecan.2018.01.003.

van Lengerich, Bettina; Zhan, Lihong; Xia, Dan; Chan, Darren; Joy, David; Park, Joshua I. et al. (2023): A TREM2-activating antibody with a blood-brain barrier transport vehicle enhances microglial metabolism in Alzheimer's disease models. In: *Nature neuroscience* 26 (3), S. 416–429. DOI: 10.1038/s41593-022-01240-0.

Wang, Xinxin; Wang, Yunhan; Yang, Lei; Zhang, Yi; Yang, Li (2025): TREM2+ macrophages: a key role in disease development. In: *Frontiers in immunology* 16, S. 1550893. DOI: 10.3389/fimmu.2025.1550893.

Wang, Yaming; Cella, Marina; Mallinson, Kaitlin; Ulrich, Jason D.; Young, Katherine L.; Robinette, Michelle L. et al. (2015): TREM2 lipid sensing sustains the microglial response in an Alzheimer's disease model. In: *Cell* 160 (6), S. 1061–1071. DOI: 10.1016/j.cell.2015.01.049.

Wu, Alex Man Lai; Gossa, Selamawit; Samala, Ramakrishna; Chung, Monika A.; Gril, Brunilde; Yang, Howard H. et al. (2021): Aging and CNS Myeloid Cell Depletion Attenuate Breast Cancer Brain Metastasis. In: *Clinical cancer research : an official journal of the*

American Association for Cancer Research 27 (15), S. 4422–4434. DOI: 10.1158/1078-0432.CCR-21-1549.

Xing, Fei; Kobayashi, Aya; Okuda, Hiroshi; Watabe, Misako; Pai, Sudha K.; Pandey, Puspa R. et al. (2013): Reactive astrocytes promote the metastatic growth of breast cancer stem-like cells by activating Notch signalling in brain. In: *EMBO molecular medicine* 5 (3), S. 384–396. DOI: 10.1002/emmm.201201623.

Yang, Daowei; Sun, Xinlei; Wang, Hua; Wistuba, Ignacio I.; Wang, Huamin; Maitra, Anirban; Chen, Yang (2025): TREM2 Depletion in Pancreatic Cancer Elicits Pathogenic Inflammation and Accelerates Tumor Progression via Enriching IL-1β+ Macrophages. In: *Gastroenterology* 168 (6), S. 1153–1169. DOI: 10.1053/j.gastro.2025.01.244.

Yang, Jing; Antin, Parker; Berx, Geert; Blanpain, Cédric; Brabletz, Thomas; Bronner, Marianne et al. (2020): Guidelines and definitions for research on epithelial-mesenchymal transition. In: *Nature reviews. Molecular cell biology* 21 (6), S. 341–352. DOI: 10.1038/s41580-020-0237-9.

Yao, Yinan; Li, Hequan; Chen, Junjun; Xu, Weiyi; Yang, Guangdie; Bao, Zhang et al. (2016): TREM-2 serves as a negative immune regulator through Syk pathway in an IL-10 dependent manner in lung cancer. In: *Oncotarget* 7 (20), S. 29620–29634. DOI: 10.18632/oncotarget.8813.

Ye, Xin; Weinberg, Robert A. (2015): Epithelial-Mesenchymal Plasticity: A Central Regulator of Cancer Progression. In: *Trends in cell biology* 25 (11), S. 675–686. DOI: 10.1016/j.tcb.2015.07.012.

Zakaria, Rasheed; Platt-Higgins, Angela; Rathi, Nitika; Radon, Mark; Das, Sumit; Das, Kumar et al. (2018): T-Cell Densities in Brain Metastases Are Associated with Patient Survival Times and Diffusion Tensor MRI Changes. In: *Cancer research* 78 (3), S. 610–616. DOI: 10.1158/0008-5472.CAN-17-1720.

Zheng, Jiaying; Wang, Lingxiao; Zhao, Shunyi; Zhang, Wenjing; Chang, Yuzhou; Dheer, Aastha et al. (2023): TREM2 mediates MHCII-associated CD4+ T cell response against gliomas. In: *bioRxiv : the preprint server for biology*. DOI: 10.1101/2023.04.05.535697.

Zhong, Jian; Xing, Xudong; Gao, Yixin; Pei, Lei; Lu, Chenfei; Sun, Huixin et al. (2024): Distinct roles of TREM2 in central nervous system cancers and peripheral cancers. In: *Cancer cell* 42 (6), 968-984.e9. DOI: 10.1016/j.ccell.2024.05.001.

Zhong, Li; Chen, Xiao-Fen; Wang, Tingting; Wang, Zhe; Liao, Chunyan; Wang, Zongqi et al. (2017): Soluble TREM2 induces inflammatory responses and enhances microglial survival. In: *The Journal of experimental medicine* 214 (3), S. 597–607. DOI: 10.1084/jem.20160844.

Zhou, Teng; Yan, Yuxin; Lin, Mingxi; Zeng, Cheng; Mao, Xinhui; Zhu, Yifei et al. (2025): Astrocyte involvement in brain metastasis: from biological mechanisms to therapeutic strategies. In: *Cancer metastasis reviews* 44 (3), S. 60. DOI: 10.1007/s10555-025-10276-0.

8. Acknowledgements

I would like to begin by expressing my deepest gratitude to everyone who paved the way for me, stood by my side, and made it possible for me to reach this point in my PhD journey. This work would not have been possible without each one of you. This is for you.

To all my lab colleagues, those who were there at the beginning (Laura, Christoph), those who joined along the way (Fabian, Elias, Magdalena, Christina), and those who accompanied me toward the end (Carmen, Niklas, Nico and Sara): Vielen Dank euch allen, dass ihr Teil meiner drei-einhalb Jahre intensiven Doktorarbeit wart. Your support, teamwork, and kindness meant a great deal to me.

To my fellow PhD students, Dhyani, Abir, Marianna, Chiara, Elena and Omer, thank you for making this journey more bearable, more joyful, and infinitely more fun. It would never have been the same without you.

Ich muss Gunnar und Elena sehr herzlich danken für die tägliche Unterstützung im Labor. Ohne euch wäre unser Alltag im Labor ein Chaos. Danke für eure ausgezeichnete und hervorragende technische Unterstützung, die bei vielen Experimenten den entscheidenden Unterschied gemacht hat. Danke, dass ihr immer für uns da wart.

Eine besondere Erwähnung geht an Raquel und Tobi, die immer den Weg für mich weitergeleitet haben und eine entscheidende Rolle bei der Entwicklung dieser Arbeit gespielt haben.

Raquel, danke für deine tägliche Betreuung im Labor und dafür, dass du mir stets den bestmöglichen Weg aufgezeigt hast.

An Tobi: Danke für das Privileg, Teil der Gruppe zu sein. Deine Unterstützung während meiner Arbeit hat mich beruflich und persönlich weitergebracht. Ich bin sehr dankbar für alles, was ich von euch gelernt habe.

To my family in Egypt: all that I am, I owe to you. I can never thank my parents enough for believing in me unconditionally. You are my source of happiness, strength, and everything good in my life. بحبّكم يا أغلى ما عندي . يا سندي وظهري في حياتي كلها

And lastly, to my life partner, you have been always the shoulder I leaned on throughout this entire PhD journey. You pushed me, lifted me, and gave me strength every time I felt I couldn't go on in ways I can never describe. Forever grateful for you. Te amo muito, meu amor. Nada compara a você.

To my little angel, Raphael: you filled our lives with so much love and helped us become the best versions of ourselves. I hope you read this one day and know how much strength you gave your mommy.

To all of you, whose support has carried me, I dedicate this thesis.

9. DECLARATION OF INDEPENDENCE

I, Jessica Alves de Lima (geb. Sonbol), born on 01.05.1995 in Alexandria (Egypt), hereby declare that I have prepared this thesis without the unauthorized assistance of third parties and without the use of resources other than those indicated.

The data and concepts taken directly or indirectly from other sources are marked with an indication of the source. In particular, I have not made use of the paid assistance of intermediary or advisory services (doctoral advisors or other persons).

The thesis has not been submitted to any other examination authority in the same or a similar form, neither in Germany nor abroad.

Landau an der Isar, 27.12.2025